


# Structural dynamics of proteins explored via time-resolved x-ray liquidography

Cite as: Chem. Phys. Rev. **3**, 041304 (2022); <https://doi.org/10.1063/5.0101155>

Submitted: 30 May 2022 • Accepted: 20 October 2022 • Published Online: 15 November 2022

Yunbeom Lee, Hyosub Lee and  Hyotcherl Ihee

## COLLECTIONS

 This paper was selected as Featured



[View Online](#)



[Export Citation](#)



[CrossMark](#)

 **The Journal  
of Chemical Physics**

**Special Topics** Open for Submissions

[Learn More](#)

# Structural dynamics of proteins explored via time-resolved x-ray liquidography

Cite as: Chem. Phys. Rev. **3**, 041304 (2022); doi: [10.1063/5.0101155](https://doi.org/10.1063/5.0101155)

Submitted: 30 May 2022 · Accepted: 20 October 2022 ·

Published Online: 15 November 2022



View Online



Export Citation



CrossMark

Yunbeom Lee,<sup>1,2</sup> Hyosub Lee,<sup>1,2</sup> and Hyotcherl Ihee<sup>1,2,a)</sup> 

## AFFILIATIONS

<sup>1</sup>Center for Advanced Reaction Dynamics, Institute for Basic Science, Daejeon 34141, South Korea

<sup>2</sup>Department of Chemistry and KI for the BioCentury, Korea Advanced Institute of Science and Technology (KAIST), Daejeon 34141, South Korea

<sup>a)</sup> Author to whom correspondence should be addressed: [hyotcherl.ihee@kaist.ac.kr](mailto:hyotcherl.ihee@kaist.ac.kr)

## ABSTRACT

The structure of a protein is closely related to its biological function. In this regard, structural changes, as well as static structures, have been scrutinized as essential elements in understanding and controlling the function of a protein. In particular, the structural change in the solution phase needs to be elucidated to properly understand protein functions under physiological conditions. Time-resolved x-ray liquidography (TRXL), also known as time-resolved x-ray solution scattering, has attracted attention as a powerful experimental method for studying the structural dynamics of proteins in the solution phase. Initially, TRXL was used to study the structural dynamics of small molecules in the solution phase, and later, its application was extended to probe the structural changes in proteins. Via TRXL, structural changes ranging from large quaternary movements to subtle rearrangements of the tertiary structures have been successfully elucidated. In this review, we introduce various studies using TRXL to investigate the structural dynamics of proteins. These include early TRXL studies on model systems, those on photoreceptor proteins, and recent studies using stimuli beyond the direct photoexcitation of proteins.

© 2022 Author(s). All article content, except where otherwise noted, is licensed under a Creative Commons Attribution (CC BY) license (<http://creativecommons.org/licenses/by/4.0/>). <https://doi.org/10.1063/5.0101155>

## TABLE OF CONTENTS

I. INTRODUCTION .....	1	B. Poly-L-glutamic acid (pH jump) .....	31
II. EXPERIMENTAL SCHEME OF TRXL .....	2	C. Cytochrome c (pH jump and electron transfer) ..	31
III. DATA ANALYSIS TO EXTRACT THE KINETICS AND STRUCTURAL DYNAMICS .....	5	D. ATP-binding proteins (photocaged molecule) ...	34
IV. TRXL STUDIES USING PHOTOEXCITATION .....	6	1. Nucleotide-binding domain from MsbA .....	34
A. Heme proteins .....	6	2. Sarco/endoplasmic reticulum Ca <sup>2+</sup> ATPase ...	35
1. Hemoglobin .....	6	3. Adenylate kinase .....	36
2. Myoglobin .....	7	E. Other examples .....	37
3. Homodimeric hemoglobin .....	9	1. Hemoglobin .....	37
4. Cytochrome c .....	13	2. Cyclophilin A .....	38
B. Photoreceptor proteins .....	14	3. Bovine $\alpha$ -lactalbumin (BLA) .....	38
1. Phytochrome .....	14	4. Myoglobin .....	40
2. Retinylidene proteins .....	18	VI. SUMMARY AND OUTLOOK .....	41
3. Photoactive yellow protein .....	21		
4. Light-oxygen-voltage domain .....	24		
5. Other examples .....	27		
V. TRXL STUDIES USING OTHER PUMP METHODS ..	29		
A. Insulin (T-jump) .....	29		
1. Insulin dimer .....	29		
2. Insulin hexamer .....	31		

## I. INTRODUCTION

Proteins are indispensable biological molecules that perform various roles necessary for sustaining living organisms. Naturally, there have been intensive efforts to understand, regulate, and improve the functions of proteins. Through such endeavors, a core concept called the “structure–function relationship” has been established that a protein’s structure is one of the most important factors in regulating a

protein's function. For example, since the substrate binding of a protein is closely related to the protein structure, researchers often explain the substrate-binding properties based on protein structures. This approach is effective in designing drugs that control the function of a protein.<sup>1–3</sup> While determining a static protein structure is often satisfactory in this regard, in reality, a protein is not confined to static conformations. Instead, the proteins in action usually undergo structural changes while performing functions *in vivo*. Protein structural dynamics, how proteins perform their functions through structural changes, have an inseparable relationship with the functions of proteins.

One of the experimental methods developed for studying protein structural dynamics is time-resolved x-ray liquidography (TRXL).<sup>4–10</sup> Initially, this method, also known as time-resolved x-ray solution scattering (TRXSS), was used to study the structural dynamics of small molecules in the liquid solution phase. For example, TRXL allowed for the reaction pathways and the molecular structures of reaction intermediates for the photodissociation of various haloalkanes,<sup>11–24</sup> metal halides,<sup>25–28</sup> and halogen or halide molecules<sup>29–38</sup> to be successfully revealed. Since the first case of its application to protein systems was reported in 2008,<sup>39</sup> TRXL has been actively used for structural dynamics studies on proteins as well as on small molecules. In a TRXL experiment, the reaction of a target sample is initiated using a pump pulse, and an x-ray pulse is delivered to the sample after a specific time delay relative to the pump pulse to obtain an x-ray scattering signal.<sup>4,5</sup> As the x-ray scattering phenomenon is closely related to the structure of a molecule, analyzing the changes in the x-ray scattering signal can reveal how the structure of a protein changes with time.<sup>5</sup> TRXL has several advantages over other techniques, such as time-resolved x-ray crystallography (TRXC),<sup>8,40</sup> which allows for extracting the structural dynamics of proteins. TRXC is a method for investigating the structural dynamics of molecules by employing x-ray crystallography and has the advantage of visualizing the structural changes in molecules in crystals with an atomic spatial resolution.<sup>41–63</sup> However, many biological reactions occur in the liquid solution phase rather than in the crystalline phase. Several studies have reported that the structural changes that occur in the crystalline phase may differ from those in the solution phase.<sup>64–69</sup> As TRXL uses a solution as a sample, it has the advantage of observing the structural changes in the solution phase, which better presents the physiological conditions in which many biological reactions occur. In the case of time-resolved optical spectroscopy, which is widely used to study reaction dynamics,<sup>70–75</sup> its signal is not a direct function of the molecular structure, although the signal can be influenced by the molecular structure. In general, an optical spectroscopic signal is dominantly governed by the electronic state of a molecule rather than the molecular structure. Accordingly, the time-resolved optical spectroscopic signal offers information on the temporal changes in populations in electronic states. Additional theoretical calculations such as time-dependent density functional theory (TDDFT) and DFT calculations are required to infer the molecular structures corresponding to the electronic states. Such theoretical calculations are often computationally demanding or inaccurate, especially for large molecules such as proteins. On the contrary, because the signal of TRXL is a direct function of the structure of a molecule, the structure of the molecule can be more conveniently obtained from the TRXL signal.

Due to these advantages, TRXL has been widely used to study the structural dynamics of proteins in the solution phase (Fig. 1). In this review, we discuss how TRXL has been developed and applied to

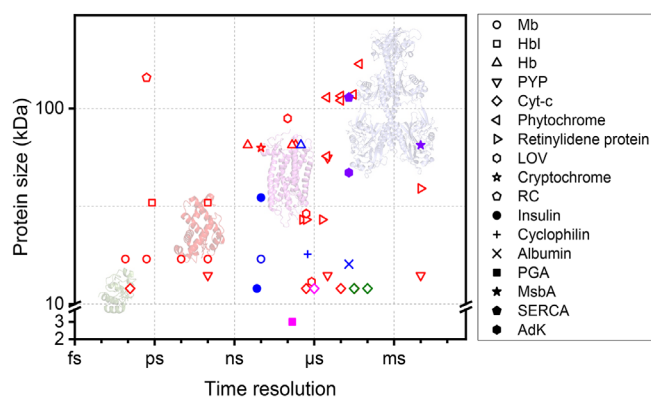


**FIG. 1.** A diagram depicting all of the proteins covered in this review in terms of time resolution and protein size. Each color indicates the methods used for triggering the reaction (red: photoexcitation, blue: T-jump, magenta: pH jump, green: electron transfer, and purple: photocaged molecule). The proteins covered in this review are specified by the shapes of the symbols. The abbreviations used in this figure are as follows: Hbl: homodimeric hemoglobin, PYP: photoactive yellow protein, RC: photosynthetic reaction center, LOV: light-oxygen-voltage domain, PGA: poly-L-glutamic acid, SERCA: sarco/endoplasmic reticulum  $\text{Ca}^{2+}$  ATPase, and AdK: adenylate kinase. Four semitransparent crystal structures represent one of the proteins in each sector in terms of protein size and time resolution (from left to right, green: cyt-c, red: Mb, purple: bacteriorhodopsin (bR), one of the retinylidene proteins, and blue: phytochrome). The earliest positive time delay of the experiment was considered as the time resolution of the experiment unless the time resolution was explicitly specified.

protein systems by introducing various studies that reveal the structural dynamics of proteins in the solution phase using TRXL. First, in Sec. IV, we introduce studies using photoexcitation as the means to initiate a reaction, which was extensively used in the early days of TRXL. Section IV is divided into Subsections IV A and IV B: Sec. IV A is the TRXL studies on model systems such as hemoglobin (Hb) and myoglobin (Mb), and Sec. IV B is those on proteins that are naturally photoactive under physiological conditions, such as phytochromes. In Sec. V, recent TRXL studies with various reaction triggers beyond photoexcitation are discussed. This section is divided into four subsections according to the reaction trigger: Sec. V A temperature jump (T-jump) of insulin, Sec. V B pH jump of poly-L-glutamic acid (PGA), Sec. V C electron transfer and pH jump of cytochrome c (cyt-c), and Sec. V D studies using photocaged molecules on adenosine 5'-triphosphate (ATP)-binding proteins, such as the nucleotide-binding domain (NBD) from a bacterial lipid flippase.

## II. EXPERIMENTAL SCHEME OF TRXL

In TRXL, a pump-probe scheme is combined with x-ray scattering to investigate the structural changes of molecules as a function of time. In a typical pump-probe scheme, the reaction of the target system is initiated using a pump pulse such as an optical laser pulse, and the change that occurs during the reaction is tracked using a probe pulse, which is often another optical laser pulse. The pump-probe scheme has been widely used in the studies of reaction dynamics because it can reveal the real-time reaction progress of the target system by controlling the time interval (the time delay) between the pump and probe pulses. In TRXL, an x-ray pulse is used as the probe, and the x-ray scattering signals of the target system (sample) are measured at various time delays using a 2D area detector [Fig. 2(a)].

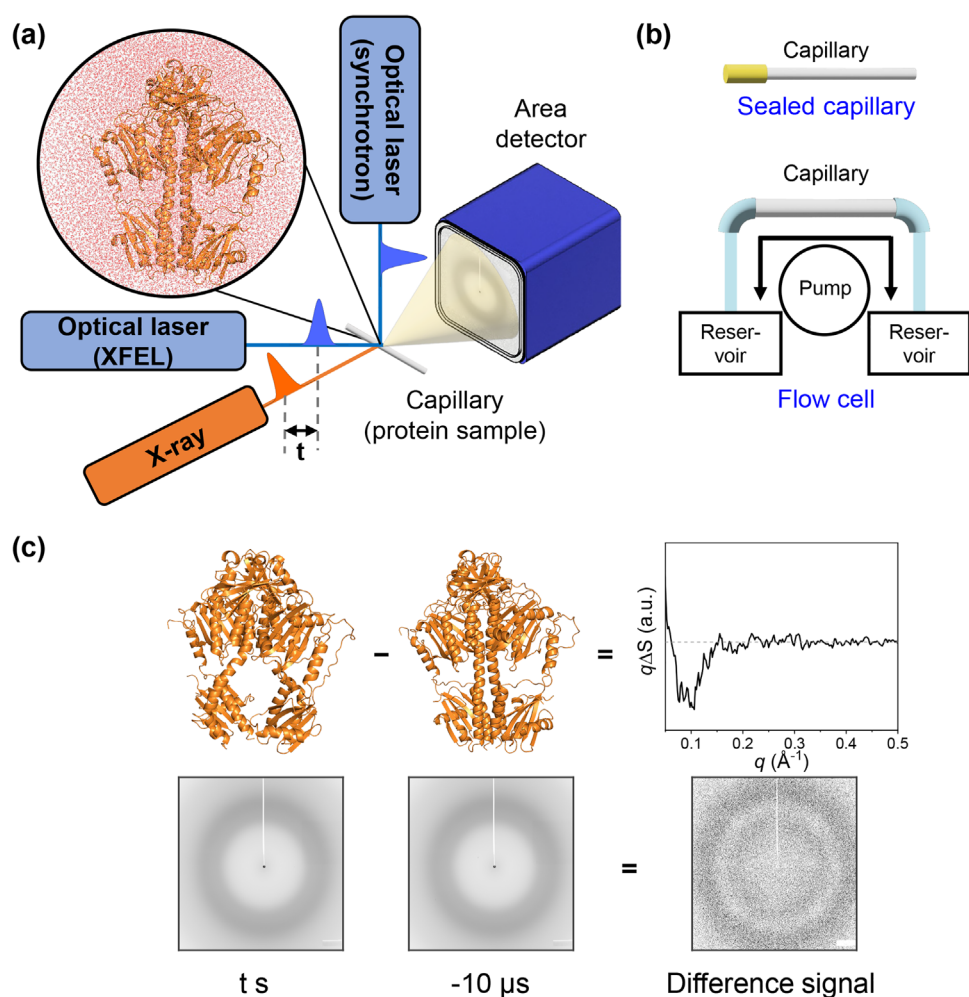


**FIG. 2.** (a) Experimental schematic for TRXL on proteins. A reaction is initiated by a pump pulse, which is typically an optical laser pulse. Afterward, an x-ray pulse, the probe, interrogates the structural change of a protein molecule accompanied by the reaction. The optical laser and x-ray pulses have an orthogonal geometry in a typical protein TRXL experiment at a synchrotron, whereas they have a collinear geometry in a typical protein TRXL experiment at an XFEL. The scattered x-ray signal is collected on an area detector. (b) Schematics for sealed capillary and flow cell systems, which are representative methods for protein sample delivery for TRXL. In the method using a sealed capillary, the protein sample is loaded in a sealed capillary. For the method using a flow cell, the sample is flowed through a capillary back and forth between reservoirs using a mechanical pump. (c) Schematic for the generation of a difference x-ray scattering curve. The x-ray scattering signal collected at a reference time delay (for example,  $-10 \mu\text{s}$ ) is subtracted from the x-ray scattering signal collected at a positive time delay to generate a difference x-ray scattering signal. The difference x-ray scattering signal contains information about the structural change during the reaction.

Typically, the x-ray and laser have an orthogonal geometry when a protein TRXL experiment is performed at a synchrotron, whereas they have a collinear geometry for a protein TRXL experiment at an x-ray free-electron laser (XFEL). For the delivery of protein samples for a TRXL experiment, a protein sample sealed in a thin capillary is typically used [Fig. 2(b)]. This method, which allows an experiment to be performed with a small amount of sample, is often used for a protein with a reversible photocycle. Still, it has the disadvantage of being vulnerable to the accumulation of damage due to x-rays and optical photons. In addition, such an approach is difficult to be used when a target reaction has a long recovery time or is irreversible. Such problems can be remedied by repeatedly moving a capillary during the measurement to change the position exposed to the pump and probe

pulses. An alternative method to solve this problem is to use a flow cell [Fig. 2(b)]. In the method using a flow cell, the protein sample circulates back and forth through a capillary via a mechanical pump. In a method using a flow cell, a larger amount of a protein sample can be used compared to the sealed capillary, which can reduce the damaged fraction in the whole sample. The back-and-forth flow of the sample can facilitate the dissipation of the damaged portion throughout the whole sample, which reduces the accumulation of the damaged sample in a specific position of a capillary. In addition, as a back-and-forth flow cycle gives ample time to allow the photoexcited molecules to be recovered to the ground state, a flow cell can be applied to a system with a long recovery time. A protein sample in a flow cell can often be flowed



one way rather than in a back-and-forth manner, and the sample exposed to a pair of pump and probe pulses is then discarded. In this way, a method using a flow cell is applicable to a system with an irreversible reaction. After measuring x-ray scattering images, difference x-ray scattering signals are obtained by subtracting the reference x-ray scattering signal from the x-ray scattering signals collected at various time delays [Fig. 2(c)]. The x-ray scattering signal measured before the reaction trigger or the x-ray scattering signal measured without the reaction trigger is used as the reference x-ray scattering signal. Since the x-ray scattering signal contains direct information on the structure of the molecule, the difference x-ray scattering signals contain information on how the structure of a molecule has changed compared to that before the initiation of the reaction. In general, as molecules in the solution phase have random orientations, the 2D scattering signal of the solution sample obtained using a 2D area detector has isotropic features. Based on these characteristics, the 2D scattering signal is averaged along the azimuthal angle to yield a 1D scattering curve, which is then used for analysis.<sup>4,5,7</sup> On the other hand, under certain circumstances, the angular distribution of molecules can be anisotropic. For example, when molecules are excited by a linearly polarized laser pulse, the excitation probability increases as the angle between the laser polarization and the transition dipole decreases. Accordingly, the orientational distribution of the excited molecules becomes transiently anisotropic. In this case, the 2D scattering signal and the 2D difference scattering signal exhibit anisotropic characteristics, and the angular anisotropy can be analyzed using the anisotropy of the difference x-ray scattering signal.<sup>38,76–79</sup>

In most TRXL studies, optical laser pulses were used to initiate the reaction. In this method, the chromophore of a protein is photoexcited by an optical laser pulse, and the subsequent structural change of the protein is investigated [Fig. 3(a)]. One of the advantages of using optical pulses as the pump is that a high time resolution can be

achieved thanks to the availability of temporally short optical laser pulses. At synchrotrons,<sup>80–82</sup> the x-ray pulse width is  $\sim 100$  ps or tens of picoseconds, which is longer than that of a femtosecond laser pulse and, accordingly, limits the time resolution. As a shorter x-ray pulse width became available thanks to the advent of XFELs,<sup>83–87</sup> a time resolution better than a subpicosecond is now accessible. Such excellent temporal resolutions were exploited to reveal changes in the structures of molecules that could not be previously observed with synchrotron-based TRXL due to their occurrence on faster time scales.<sup>88</sup> Because of this advantage in terms of time resolution, early TRXL studies mainly used reaction initiation using optical laser pulses.

Despite successful studies, the reaction initiation scheme using an optical laser pulse limits the range of applicable proteins. The biological functions of many proteins in physiological conditions are triggered by stimuli other than light. For example, protein unfolding is often triggered by external stimuli such as temperature changes or the addition of denaturants. In addition, enzymatic activity, a typical biological function of a protein, can be activated by binding to a substrate. Recently, various methods of initiating a reaction beyond photoexcitation have been combined with TRXL, opening the possibility of exploring the structural dynamics of nonphotoactive proteins with TRXL. Representative examples include (i) a T-jump method [Fig. 3(b)] to study structural dynamics triggered by temperature changes, (ii) the release of protons or caged molecules upon photoexcitation [Fig. 3(c)] to investigate the reactions initiated via protonation or substrate binding, and (iii) electron transfer from a photosensitizer [Fig. 3(d)] to explore the reaction triggered by the change of an oxidation state. In these methods, the optical laser pulse does not directly excite the protein but other molecules to induce changes in chemical and physical environments such as temperature, pH, and the electronic state of a metal ion in a protein or to release substrate molecules that can bind the protein molecule.

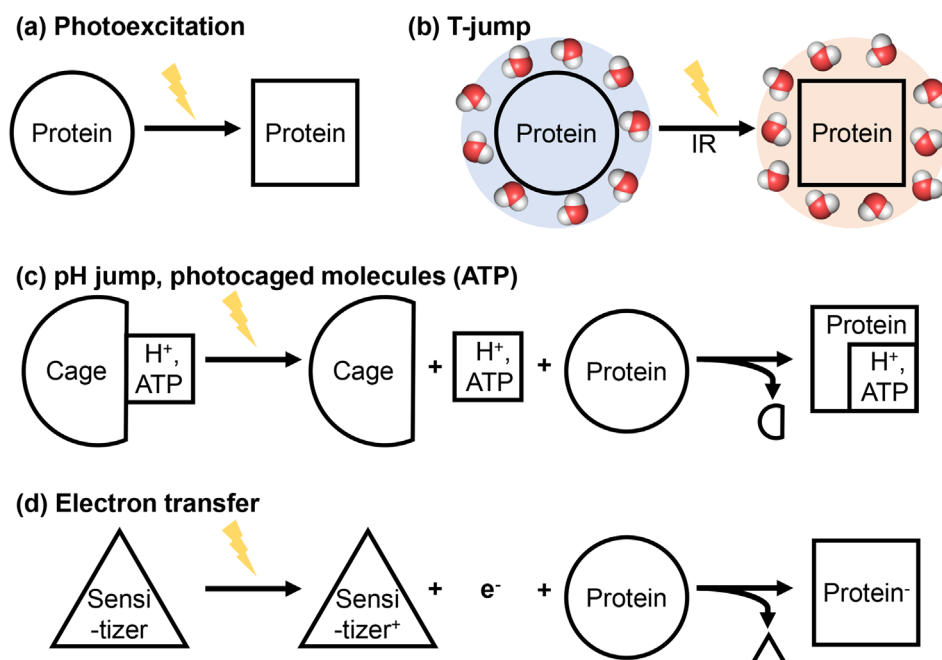


**FIG. 3.** Schematic of various schemes to initiate a reaction. Reactions of a protein sample can be initiated by various triggers. (a) Direct photoexcitation: If a protein can absorb light, a photoreaction can be initiated by sending photons, which are commonly delivered in the form of an optical pulse from a pulsed laser system, to the protein. (b) Temperature jump (T-jump): an increase in the temperature, which is typically achieved by photoexcitation of the vibrational modes of the solvent molecules by a laser pulse with a wavelength in the infrared (IR) region. (c) pH jump or release of photocaged molecules: binding with protons or molecules, which are dissociated from their cages upon photoexcitation. (d) Electron transfer from a photoexcited photosensitizer: a change in the oxidation state of a protein via the electron transfer from the photosensitizer.

### III. DATA ANALYSIS TO EXTRACT THE KINETICS AND STRUCTURAL DYNAMICS

The x-ray scattering intensity from a protein molecule in the solution phase can be described as a function of the magnitude of the momentum transfer vector ( $q$ ) as follows:

$$S(q) = |A_p(q) - \rho_0 A_e(q) + \Delta \rho A_{bl}(q)|^2, \quad (1)$$

where  $S(q)$  is the x-ray scattering intensity,  $A_p(q)$  is the scattering amplitude of a protein in a vacuum,  $\rho_0$  is the electron density of the excluded volume,  $A_e(q)$  is the scattering amplitude of the excluded volume with unitary density,  $\Delta \rho$  is the electron density contrast of the border layer around the protein (for example, the hydration shell) to  $\rho_0$ , and  $A_{bl}(q)$  is a scattering amplitude of the border layer with unitary density.  $A_p(q)$ , as well as other terms such as  $A_e(q)$ , contributing to the x-ray scattering intensity, is largely affected by the structure of a protein. For example,  $A_p(q)$  can be described as a function of the positions ( $r_j$ ) and form factors [ $f_j(q)$ ] of the atoms constituting a protein:

$$A_p(q) = \sum_j f_j(q) \exp(-iq \cdot r_j). \quad (2)$$

As seen in this equation, the x-ray scattering intensity is closely related to the protein structure, and the structural information can be obtained from the x-ray scattering intensity. Distributed programs, such as CRY SOL and FoXS, or inhouse programs are used for the calculation of the x-ray scattering intensity.<sup>89,90</sup>  $\Delta S(q, t)$ , which is the difference between the x-ray scattering intensity at a time delay ( $t$ ) and that at a reference time delay ( $t_{\text{ref}}$ ), can be expressed as follows:

$$\Delta S(q, t) = S(q, t) - S(q, t_{\text{ref}}). \quad (3)$$

The TRXL data obtained from experiments are analyzed via kinetic analysis and structure refinement. One of the representative methods used for the kinetic analysis of the TRXL data is the method aided by singular value decomposition (SVD) and kinetic modeling.<sup>66,67,91</sup> In this method, SVD is used to decompose the TRXL data into left singular vectors (LSVs), right singular vectors (rSVs), and singular values. LSVs, rSVs, and singular values correspond to time-independent scattering signals, the time profiles of LSVs, and the contributions of each singular vector to the data, respectively. Two types of information can be obtained through an SVD analysis: One is the minimum number of distinguishable reaction intermediates, which is determined from the number of singular vectors that predominantly contribute to the data. The other is the time constants for the transition between the reaction intermediates, which are obtained via the kinetic fitting of the rSVs. Based on the information on the number of reaction intermediates and time constants for the transition, candidate kinetic models compatible with this information can be generated. Then, for each kinetic model, the reconstructed TRXL data are obtained using the concentrations and species-associated difference scattering curves (SADSs) of the reaction intermediates. The SADSs are optimized to minimize the disagreement between the reconstructed TRXL data and the experimental TRXL data. Typically, the discrepancy can be expressed as follows:

$$\chi^2 = \sum_{i,j} \left( \frac{\Delta S_{\text{exp}}(q_i, t_j) - \Delta S_{\text{recon}}(q_i, t_j)}{\sigma(q_i, t_j)} \right)^2, \quad (4)$$

where  $\Delta S_{\text{exp}}(q_i, t_j)$  and  $\Delta S_{\text{recon}}(q_i, t_j)$ , respectively, are the x-ray scattering intensities of the experimental data and the reconstructed data at  $q_i$  and  $t_j$ , and  $\sigma(q_i, t_j)$  is the standard error of the mean at  $q_i$  and  $t_j$ . Among the plausible kinetic models, the kinetic model whose reconstructed data show the best agreement with the experimental data is selected as the optimal kinetic model, and the concentration profiles and SADSs of the intermediates obtained based on the optimal kinetic model are used for further analysis. When the number of intermediates and time constants participating in the reaction is large, the number of candidate kinetic models compatible with the SVD results increases as well. Accordingly, it becomes difficult to determine an optimal kinetic model. We developed variable time range SVD (VT-SVD) and SVD-aided pseudo principal component analysis (SAPPA) to solve this problem.<sup>92</sup> In VT-SVD, SVD is performed on the experimental data of several, limited time ranges rather than the entire time range. Because kinetic models not consistent with the VT-SVD results can be ruled out for further analysis, the number of possible kinetic models can be substantially reduced. In SAPPA, the experimental data in the time segments where rSVs are stationary are searched so that they can be used as bases to decompose the experimental data. Then, the experimental data at each time delay are fitted using a linear combination of the bases to generate the time profiles of the bases. If the number of time domains where rSVs are stationary is the same as the number of reaction intermediates, the bases and time profiles obtained from SAPPA can be regarded as the SADSs and time profiles of the reaction intermediates, respectively. In this way, SAPPA allows a kinetic analysis to be performed without determining the optimal kinetic model. Since the SADSs obtained from the kinetic analysis have information on the structures of the reaction intermediates, structure refinement is performed on the SADSs to elucidate the structures of the reaction intermediates.

The structural information in the real space can be obtained by the Fourier transform of the x-ray scattering or diffraction signal observed in the  $q$  space (reciprocal space), as the real space and the  $q$  space have a reciprocal relationship. For example, molecules in a crystal have a periodic arrangement, and the x-ray diffraction signal from a single crystal has spot-like features. In a crystallographic analysis, diffraction spots are indexed with a set of Miller indices ( $h$ ,  $k$ , and  $l$ ) in the reciprocal space, and a 3D molecular structure in the real space can be directly obtained through the Fourier transform of the amplitudes of the structure factors of the diffraction spots if phase information is given. In contrast, molecules in solution typically have random arrangements leading to a diffuse isotropic x-ray scattering signal. For such x-ray scattering signals, only 1D structural information, the distances between the atoms constituting the system, can be obtained. In this regard, it is challenging to obtain a 3D molecular structure directly from the x-ray scattering data due to the insufficient number of experimental observables. To obtain a 3D molecular structure from 1D structural information, structural modeling is required. For TRXL, two modeling methods, one using dummy atoms and the other based on a reported high-resolution protein structure, are widely used for such a purpose. Typically, the former and the latter are used to analyze small-angle x-ray scattering (SAXS) and wide-angle x-ray scattering (WAXS) data, respectively.<sup>6</sup>

From the analysis of the SAXS region, the overall protein size or low-resolution structure can be obtained, as the data of the SAXS region contain information on the global structure of the protein.

A low-resolution structure is generally obtained as follows: First, the species-associated static scattering curve (SAC) representing the x-ray scattering curve of a reaction intermediate is constructed by adding the x-ray scattering curve of the ground state to the SADS considering the quantum yield of the reaction. Then, the pair distribution function of a reaction intermediate is calculated by the sine Fourier transform of the SAXS region of the SAC. Such a process is typically performed using GNOM software.<sup>93</sup> Finally, the *ab initio* structure is reconstructed using the pair distribution function and SAC. In *ab initio* structure reconstruction, the structure of a protein is regarded as being made of bead-shaped dummy atoms, and structure reconstruction is performed by optimizing the structure to describe the pair distribution function and SAC. *Ab initio* structure reconstruction can be performed via DAMMIN software.<sup>94</sup> Although this approach provides a low-resolution structure, it has the advantage of reconstructing the protein structure without detailed prior knowledge of the protein structure.

The analysis of the WAXS region can offer information on relatively detailed structural change, including the movements of the tertiary structures, such as the  $\alpha$  helices and  $\beta$  sheets. To obtain such information, a high-resolution template structure, such as a crystal structure, is used as a starting template structure for the analysis. Trial structures are generated from the template structure through various methods. For example, trial structures can be generated from snapshots of molecular dynamics (MD) simulation results on the template structure. In addition to generating various snapshots, MD simulations aid in retrieving plausible 3D structures from the limited structural information encrypted in x-ray scattering data by constraining the search space to physically allowed structures. Among the trial structures, those of which the theoretical difference scattering curves have good agreement with the SADS are selected as the structures of a reaction intermediate. Typically, the disagreement between the theoretical difference scattering curve and SADS can be expressed as follows:

$$\chi^2 = \sum_i \left( \frac{\Delta S_{\text{SADS}}(q_i) - c \Delta S_{\text{theo}}(q_i)}{\sigma(q_i)} \right)^2, \quad (5)$$

where  $\Delta S_{\text{exp}}(q_i)$  and  $\Delta S_{\text{theo}}(q_i)$  are the x-ray scattering intensities of the SADS and theoretical difference scattering curve at  $q_i$ , respectively,  $\sigma(q_i)$  is the standard error of the mean at  $q_i$ , and  $c$  is the scaling factor between the SADS and theoretical difference scattering curve. The scaling factor,  $c$ , is closely related to the concentration of the reaction intermediate (or photoreaction yield) of the sample. One way to estimate the scaling factor is to use the information obtained from spectroscopic measurements. Although this analysis method for TRXL requires a 3D molecular structure of the protein as prior knowledge, it has a great advantage in that it can refine even detailed structural changes, such as the movement of the  $\alpha$  helices. In some studies, to facilitate the structure refinement process, modified MD simulations with additional information rather than conventional MD simulations were used to generate the trial structures. For example, a potential energy term corresponding to the discrepancy of the theoretical difference scattering curve and a SADS is added to the conventional MD simulation.<sup>95</sup> Through this, MD simulations can be performed more efficiently by guiding the simulations to obtain snapshots that exhibit better agreement with the SADS. As the number of reported crystal structures and the accuracy of MD simulations increase, this structure refinement method has further room for improvement.

## IV. TRXL STUDIES USING PHOTOEXCITATION

### A. Heme proteins

#### 1. Hemoglobin

Hemoglobin (Hb) is a heme protein with a heme group as the cofactor. The heme group of Hb can bind small gaseous molecules such as dioxygen and carbon monoxide, and Hb is involved in the transportation of gaseous molecules. Hb forms a tetrameric structure composed of four subunits, and the ligand-binding affinity of each subunit is regulated by the ligand-binding state of the other subunits, which is called allosteric regulation.<sup>96–98</sup> For example, Hb exhibits cooperative ligand binding, in which the ligand-binding affinity of a subunit increases as other subunits become ligated. Hb has a ligand-bound R state with high ligand-binding affinity and a ligand-unbound T state with low ligand-binding affinity, and the two states have different structures [Fig. 4(a)]. Since gaseous molecules bound to the heme group of Hb undergo dissociation from the heme group upon photoexcitation, the transition from the R state to the T state (R–T transition) of Hb can be easily induced via photoexcitation.<sup>99</sup> Because of these properties, Hb has been investigated extensively as a model system to study the dynamics of the allosteric regulation of proteins.<sup>100–108</sup> Indeed, Hb is one of the first proteins to which TRXL was applied, and the structural dynamics of Hb in solution during the R–T transition were studied with TRXL.<sup>39,109–111</sup>

In the first TRXL study on Hb, an optical pulse with a temporal width of  $\sim 150$  ns was used, and the TRXL data were collected for a time range from 200 ns to  $\sim 10$  ms. A kinetic model with two intermediate states can explain the data [Fig. 4(b)].<sup>39</sup> The first intermediate state is assigned to the R-like state with some tertiary structural changes but without noticeable quaternary structural changes. The R-like state transforms into the second intermediate (T-like state), which was assigned to a fully deoxygenated state, accompanying both tertiary and quaternary structural changes. Such a transformation corresponds to the R–T transition, and its timescale is  $\sim 1$ – $3$   $\mu$ s. A similar time constant (2  $\mu$ s) for the R–T transition was also reported in a later TRXL study on Hb, in which the data were measured with a narrower time interval.<sup>109</sup> The results of the TRXL studies clarified the timescale for the quaternary structural change upon the R–T transition. In fact, there was a discrepancy in the time constants for the R–T transition obtained from the spectroscopic studies. For example, in some studies,<sup>100,101,104</sup> it was suggested that the quaternary structural change upon the R–T transition occurs with a time constant of  $\sim 20$   $\mu$ s, but in later studies using time-resolved Raman spectroscopy and time-resolved magnetic circular dichroism (CD),<sup>105,107,108</sup> it was argued that the quaternary structural change upon the R–T transition begins to occur with a faster time constant of microseconds or less. Via TRXL, it was confirmed that the quaternary structural change upon the R–T transition occurs with a time constant of  $\sim 2$   $\mu$ s by identifying the global structural change, which is not easy to clarify with the spectroscopic methods. In addition to the kinetics, the conformation of Hb in solution was revealed through a structural analysis of the TRXL data. In particular, the conformation of the R state of Hb in the solution phase was determined from the analysis. While only one crystal structure was reported for the T state, multiple crystal structures, including R and R2, were reported for the R state depending on the crystallization conditions.<sup>112,113</sup> The structure of the R state in the solution phase was unveiled by using the theoretical difference scattering curves that



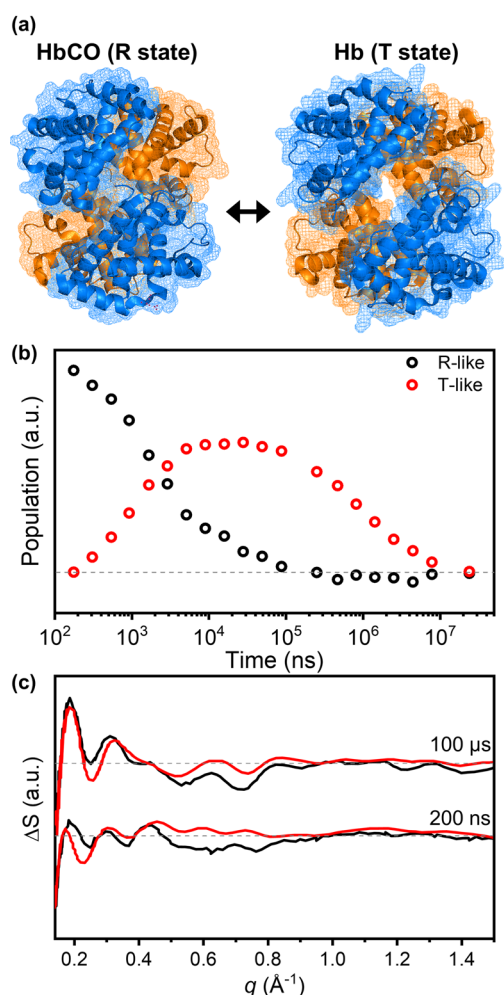


**FIG. 4.** (a) Representative structure of Hb in its carboxy and deoxy states. Two  $\alpha$  subunits are shown in orange, and two  $\beta$  subunits are shown in blue. (b) Time profiles for the populations of the R-like and T-like states obtained from the kinetic analysis of the TRXL data from Hb. (c) Experimental difference scattering curves (black) at 200 ns and 100  $\mu$ s superimposed by the theoretical difference scattering curves (red) calculated for the structural changes of Hb. For the difference scattering curve at 100  $\mu$ s, the theoretical difference scattering curve was calculated by subtracting the x-ray scattering intensity calculated with the crystal structure of R2 from that with the crystal structure of the T state. For explaining the difference scattering curve at 200 ns, the crystal structure of R2 was used for the carboxy R state, and the R2 structure was modified assuming the clamshell motion for the R-like state generated upon photoinduced CO dissociation. The theoretical difference scattering curve was generated by subtracting the x-ray scattering intensity of R2 from that of the modified structure.

were calculated using these crystal structures. The theoretical difference scattering curves were generated by using either R or R2 as the carboxy structure before photoexcitation and the crystal structure of the T state as the structure of the T-like state identified by TRXL. Between two theoretical difference scattering curves, the curve calculated using R2 for the carboxy R state in the solution phase shows better agreement with the experimental difference scattering curve at 100  $\mu$ s [Fig. 4(c)], which can represent the difference scattering curve

of the T-like state generated by photoexcitation. Based on this result, it was suggested that the carboxy state of Hb in the solution phase has a structure similar to that of R2. The structure analysis of the R-like state generated by photoinduced CO dissociation was performed using the difference scattering curve at 200 ns. Considering the clamshell motion of the E and F helices upon the R–T transition proposed in previous studies,<sup>114,115</sup> the crystal structure of R2 was modified to mimic the clamshell motion in the R-like state. Then, a theoretical difference scattering curve was generated by subtracting the x-ray scattering intensity of R2 from that of the modified structure. The theoretical difference scattering curve qualitatively agreed with the target experimental difference scattering curve at 200 ns [Fig. 4(c)]. This result implies that the clamshell motion occurs during the transition to the R-like state.

Later, a TRXL study for a wider time domain was performed on wild-type (WT) Hb and mutant Hb (HbYQ) using a shorter optical laser pulse with a temporal width of 3 ns.<sup>110</sup> In HbYQ, two residues near the distal heme pocket of each subunit were mutated [H(E7)Q and L(B10)Y]. As with WT, this mutant has cooperative ligand binding, but geminate recombination is suppressed.<sup>116,117</sup> The TRXL data from HbYQ are similar to those of WT Hb, although the amplitude of the difference scattering curve at 100  $\mu$ s at which the T-like form is generated is larger for HbYQ. It was interpreted that a larger fraction can undergo the R–T transition for HbYQ because the geminate recombination has hardly occurred in HbYQ. The kinetics showed a difference between WT Hb and HbYQ. For kinetic analysis of WT Hb and HbYQ, the Monod–Wyman–Changeux (MWC) model, frequently used for kinetic analyses of allosteric regulation, was used.<sup>97</sup> The kinetics of both WT Hb and HbYQ were well-described through the MWC model, suggesting the generality of the MWC model. The kinetic analysis was performed on the TRXL data at time delays longer than 250 ns, to which a simplified model could be applied, as the geminate recombination and changes in the tertiary structure are completed in this time domain. This MWC kinetic model was used to calculate the time profiles of the populations of R-like and T-like states. Then, several parameters of the MWC kinetic model, such as the time constant for the R–T transition, were optimized by fitting the experimental data with the theoretical data based on the MWC kinetic model. As a result, the optimized time profiles of the populations and SADs were obtained [Figs. 5(a) and 5(b)]. The rate for the R–T transition of HbYQ is  $\sim 10$  times slower than that of WT Hb. It was suggested that even the mutations of the residues nearby the heme pocket may interfere with the movements of the residues in the subunit interface, whose movements are the largest during the quaternary structural change upon the R–T transition, via the change in the interaction between the residues. Such limited movements of the residues in the interface could slow down the R–T transition.

## 2. Myoglobin

Myoglobin (Mb), as with Hb, is involved in the transport and storage of gaseous molecules using a heme group, and its ligand dissociation can be easily induced through photoexcitation. In contrast to Hb, Mb has a much simpler, monomeric structure. Because of these properties, Mb has been widely studied as a model system for studying the structural dynamics of proteins.<sup>41–48,118–123</sup> The structural dynamics of Mb have also been studied using TRXL, including studies on Mb from sperm whale (swMb)<sup>39,64,91,124</sup> and Mb from horse heart (hhMb).<sup>76,125–128</sup>

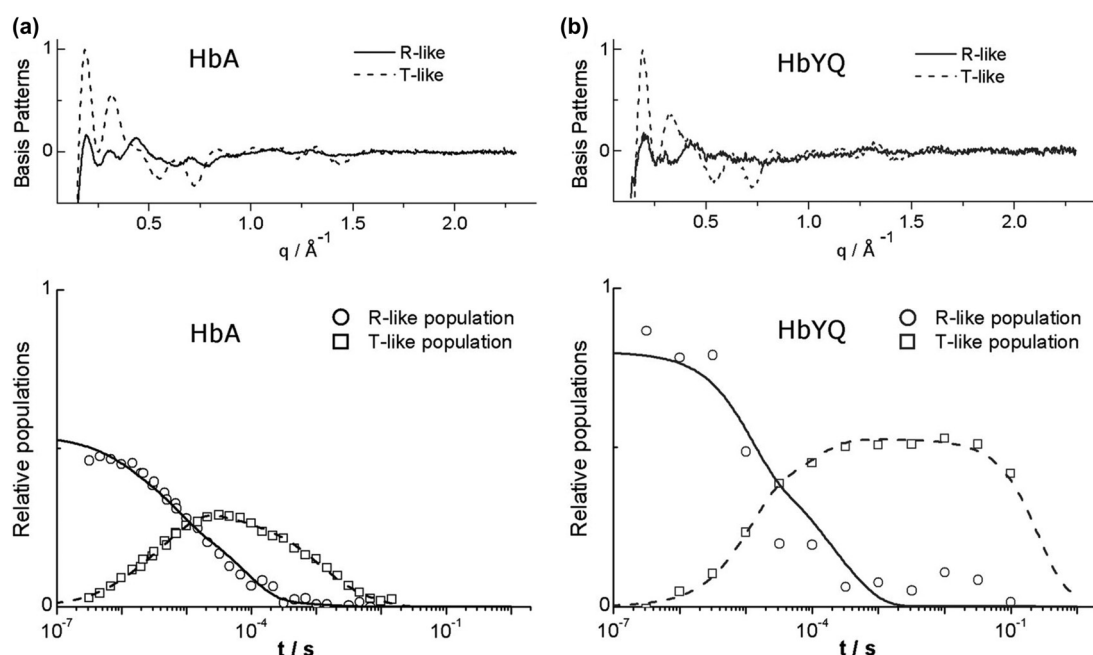


**FIG. 5.** (Top) SADSs and (bottom) time profiles of the populations of intermediates obtained from the kinetic analysis of the TRXL data from (a) WT Hb (HbA) and (b) HbYQ. The SADSs and the populations obtained from the kinetic model for the R-like and T-like states are shown in solid and dashed lines, respectively. The optimal populations for the R-like and T-like states, obtained by fitting the experimental data using the linear combination of the SADSs, are shown with circles and squares, respectively. Reproduced with permission from Levantino *et al.*, Proc. Natl. Acad. Sci. U. S. A. **109**, 14894 (2012). Copyright 2012 National Academy of Science.

In an early TRXL study on swMb,<sup>124</sup> the structural dynamics of Mb were studied using data ranging from 100 ps to 10 ms. Although Mb shows only a small change in its tertiary structure, the difference scattering curves obtained in the TRXL experiment show noticeable features. Based on the analysis of the SAXS region of the TRXL data, it was suggested that the expansion of Mb occurs after photoexcitation, followed by contraction. In addition, the relaxation of the tertiary structure was identified through the change in the signal in the WAXS region, although the detailed information on the change in the 3D protein structure was not clarified. The kinetic analysis was performed using a kinetic model with two-step relaxation of the tertiary structure of Mb, followed by the escaping of the CO ligand from the protein or recombination with the CO ligand. On the contrary, in another TRXL study, a different kinetic model was suggested through a kinetic analysis using SVD.<sup>91</sup>

This TRXL study on swMb revealed the existence of two substates of proteins and their effects on structural dynamics. A protein in a specific conformational state can have multiple conformational substates, which can affect the biological function of the protein. Such conformational substates of Mb were investigated using TRXL. For example, it had been reported that the carboxy state (A state), as well as the state formed rapidly upon the ligand dissociation (B state), has multiple conformational substates depending on the conformation of the distal histidine residue and the orientation of the CO ligand.<sup>129,130</sup> Via TRXL, it was possible to confirm how conformational substates affect the global structural change of the protein. The kinetic analysis aided by SVD on the TRXL data in the time domain from 100 ps to 10 ms showed that the four reaction intermediates (B, C, D, and S states)

are involved in the reaction before Mb returns to the carboxy state [Fig. 6(a)]. The B-to-C state transition has a biphasic feature with time constants of 460 ps and 3.6 ns, which had not been reported in spectroscopic studies. Such a biphasic transition was explained by the conformational substates of the B state. In particular, the interaction between the CO molecule and the adjacent His residue is different for each conformational substate of the B state, inducing different kinetics for the transition to the C state.

A biphasic B-to-C state transition in hhMb, which is similar to that of swMb, was revealed via TRXL as well. In an early TRXL study performed at a synchrotron, it was observed that the B-to-C state transition occurs with a time constant of hundreds of picoseconds.<sup>125</sup> In a subsequent TRXL study on hhMb, using time slicing to improve the time resolution, an additional sub-100 ps time constant was identified for the B-to-C state transition.<sup>126</sup> Via the time slicing technique, the time resolution of the TRXL data collected at a synchrotron (typically ~100 ps) was improved by the deconvolution of the TRXL data using the known temporal width of an x-ray pulse. As a result of a kinetic analysis of the TRXL data from hhMb ranging to 160 ps, two reaction intermediates, which were assigned to the B and C states, were identified. In addition, it was confirmed that the B-to-C state transition occurs with a time constant of 70 ps [Fig. 6(b)], which was not observed in the previous TRXL study. These results, combined with those obtained from the earlier TRXL study, indicate that the transition from the B state to the C state of hhMb also occurs biphasically.

The structural dynamics of Mb were elucidated in terms of not only kinetics but also detailed structures. For swMb, the structure of a reaction intermediate was visualized using structure refinement on the



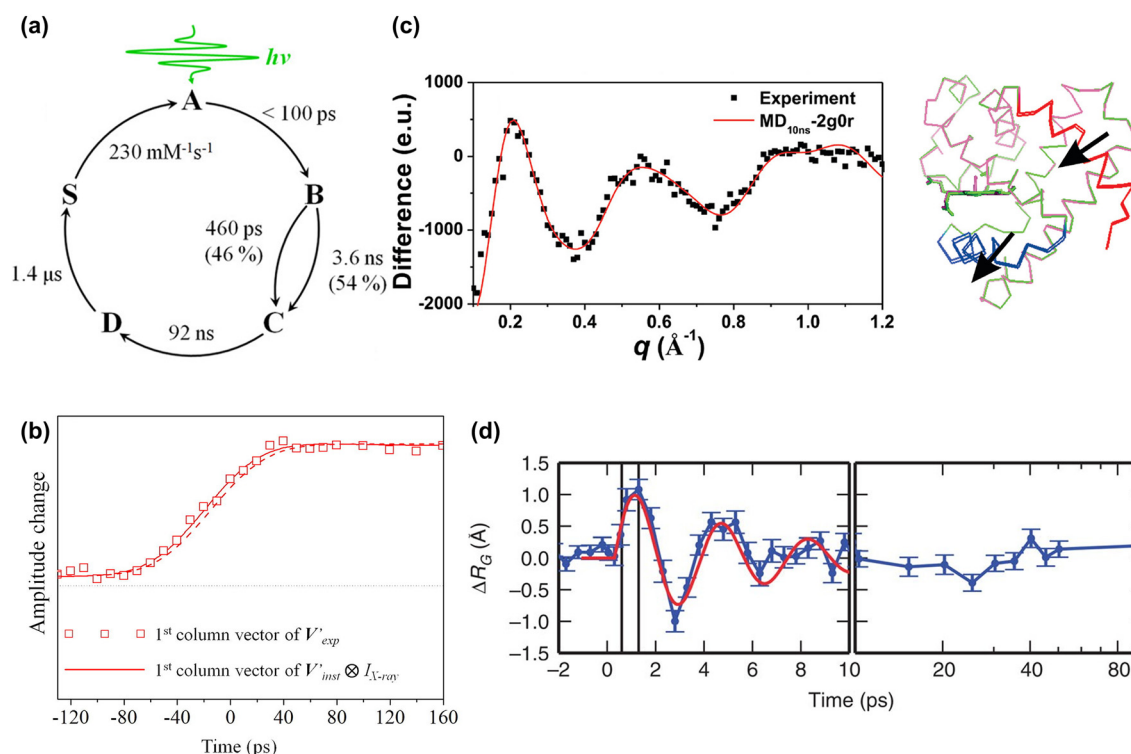


**FIG. 6.** (a) Schematic for the kinetics upon the photoreaction of swMb obtained from a TRXL experiment. Reproduced with permission from Oang *et al.*, J. Phys. Chem. Lett. **5**, 804 (2014). Copyright 2014 American Chemical Society. (b) The first rSV obtained from the TRXL data from hhMb (open square) and the first rSV obtained assuming an instantaneous response convoluted by the temporal profile of the x-ray intensity (red solid line). The instantaneous response was modeled using an exponential function with a time constant of 70 ps. The dashed line indicates the integration of the temporal profile of the x-ray intensity over time. Reproduced with permission from Oang *et al.*, Chem. Phys. **442**, 137 (2014). Copyright 2014 Elsevier B. V. (c) (Left) Experimental difference scattering curve at 10 ns obtained from a TRXL experiment on swMb (black) and theoretical difference scattering curve obtained from the structure refinement (red). (Right) Structures of Mb before (magenta) and after (green) photoexcitation. The A and F helices, which exhibit large movements, are labeled red and blue, respectively. Reproduced with permission from Ahn *et al.*, J. Phys. Chem. B **113**, 13131 (2009). Copyright 2009 American Chemical Society. (d) Oscillation of the  $R_g$  of hhMb in the ultrafast time domain obtained from a fs-TRXL experiment. Adapted from Levantino *et al.*, Nat. Commun. **6**, 6772 (2015). Copyright 2015 Authors, licensed under a Creative Commons Attribution (CC BY) License.

difference scattering curve at 10 ns [Fig. 6(c)].<sup>64</sup> Structure refinement was performed by moving the rigid bodies, which were the helices and heme group of the known crystal structure. The resulting structural change upon photoexcitation is similar to the structural change from the carboxy state to the deoxy state observed in the crystallography study [Fig. 6(c)]. Through this structural analysis, it was confirmed that the clamshell motion of the E and F helices reported in the crystallography study also occurs during the photoreaction of Mb in the solution phase. On the other hand, the movement of the A helix shows a larger structural change than that in the crystal. It was suggested that the movement of the A helix is possibly limited by the crystal contacts within the crystal lattice. The structural change revealed through TRXL agrees with the results of a time-resolved Raman spectroscopy study that suggested the movement of the A and E helices upon photoexcitation.<sup>131</sup>

After the development of XFELs, the ultrafast structural dynamics of Mb, which are inaccessible via synchrotron-based studies, were explored using femtosecond TRXL (fs-TRXL) at an XFEL.<sup>127</sup> In this study, the ultrafast global structural change of Mb was revealed by applying the Guinier analysis to the SAXS region of the TRXL data with a time resolution better than 1 ps. The ultrafast change of the

radius of gyration ( $R_g$ ) was observed within 1 ps after photoexcitation [Fig. 6(d)]. A similar ultrafast change of the  $R_g$  of Mb was reported by another fs-TRXL study where SAXS data were used for the structural analysis.<sup>128</sup> In addition, the  $R_g$  and volume exhibited an underdamped oscillatory feature. It was suggested that such underdamped oscillation is attributed to the synchronized motion of Mb by photoexcitation, not the ensemble-averaged behavior of the typical thermal process of molecules. However, a theoretical study argued that the underdamped oscillation of the  $R_g$  and volume of Mb originated from the change in the hydration shell rather than the motion of the protein because the SAXS region used for the analysis was affected not only by the protein motion but also by the changes in the hydration shell.<sup>132</sup> Indeed, another TRXL study showed that when the WAXS region of the TRXL data is analyzed, the underdamped oscillatory motion is not observed.<sup>133</sup>

### 3. Homodimeric hemoglobin

Homodimeric hemoglobin (HbI) is a heme protein with a homodimeric structure [Fig. 7(a)].<sup>134</sup> As with many other heme proteins, the heme group can bind small molecules such as carbon monoxide

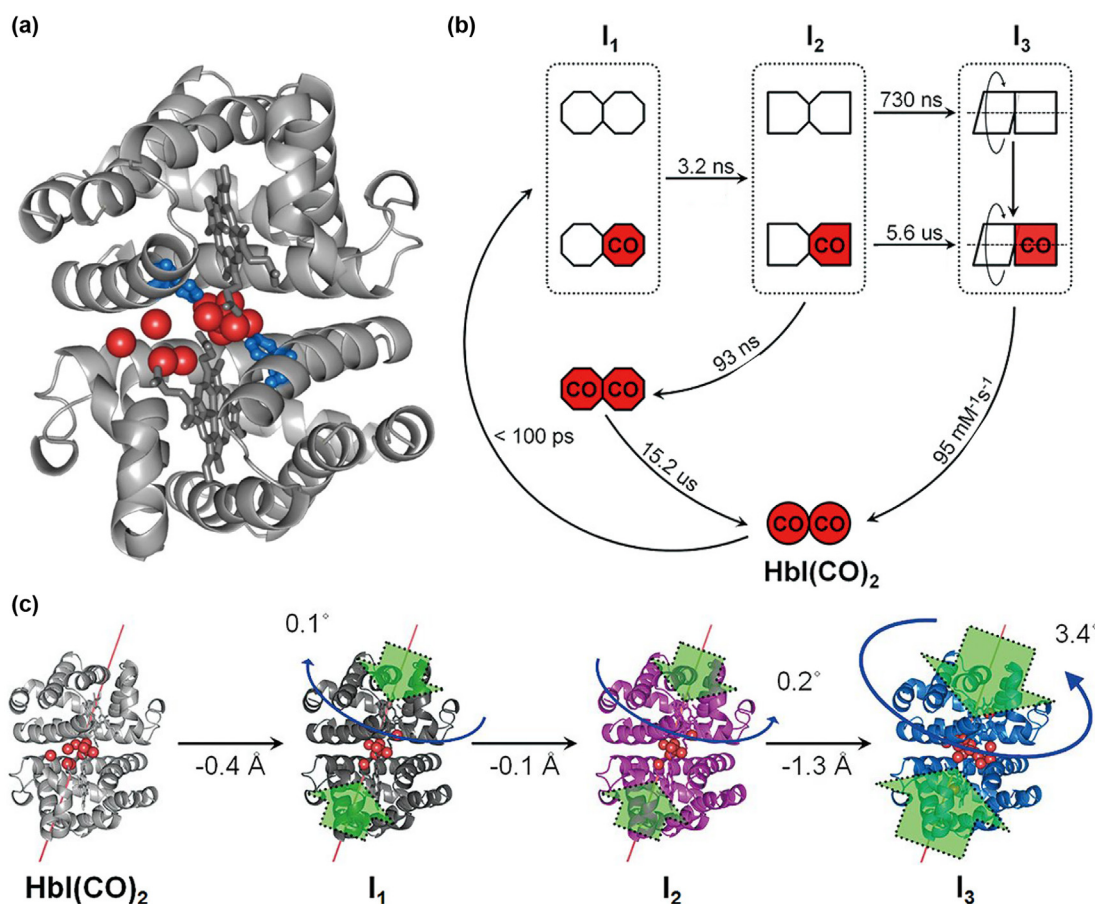


**FIG. 7.** (a) Molecular structure of HbI. Red spheres indicate interfacial water molecules. Phe97 residues, which were mutated for a comparative TRXL study, are shown in blue. (b) Kinetic model for the structural dynamics of WT HbI upon photoexcitation determined by a kinetic analysis of the TRXL data. Three reaction intermediates ( $I_1$ ,  $I_2$ , and  $I_3$ ) are identified from the TRXL data. (c) Structural change upon the photoexcitation of WT HbI determined via a structural analysis of the TRXL data. The subunit rotation (blue arrows) and heme-heme distance contraction (green arrows) are the movements relevant to the quaternary structural changes associated with the R-T transition. The transition from  $I_2$  to  $I_3$  shows a larger quaternary structural change compared to the other transitions, such as the transition from the R state to  $I_1$  and that from  $I_1$  to  $I_2$ , indicating that it corresponds to the R-T transition. Adapted with permission from Kim *et al.*, J. Am. Chem. Soc. **134**, 7001 (2012). Copyright 2012 American Chemical Society.

and thus transport these substances. The ligand-binding phenomenon of HbI shares similar properties with that of Hb in terms of cooperative ligand binding.<sup>135</sup> As with Hb, HbI has cooperative ligand binding, where the oxygenated state (R state) has a high ligand affinity, and the deoxygenated state (T state) has a low ligand affinity,<sup>136</sup> and the R-T transition of HbI can be triggered by photoexcitation. Compared to Hb, with a complicated, heterotetrameric structure, HbI has a simpler structure, making HbI attractive for investigating cooperative ligand binding. Accordingly, HbI has been investigated via time-resolved optical spectroscopic methods and TRXC.<sup>49–51,137–139</sup> Still, the detailed structural dynamics of HbI in solution remained elusive until TRXL was applied to HbI. In addition, TRXL experiments on several mutants were conducted for comparative studies, from which it was possible to unveil how the residues affect the structural dynamics associated with the R-T transition of HbI.

A TRXL study on WT  $\text{HbI}(\text{CO})_2$  at a synchrotron unveiled the structural dynamics of HbI from  $\sim 100$  ps to 10 ms.<sup>66</sup> It was confirmed

that HbI already shows a distinct TRXL signal at  $\sim 100$  ps, indicating that the structural change of HbI occurs within 100 ps. A kinetic analysis using SVD revealed that three reaction intermediates ( $I_1$ ,  $I_2$ , and  $I_3$ ) are involved in the structural dynamics of HbI in the time range from  $\sim 100$  ps to 10 ms [Fig. 7(b)]. The first intermediate,  $I_1$ , is formed within the time resolution ( $\sim 100$  ps), and then  $I_1$  transforms into the second intermediate,  $I_2$ , with a time constant of 3.2 ns. Via geminate recombination, a portion of  $I_2$  is recovered to the ground state, passing through  $I_1$ . The remaining fraction of  $I_2$  makes a biphasic transition (730 ns and 5.6  $\mu$ s) to  $I_3$ . A laser fluence dependence experiment verified that the fast and slow components of the biphasic transition correspond to transitions of the fully and partially photolyzed forms of HbI, respectively. Although the time constants for the  $I_2$ -to- $I_3$  transition of the fully and partially photolyzed forms are different, the TRXL signals for the two forms are the same. The identical TRXL signals of the two forms indicate that the partially and fully photolyzed forms have the same structure, confirming a cooperative structural change.

Finally, the recovery of the ground state occurs through the bimolecular recombination of  $I_3$  and the CO molecules. A structural analysis was performed using structure refinement aided by Monte Carlo simulations using rigid body modeling. According to the analysis results, during the formation of  $I_1$  and  $I_2$ , the quaternary structural change is not large, as the heme–heme distance slightly decreases, and the subunit rotation has hardly occurred [Fig. 7(c)]. In contrast, for the formation of  $I_3$ , the subunit rotates by  $3.5^\circ$ , and the heme–heme distance decreases more than in  $I_1$  and  $I_2$ . The subunit rotation in the solution phase is larger than that in the crystalline phase ( $\sim 0.6^\circ$ ), which was reported by a TRXC study.<sup>49</sup>

TRXL studies on Hbl were carried out not only for WT but also for various mutants, including F97Y, T72V, I114F, and K30D, which enhanced the understanding of the structural dynamics of Hbl

[Fig. 8(a)]. Phe97 is a residue near the interface [Fig. 8(a)]. It was reported that the flipping of Phe97 occurs during the R–T transition of Hbl, changing the orientation of the side chain from the interface-facing conformation to the inward-facing conformation.<sup>140</sup> It was known that such a change affects the entry of interfacial water molecules located between subunits and the ligand-binding affinity. Since the flipping of Phe97 is absent in the F97Y mutant, the effect of Phe97 flipping on structural dynamics can be unraveled by comparing the structural dynamics of F97Y and WT.<sup>66</sup> According to the kinetic analysis results for the F97Y mutant, F97Y and WT have the same kinetic framework, but the rate constants for the transitions are different. Notably, the CO recombination rate is larger in F97Y by  $\sim 10$  times. In addition to similar kinetic frameworks, the  $I_1$  and  $I_2$  of F97Y ( $I_1^{F97Y}$  and  $I_2^{F97Y}$ ) have similar SADSs to those of  $I_1^{WT}$  and  $I_2^{WT}$ , respectively.

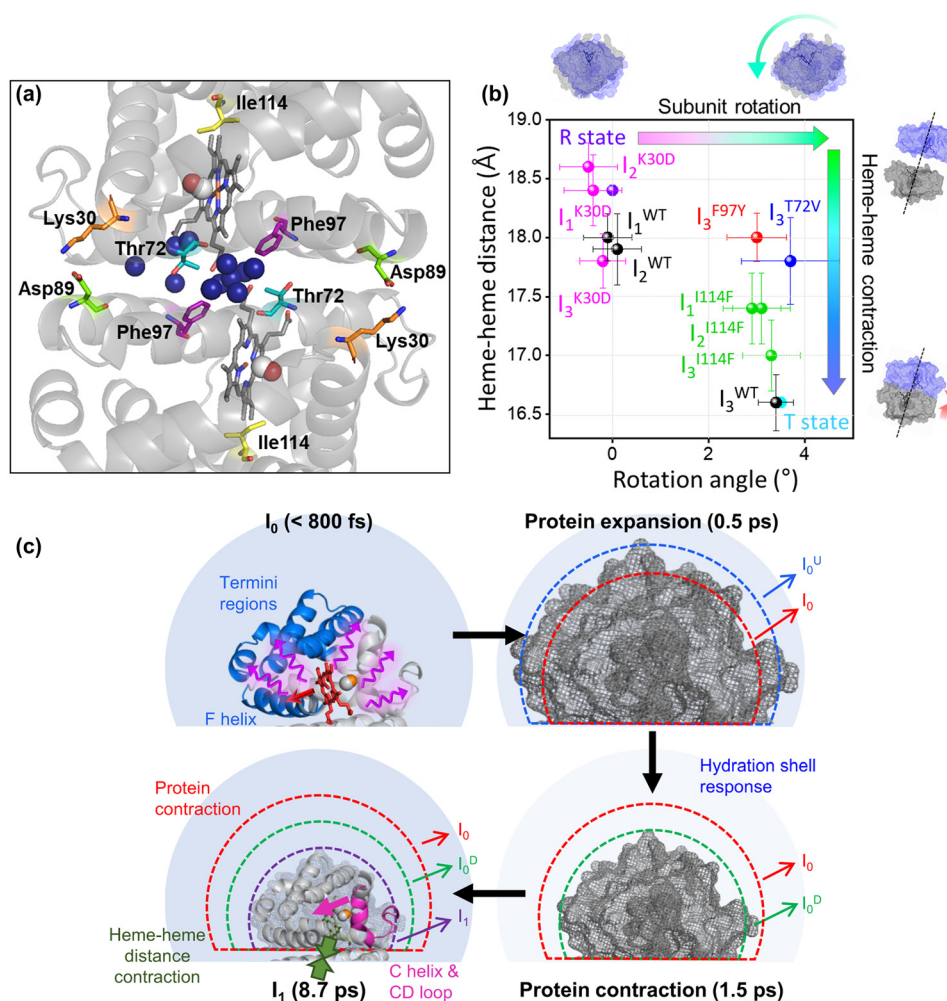


**FIG. 8.** (a) Structure of WT Hbl and residues mutated for comparative TRXL studies. The residues mutated for comparative TRXL studies, such as Phe97, Thr72, Ile114, and Lys30, are shown. Asp89, which forms the salt bridge with Lys30, is also shown. Blue spheres are the interfacial water molecules. The backbone and heme groups of Hbl are shown in translucent gray ribbon and stick representation, respectively. The carbon and oxygen atoms of carbon monoxide molecules near the heme groups are represented with translucent gray and red spheres. (b) Changes in the quaternary structures of various mutants investigated using TRXL. (c) Schematic for the ultrafast structural dynamics of Hbl revealed by fs-TRXL on WT Hbl. Reproduced from Lee *et al.*, Nat. Commun. 12, 3677 (2021). Copyright 2021 Authors, licensed under a Creative Commons Attribution (CC BY) License.



In contrast, the SADS of  $I_3^{F97Y}$  has an opposite sign to that of  $I_3^{WT}$ , in the SAXS region. This difference in the SAXS region was interpreted in terms of interfacial water molecules. The number of interfacial water molecules increases during the R–T transition in WT, whereas it decreases in F97Y. Based on the structural analysis, it was reported that  $I_3^{F97Y}$  has a subunit rotation angle similar to  $I_3^{WT}$  but a smaller change in the heme–heme distance than WT. It was suggested that the absence of the flipping of Phe97 hinders the heme–heme distance contraction [Fig. 8(b)]. In addition, the long heme–heme distance of  $I_3^{F97Y}$ , which is close to that of the R state, seems to promote bimolecular CO recombination.

Thr72 is a residue participating in the hydrogen bond of interfacial water [Fig. 8(a)]. A crystallographic study reported that the T72V mutant in the deoxy state has two fewer interfacial water molecules than WT and greater cooperativity between two subunits than that in WT.<sup>141</sup> A TRXL study on T72V unraveled how such a change in the interfacial water molecules affects the structural dynamics of HbI.<sup>142</sup> According to the kinetic analysis, T72V has the same kinetic framework as WT, but the kinetic parameters show some differences. In T72V, the rate ratio of the two kinetic components for the biphasic  $I_2$ -to- $I_3$  transition (slow component/fast component) is decreased, and the rate of bimolecular CO recombination is accelerated. The reduced rate ratio of the biphasic transition means that the larger cooperativity of T72V facilitates the  $I_2$ -to- $I_3$  transition of the partially photolyzed form, such that the difference in the transition speeds between the partially and fully photolyzed forms is reduced. The SADSs of  $I_1^{T72V}$  and  $I_2^{T72V}$  are similar to those of WT, indicating that the structures of  $I_1^{T72V}$  and  $I_2^{T72V}$  are similar to those of  $I_1^{WT}$  and  $I_2^{WT}$ , respectively. Still, the SADS of  $I_3^{T72V}$  is different from that of  $I_3^{WT}$ , implying that  $I_3^{T72V}$  has a different structure from  $I_3^{WT}$ . The refined structure of  $I_3^{T72V}$  indicates that subunit rotation occurs at a similar level to that of  $I_3^{WT}$ , but the heme–heme distance contraction is less significant than that of  $I_3^{WT}$  [Fig. 8(b)]. In addition, the distance between the E and F helices is less increased in  $I_3^{T72V}$  than in  $I_3^{WT}$ . A crystallographic study elucidated that the distance between the E and F helices increases in the R–T transition, which accompanies the decrease in ligand affinity.<sup>51</sup> The shorter E–F distance and accelerated bimolecular CO recombination of  $I_3^{T72V}$  compared to  $I_3^{WT}$  agree with the negative correlation between the E–F distance and ligand affinity observed in the crystallographic study.

Ile114 is related to the migration of CO in HbI and located in the channel through which the dissociated CO moves from the primary docking site to the secondary docking site [Fig. 8(a)]. With Ile114 residue mutated into a bulky Phe residue, the I114F mutant inhibits ligand migration.<sup>143</sup> In addition, it was reported that the I114F mutation hinders ligand-related heme movement, and the liganded state of I114F has a structure similar to that of the T state structure of WT.<sup>143</sup> A TRXL study on I114F unveiled how the inhibition of ligand migration and the changes in the liganded structure affect the structural dynamics of HbI.<sup>144</sup> The kinetic framework of I114F elucidated by TRXL resembles that of WT, but the geminate recombination of I114F occurs immediately in the  $I_1$  state, as opposed to WT, whose geminate recombination occurs in  $I_2$ . The rates of the  $I_1$ -to- $I_2$  transition and bimolecular CO recombination are decelerated, suggesting that these processes are related to the migration of the ligand between the primary and secondary docking sites. Furthermore, the SADSs of I114F have smaller amplitudes than those of WT. In particular, the SADS of

$I_3^{I114F}$  has a similar shape to that of  $I_3^{WT}$ , but its amplitude is approximately 2.8 times smaller. In fact, in the intermediate structures of I114F obtained from structure refinement, the changes in the quaternary structures are smaller than those of WT [Fig. 8(b)]. It was suggested that the structural similarity between the liganded state of I114F and the T state of WT accounts for the small structural change in I114F.

The Lys30 of HbI forms a salt bridge with the Asp89 of the other subunit, affecting the dimer formation of HbI [Fig. 8(a)].<sup>145</sup> Since the salt bridge is absent in the K30D mutant, a TRXL study on K30D could unveil how the salt bridge affects the structural dynamics of HbI.<sup>146</sup> For a kinetic analysis of the TRXL data from K30D, a kinetic model considering the contributions from both a dimer and a monomer was used, as opposed to other studies where only the dimer was considered. The dimer of K30D has the same kinetic framework as that of WT, but the detailed reaction rates differ. For example, the  $I_2$ -to- $I_3$  biphasic transition of K30D is accelerated compared to that of WT, and the bimolecular CO recombination is slower. Furthermore, according to the structural analysis,  $I_3^{K30D}$  has a remarkably different structure from  $I_3^{WT}$ . While  $I_3^{WT}$  has a T-like structure,  $I_3^{K30D}$  has an R-like structure, which exhibits a small root mean square deviation (RMSD) against the crystal structure of the R state and a small quaternary structural change compared to the liganded state [Fig. 8(b)]. The acceleration of the  $I_2$ -to- $I_3$  transition in K30D compared to WT was explained through the structural changes extracted from the structural analysis. As opposed to  $I_2^{WT}$  and  $I_3^{WT}$ , which have R-like and T-like structures, respectively, both  $I_2^{K30D}$  and  $I_3^{K30D}$  have R-like structures. Such a structural similarity between  $I_2^{K30D}$  and  $I_3^{K30D}$  leads to the acceleration of the  $I_2$ - $I_3$  transition in K30D. However,  $I_3^{K30D}$  has a slower CO recombination than  $I_3^{WT}$ , even though  $I_3^{K30D}$  has a more similar structure to the R state with a higher ligand affinity. It was suggested that this phenomenon indicates that the absence of the salt bridge interferes with ligand binding in K30D. It was also suggested that the salt bridge plays a critical role in the allosteric transition of HbI and that the inhibited formation of the salt bridge in K30D can cause a decrease in quaternary structural changes.

The TRXL studies on HbI were typically performed at synchrotrons, and the limited time resolution did not allow for exploring the ultrafast structural dynamics of HbI earlier than 100 ps. Later, the ultrafast structural dynamics of HbI were unveiled via an fs-TRXL experiment at an XFEL [Fig. 8(c)].<sup>133</sup> As discussed for Mb, it had been suggested that changes in the hydration shell can significantly influence the SAXS data of an fs-TRXL experiment.<sup>132</sup> Considering this argument, prior to the analysis, simulations were performed to generate difference scattering curves, assuming that the structural changes in the protein are the same but that the electron density changes of the hydration shell are different. The results indicated that the change in the hydration shell significantly affects the SAXS region of the difference scattering curve but not the WAXS region. These simulation results were taken into account, and accordingly, a protein structure analysis was performed using fs-TRXL data in the WAXS region only, without including the SAXS region. A kinetic analysis on the WAXS region of the fs-TRXL data identified  $I_0$ , an intermediate preceding  $I_1$ . In addition, the TRXL signal deviated from exponential behavior in the ultrafast time domain, implying that a coherent motion of HbI occurs. The structure refinement revealed that some structural change in the entire protein has already occurred during the formation of  $I_0$ .

This ultrafast global structural change in HbI was explained as a result of the protein quake, in which the structural change initiated from the heme group is rapidly transferred to the whole protein in a way similar to the propagation of a wave. In addition, it was revealed that overall protein expansion and contraction occur in the ultrafast time domain ( $<3$  ps), where coherent motion exists. Then,  $I_0$  transforms into  $I_1$ , the intermediate observed in the synchrotron-based TRXL, with a time constant of 8.7 ps. During the  $I_0$ -to- $I_1$  transition, the protein contraction and the movements of the C helix and CD loop region are observed. In addition to protein structure, the change in the electron density of the hydration shell upon photoexcitation was tracked using the TRXL data in the SAXS region, which is significantly affected by changes in the hydration shell according to the simulation results. The electron density of the hydration shell initially decreases after photoexcitation up to  $\sim 1.5$  ps, and then it increases along with the formation of  $I_1$ .

#### 4. Cytochrome c

Cytochrome c (Cyt-c) plays a role in various biological phenomena, such as electron transfer in mitochondria and cell apoptosis. Cyt-c has a heme group as a cofactor [Fig. 9(a)], and its function and structure

are significantly affected by the ligation state of the heme group. For example, in the native structure, the iron atom of the heme group has a hexa-coordinated structure.<sup>147</sup> In this conformation, Met80 and His18 residues are bound as axial ligands, and cyt-c serves as an electron transfer protein. When the Fe-S bond between the heme group and Met80 is dissociated, cyt-c can act as a peroxidase.<sup>148,149</sup> Meanwhile, the protein folding of cyt-c can be triggered by a change in the ligation state. For example, when cyt-c has an unfolded structure, the heme group can bind to small molecules, such as carbon monoxide. When the heme group is excited, Fe-CO bond dissociation occurs, followed by protein folding through the ligation of Met80. During the folding, not only native ligation, where Met80 binds to the heme group, but also non-native ligation, where residues such as His26 bind to the heme group, can occur.<sup>150–153</sup> Due to the characteristics of cyt-c that a change in function and protein folding can be readily induced, cyt-c has been investigated intensively as a model system to study protein structural dynamics.<sup>154–156</sup> Likewise, since the development of TRXL on proteins, many TRXL studies have been performed on cyt-c.<sup>39,157–159</sup>

For example, a TRXL study was performed to study the folding dynamics of cyt-c upon the change in the ligation state of the heme group.<sup>158</sup> In this study, x-ray transient absorption (XTA), also known

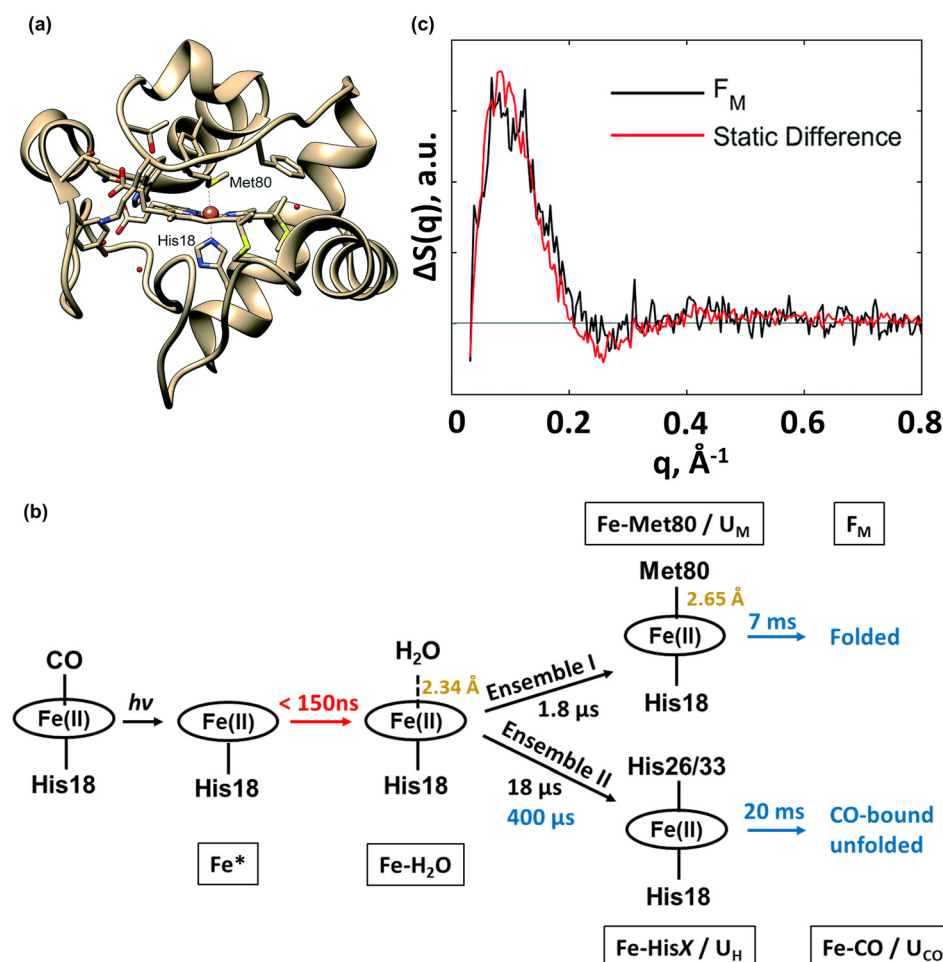


**FIG. 9.** (a) Molecular structure of cyt-c. (b) Folding pathway of cyt-c upon photoexcitation proposed via XTA and TRXL. The intermediates are labeled in the boxes below the molecular structure around the heme group. The processes shown in black are those observed via both techniques, whereas those shown in red and blue are processes observed by only XTA and TRXL, respectively. (c) Comparison between the SADS of  $F_M$  and the experimental difference scattering curve calculated using the static scattering curves of the folded and unfolded states of cyt-c. Adapted from Hsu *et al.*, Chem. Sci. **10**, 9788 (2019). Copyright 2019 Authors, licensed under a Creative Commons Attribution (CC BY) License.



as time-resolved x-ray absorption spectroscopy, and TRXL were combined to clarify the detailed structural dynamics of protein folding by investigating both the local structural changes around the heme group and the global structural changes in the protein. The XTA experiment unveiled the local structural changes, such as the change in the ligation state around the heme group. Based on the analysis of the XTA data, it was suggested that penta-coordinated species, water-ligated species, Met-ligated species, and His-ligated species are involved in the reaction dynamics [Fig. 9(b)]. The Met-ligated species and His-ligated species correspond to  $U_M$  and  $U_H$ , respectively, identified in a TRXL experiment which will be introduced shortly. The Fe-S bond length of the Met-ligated species obtained from the XTA experiment is 2.65 Å, which is 0.36 Å longer than that of the native state. The TRXL experiment revealed a global structural change accompanied by a change in the ligation state of the heme group. A kinetic analysis of the TRXL data identified three reaction intermediates ( $U_M$ ,  $F_M$ , and  $U_H$ ) [Fig. 9(b)].  $U_M$ , formed with a time constant of 1.8  $\mu$ s, was assigned to be the Met-ligated species based on a comparison to the time constant obtained from the XTA experiment results. Based on a SAXS region analysis, it was suggested that  $U_M$  has a partially folded state that is more compact than the ground state (unfolded state) but more flexible than the folded state.  $U_M$  is transformed into  $F_M$  with a time constant of 6.6 ms. The SADS of  $F_M$  shows good agreement with the difference scattering curve between the folded and unfolded states of cyt-c, which was obtained from a static x-ray scattering experiment [Fig. 9(c)]. In addition, the cyt-c in the  $F_M$  state is more compact than that in  $U_M$ , and has a similar protein size to that of the folded state. Based on these results,  $F_M$  was assigned to the folded state. The formation of  $U_M$  prior to  $F_M$  indicates that the native folded conformation is not formed immediately after Fe-Met ligation but that additional rearrangement is required after the ligation. The  $U_H$  state is formed in a parallel manner to the formation of  $U_M$ , and its formation is biphasic, with time constants of 18 and 400  $\mu$ s. Based on a comparison with the previously known time constants for His ligation and the time constant identified in the XTA experiment,  $U_H$  was assigned to the His-ligated species. The SADS of this state exhibits negative features in the SAXS region, indicating that the protein is expanded and disordered. The  $U_H$  decays to the ground state with a time constant of 20.4 ms without transition to the native folded structure. In terms of thermodynamics, the Fe-His bond is more favorable than the Fe-Met bond. Nevertheless, the intermediates with the Fe-Met bond (the  $U_M$  and  $F_M$  states) are observed according to XTA and TRXL data. The structural heterogeneity of the protein was suggested as a reason for the formation of the Fe-Met bond in the  $U_M$  and  $F_M$  states. The CO-bound unfolded state of cyt-c can have multiple conformations. Among them, for a population with a local structure in which the binding of Fe-Met80 is favorable, the Fe-Met80 bond would be formed upon photoexcitation, and protein folding would occur. Otherwise, Fe-His bond formation would occur, leading to misligation.

TRXL was also used to scrutinize the effect of misligation by His residues on protein folding dynamics.<sup>157</sup> As imidazole and histidine have similar molecular structures, imidazole can transiently bind to the heme group to prevent misligation with His residues. From a TRXL study performed on a CO-ligated cyt-c sample with and without imidazole [Fig. 10(a)], the effect of the presence of imidazole on the kinetics of protein folding was examined. In the case where imidazole was absent, the first and second rSVs of the TRXL data could be

described with three exponentials with time constants of 40  $\mu$ s, 2.3 ms, and 37 ms [Fig. 10(b)]. Because the time constant of 40  $\mu$ s is similar to the timescale where the misligation of His residues occurs,<sup>154,155</sup> this kinetic component was assigned to the misligation process. The TRXL signal corresponding to misligation was not observed when imidazole was present. Based on this result, it was suggested that misligation by His residues is inhibited in the presence of imidazole. Other kinetic components with 2.3 and 37 ms time constants were assigned to ligand replacement from the His residues to the Met residue and successive small structural changes, respectively. For the kinetic component with a time constant of 2.3 ms, the TRXL signal in the SAXS region ( $q < 0.25 \text{ \AA}^{-1}$ ) increases, which implies that the protein folding is accompanied by global structural changes. In the presence of imidazole, the first and second rSVs of the TRXL data can be described with two exponentials with time constants of 370  $\mu$ s and 56 ms [Fig. 10(b)]. The TRXL signal of the kinetic component with a time constant of 370  $\mu$ s is similar to that with a time constant of 2.3 ms, obtained from the TRXL experiment on a sample without imidazole, indicating that it corresponds to protein folding. Based on the smaller time constant for protein folding, it was suggested that protein folding is promoted when misligation is inhibited by imidazole. In the presence of imidazole, ligand replacement (from imidazole to Met) and successive structural changes involve one time constant (56 ms) rather than two.

Recently, with the development of XFELs, the ultrafast structural dynamics of cyt-c were investigated. This study elucidated the ligand dissociation dynamics of cyt-c in the native state via time-resolved x-ray emission spectroscopy (TR-XES) and TRXL.<sup>159</sup> Based on the TR-XES data, it was suggested that, upon the  $\pi$ - $\pi^*$  transition of the porphyrin ligand, cyt-c eventually forms a  $^5MC$  state via a  $^3MC$  state. It was argued that the  $^3MC$  state has a configuration of  $^3[d_\pi^3 d_{z^2}^1]$ , which has an antibonding  $\sigma^*$  character, thereby inducing Fe-S bond dissociation. Nevertheless, the detailed mechanism for the formation of these states was not clarified. The change in the protein structure upon photoexcitation was investigated via the TRXL signal. For a detailed structural analysis of the TRXL data, a structural model considering only the movements of the heme group and axial ligands was used [Fig. 11(a)]. Accordingly, a structural analysis was performed for the ultrafast time domain (<300 fs), assuming that the local structural change near the heme group is dominant in this time domain. The TRXL data in the ultrafast time domain could be explained by increased distances between the Fe atom and axial ligands such as Met80 and His18 [Fig. 11(b)]. For the later time domain, this simple structural model could not reproduce the experimental difference scattering curve well, implying that structural motions other than the simple Fe-ligand displacement participate in the dynamics.

## B. Photoreceptor proteins

### 1. Phytochrome

Phytochrome is a photoreceptor protein found in various organisms, from bacteria to plants.<sup>160,161</sup> It plays an important role in various biological functions, such as the seed germination of plants. Phytochrome has a dimeric structure, and a monomer is composed of photosensory and output domains. The photosensory domain of phytochrome typically consists of PAS (Per/Arndt/Sim), GAF (cGMP phosphodiesterase/adenyl cyclase/FhlA), and PHY (phytochrome-specific) domains.<sup>162</sup> The photosensory domain is linked to the output

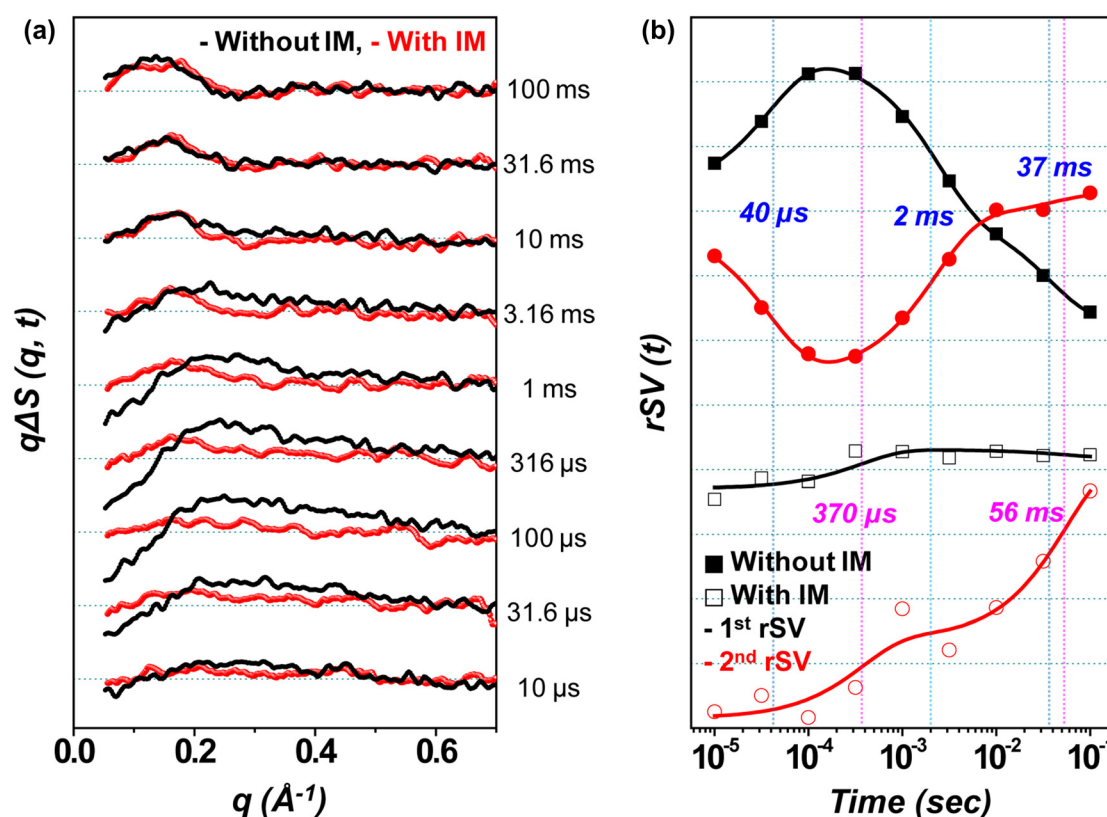


**FIG. 10.** (a) TRXL data from cyt-c without (black) and with (red) imidazole (IM) upon photoexcitation. (b) The first and second rSVs of the TRXL data from cyt-c without and with imidazole. The upper two curves are the first (black-filled squares) and second (red-filled circles) rSVs of the TRXL data from cyt-c without imidazole and their fits (black and red solid lines). The lower two curves are the first (black open squares) and second (red open circles) rSVs of the TRXL data from cyt-c with imidazole and their fits (black and red solid lines). The time constants from the fits are also shown. Reproduced with permission from Kim *et al.*, Bull. Korean Chem. Soc. **35**, 697 (2014). Copyright 2014 Korean Chemical Society.

domain that performs a catalytic function through the PHY domain. Phytochrome has a biliverdin chromophore, and the chromophore is usually present in the PAS–GAF domain. According to the consensus of several phytochromes, the isomerization of a double bond of the chromophore occurs during photoexcitation. The isomerization of the chromophore induces the structural change in the entire protein as well.<sup>163,164</sup> For the bacterial phytochrome superfamily, the proteins are classified into two types, canonical and bathy, according to their photoconversion properties.<sup>165–167</sup> Canonical bacterial phytochromes adopt the Pr state as the parental state, which converts into the Pfr state by absorbing red light. Upon the absorption of far-red light, the Pfr state is converted back into the Pr state. In contrast, bathy bacterial phytochromes adopt the Pfr state as the parental state, and the Pfr state is converted into the Pr state by absorbing far-red light. The Pr state returns to the Pfr state by absorbing red light. Although phytochrome performs various biological roles and has photochromic dynamics, few studies directly had visualized the structural dynamics of phytochrome. In addition, in contrast to the heme proteins introduced in Sec. IV A, phytochromes under physiological conditions are naturally photoactive and perform their functions via photoexcitation. In this regard, the TRXL studies on phytochrome provided an opportunity to reveal the biologically relevant movement of phytochrome by

using the advantage that the TRXL signal is directly sensitive to the structural change in the protein.<sup>168–172</sup>

*a. Phytochrome from Deinococcus radiodurans.* The first TRXL study on phytochromes was performed on the canonical bacterial phytochrome from *D. radiodurans*, which was known to undergo a photo-induced Pr-to-Pfr transition.<sup>168</sup> The TRXL signal rose with a time constant of 4.3 ms, similar to the formation time for the Pfr state observed in a spectroscopic experiment. The difference scattering curve obtained from the TRXL experiment was in agreement with the difference between static scattering curves before and after light illumination. In this study, crystallography was also used to scrutinize the structural change in the photosensory domain upon irradiation. The crystal structures obtained for the dark and illuminated states, which can represent the Pr and Pfr states, respectively [Fig. 12(a)], show that the structures of the tongue regions of the PHY domains are changed from a  $\beta$  sheet conformation to an  $\alpha$  helix conformation upon light illumination, resulting in the opening of the dimeric photosensory domain. Based on this information, MD simulations were performed on the two crystal structures to uncover the structural change in phytochrome in the solution phase. Among the structures obtained from the MD simulations, those that reproduced the experimental

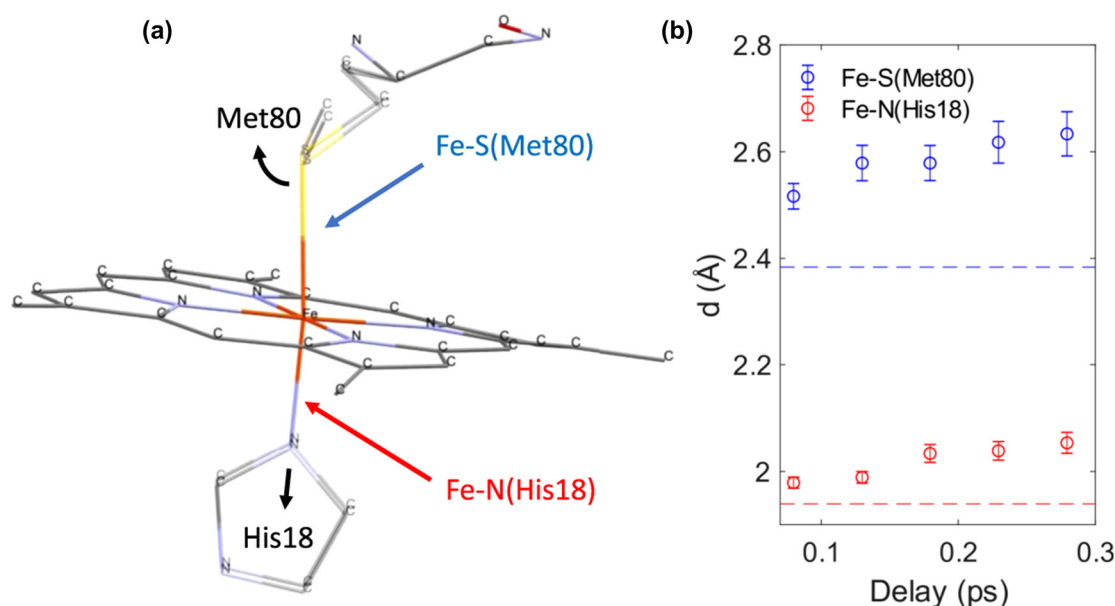


**FIG. 11.** (a) Structure representation of cyt-c used for the structure refinement on the fs-TRXL data. The translation of His18 and rotation of Met80, which are shown with black arrows, were considered during the structure refinement. Such movements induced the change of the distances from the iron atom to the axial ligands, the Fe-N distance for His18 (red) and the Fe-S distance for Met80 (blue). (b) The distances between the heme group and axial ligands over time obtained from the analysis of the fs-TRXL data. The Fe-S and Fe-N distances are shown in blue and red, respectively. The dashed lines indicate the Fe-S (blue) and Fe-N (red) distances in the ground state. Reproduced from Reinhard *et al.*, Nat. Commun. **12**, 1086 (2021). Copyright 2021 Authors, licensed under a Creative Commons Attribution (CC BY) License.

difference scattering curve corresponding to the Pr-to-Pfr transition were selected. The experimental difference scattering curve used for the structure refinement was generated from the x-ray scattering curves of the Pr and Pfr states obtained from a static x-ray scattering experiment rather than the TRXL experiment. The structure refinement revealed that a similar but larger structural change occurs in the solution phase compared to that observed in the crystalline phase [Fig. 12(b)]. It was suggested that such a structural change in the photosensory domain induces the conformational change in the output domain, which performs catalytic functions.

In a subsequent study, which combined TRXL and Fourier transform infrared (FTIR) spectroscopy, it was investigated whether the dimeric interface played an important role in the activation of phytochrome by mutating residues at the interface of the photosensory domain to generate a monomeric structure.<sup>169</sup> The rise of the TRXL signal of the monomeric photosensory domain was delayed by an order of magnitude compared to that of the dimeric photosensory domain. Structure refinement was performed using MD simulations similar to the case of the dimeric photosensory domain. Among the structures obtained from the MD simulations, those capable of describing the experimental difference scattering curve of the Pf-to-Pfr transition were selected. These structures show the bending of the monomeric structure along the long scaffolding helix and the twist motion of the PHY domain during the Pr-to-Pfr transition [Fig. 12(c)]. Additionally, in the FTIR experiment, the structural change in the tongue region from a  $\beta$  sheet to an  $\alpha$  helix was observed. Such a structural change is similar to that obtained from the TRXL study on the dimeric photosensory domain. Based on the comparison of kinetics and structural changes between the dimeric and monomeric photosensory domains, it was

suggested that the interaction between the monomers in a dimer affects the kinetics of the structural change rather than the structural change in the photosensory domain itself. In addition, the fact that the dimeric interface does not significantly affect the structural change may indicate that various dimeric photosensory domains can have a common structural change in the monomeric photosensory domain, although their dimeric interfaces are different.

In addition to the TRXL study on the photosensory domain, there is a study that used TRXL and transient absorption (TA) and compared the structural dynamics of the full-length bacterial phytochrome with those of the PAS-GAF domain and the PAS-GAF-PHY domain.<sup>170</sup> The TRXL data from the full-length protein show almost no distinct signal in the microsecond time domain but a large change in the millisecond time domain. Likewise, the TRXL signals of the PAS-GAF and PAS-GAF-PHY domains emerge on millisecond time scales. Based on this observation, it was suggested that the structural change in the PAS-GAF domain binding the chromophore is the rate-limiting step in the millisecond time domain. The time domain in which the TRXL signal shows a large change is similar to that for the formation of the meta-Rc state, which accompanies the transfer of protons from the protein to the surroundings. The Guinier analysis and low-resolution structure reconstruction were performed using SAXS data of the Pr and Pfr states to elucidate the detailed structural changes occurring in the full-length protein. The SAXS curve of the Pfr state used for the structure refinement was obtained using the difference scattering curves in the millisecond timescale and the static SAXS curve of the Pr state. The Guinier analysis results indicated that the Pr and Pfr states have a similar  $R_g$  and volume. The low-resolution structure reconstruction identified a concerted motion of the photosensory domain and the



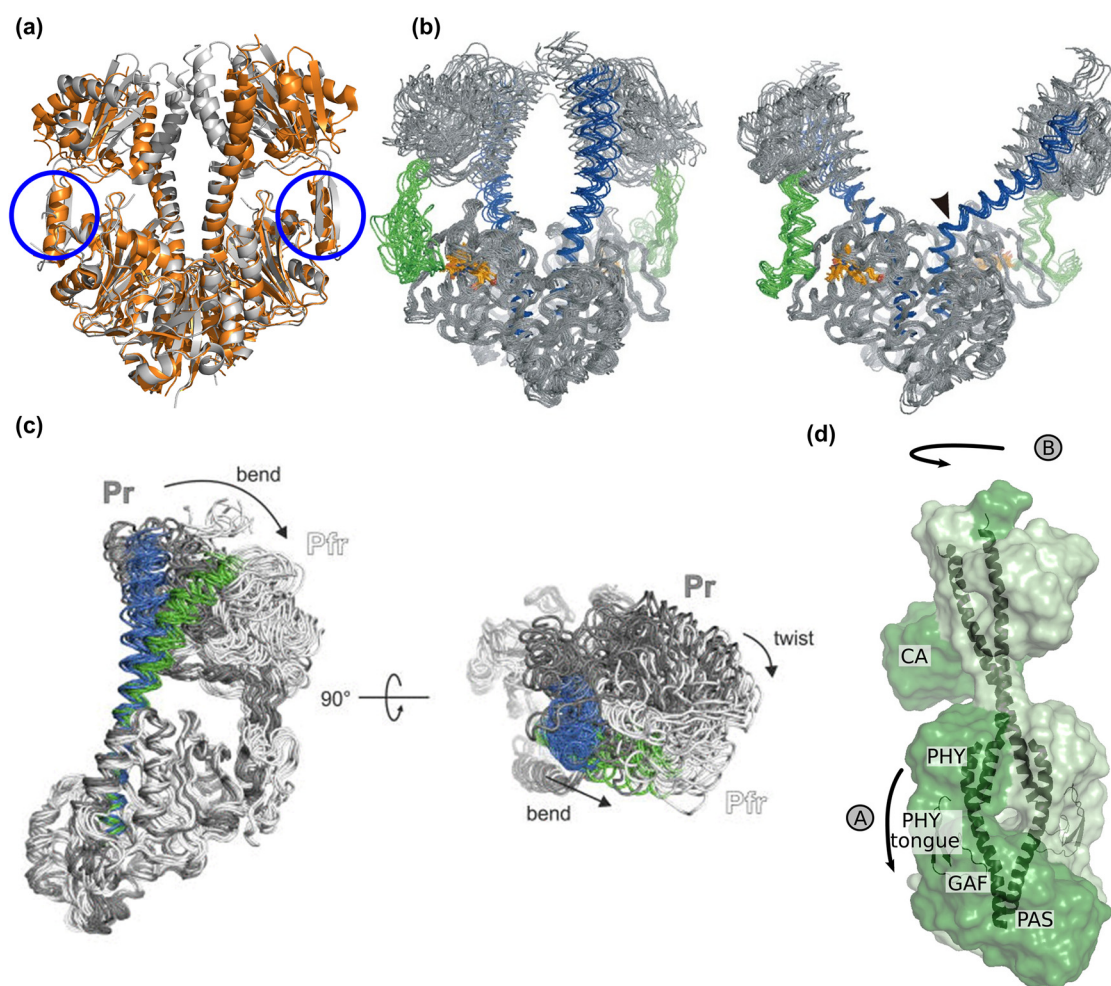


**FIG. 12.** (a) Crystal structures of the dimeric photosensory domain of the canonical bacterial phytochrome from *D. radiodurans* in the dark (gray) and illuminated (orange) states. The tongue regions of the PHY domains, of which the structure changes from a  $\beta$  sheet conformation to an  $\alpha$  helix conformation upon illumination, are marked with blue circles. (b) Structures for the Pr (left) and Pfr (right) states obtained from the structure refinement. The structure refinement was performed using the experimental difference scattering curve generated from a static x-ray scattering experiment on the dark and illuminated states. The chromophores, the PHY domains, and the scaffolding helices, which connect the PHY and PAS-GAF domains, are shown in orange, green, and blue, respectively. Reproduced with permission from Takala *et al.*, Nature **509**, 245 (2014). Copyright 2014, Nature Publishing Group. (c) Structures of the monomeric photosensory domain of the canonical bacterial phytochrome from *D. radiodurans* in the Pr and Pfr states obtained by TRXL. The structures representing the Pr and Pfr states are shown in gray and white, respectively. The scaffolding helices of the Pr and Pfr states are shown in blue and green, respectively. Reproduced from Takala *et al.*, Struct. Dyn. **3**, 054701 (2016). Copyright 2016 Authors, licensed under a Creative Commons Attribution (CC BY) License. (d) Structural change in the full-length bacterial phytochrome from *D. radiodurans* upon the Pr-to-Pfr transition. The arrow A indicates the rotation of the photosensory domain, and B indicates the rotation of the output domain. Reproduced from Björling *et al.*, Sci. Adv. **2**, e1600920 (2016). Copyright 2016 Authors, licensed under a Creative Commons Attribution 4.0 License.

output domain, as well as the rotation of the output domain during the Pr-to-Pfr transition [Fig. 12(d)].

*b. Phytochrome from Synechocystis sp. PCC6803.* In addition to the bacterial phytochrome, TRXL was applied to the full-length phytochrome and photosensory domains of a cyanobacterial phytochrome from *Synechocystis sp. PCC6803*.<sup>171</sup> The TRXL data indicated that the cyanobacterial phytochrome has different structural dynamics from the bacterial phytochrome. For example, the photosensory domain and the output domain of the bacterial phytochrome show a concerted motion. In contrast, the movements of the two domains occur

sequentially for the cyanobacterial phytochrome. Based on an SVD analysis of the TRXL data, it was suggested that both the photosensory domain and the full-length protein have three significant SVD components. The second and third ISVs of the TRXL data from the full-length protein, which are associated with the TRXL data in the time domain from microseconds to milliseconds, are similar to the second and third ISVs of the data from the photosensory domain, respectively [Fig. 13(a)]. In addition, the third ISV of the data from the full-length protein is similar to the TRXL signal obtained from the photosensory domain of the bacterial phytochrome [Fig. 13(a)]. Based on these similarities, the second and third SVD components of the data from the

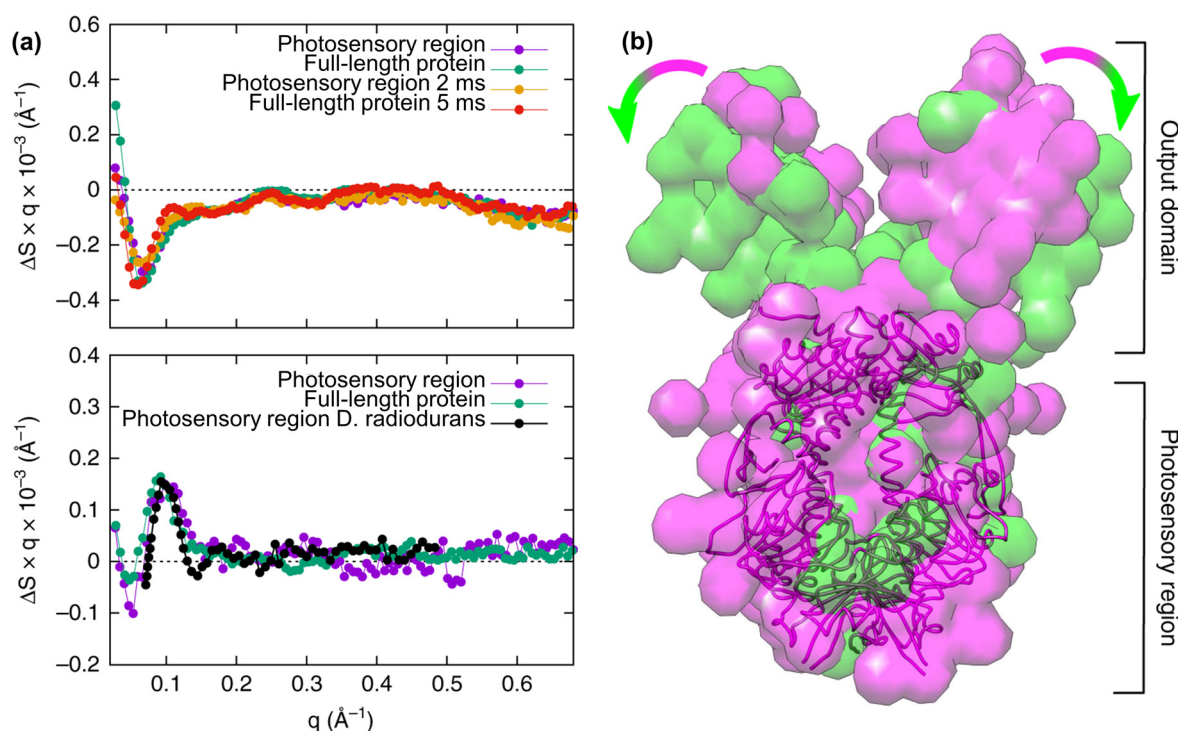


**FIG. 13.** (a) (Top) Comparison of the second ISVs of the TRXL data from the full-length protein and the photosensory domain of the cyanobacterial phytochrome from *Synechocystis* sp. PCC6803 with the TRXL data. (Bottom) Comparison of the third ISVs of the TRXL data from the full-length protein and the photosensory domain of the cyanobacterial phytochrome with the TRXL data from the photosensory domain of the bacterial phytochrome. (b) Structural change in the cyanobacterial phytochrome upon the Pr-to-Pfr transition obtained via TRXL. Low-resolution structures for the Pr and Pfr states are shown in pink and green, respectively. Adapted from Heyes *et al.*, *Commun. Biol.* **2**, 1 (2019). Copyright 2019 Authors, licensed under a Creative Commons Attribution (CC BY) License.

full-length protein were assigned to the movement of the photosensory domain. In contrast, the first ISV, responsible for the TRXL data at several hundred milliseconds, shows different characteristics for the photosensory domain and full-length protein. Based on this difference, the first SVD component of the data from the full-length protein was assigned to the movement of the output domain, which does not occur in a concerted manner with the structural change in the photosensory domain. The different structural dynamics of the bacterial phytochrome and the cyanobacterial phytochrome suggest that proteins belonging to the phytochrome family may have different reaction pathways. Detailed structural changes during the Pr-to-Pfr transition of the cyanobacterial phytochrome were elucidated via the low-resolution structure reconstruction using static x-ray scattering curves of the Pr and Pfr states. The result showed that the opening motion of the dimeric interface of the output domain occurs during the Pr-to-Pfr transition [Fig. 13(b)].

*c. Phytochrome from Pseudomonas aeruginosa.* A TRXL study was also performed on the dimeric photosensory domain of a bathy phytochrome from *P. aeruginosa*, not a canonical phytochrome.<sup>172</sup> A kinetic analysis of the TRXL data showed that the final photoproduct (the P state) is formed with a time constant of 21 ms via the Pfr-to-Pr transition, which is similar to the time for the Pr state formation observed in a spectroscopic study.<sup>173</sup> To investigate the structural properties involved in the Pfr-to-Pr transition of the protein, a structural analysis guided by MD simulations was conducted on the TRXL data.

For the MD simulations, the previously reported crystal structures of bacterial phytochromes were classified into three representative structural frames according to the conformations of the helical backbones in their photosensory domains: (i) II-frame, (ii) O-frame, and (iii) Y-frame [Fig. 14(a)]. Based on this structural information, various candidate structures targeting the three different frames were generated through the MD simulations, and the optimal structures for the Pfr-to-Pr transition were obtained from the combination of the candidate structures. The optimal structures demonstrated that the photoconversion of the bathy bacterial phytochrome involves a structural transition from the II-framed Pfr state to the O-framed Pr state [Fig. 14(b)]. This conformational change in the bathy bacterial phytochrome is different from those of other canonical bacterial phytochromes involving the structural transition from the O-framed Pr state to the Y-framed Pfr state, suggesting that the photoconversion of canonical and bathy bacterial phytochromes involves different global conformational changes.

## 2. Retinylidene proteins

Retinylidene proteins, which have retinal chromophores, participate in molecular pumps and signal transduction processes. For example, bacteriorhodopsin (bR), found in some archaea, and proteorhodopsin (pR) of marine organisms, transport protons upon photoexcitation,<sup>174,175</sup> and rhodopsin, found in the vertebrate, plays an important role in vision by performing signal transduction as a



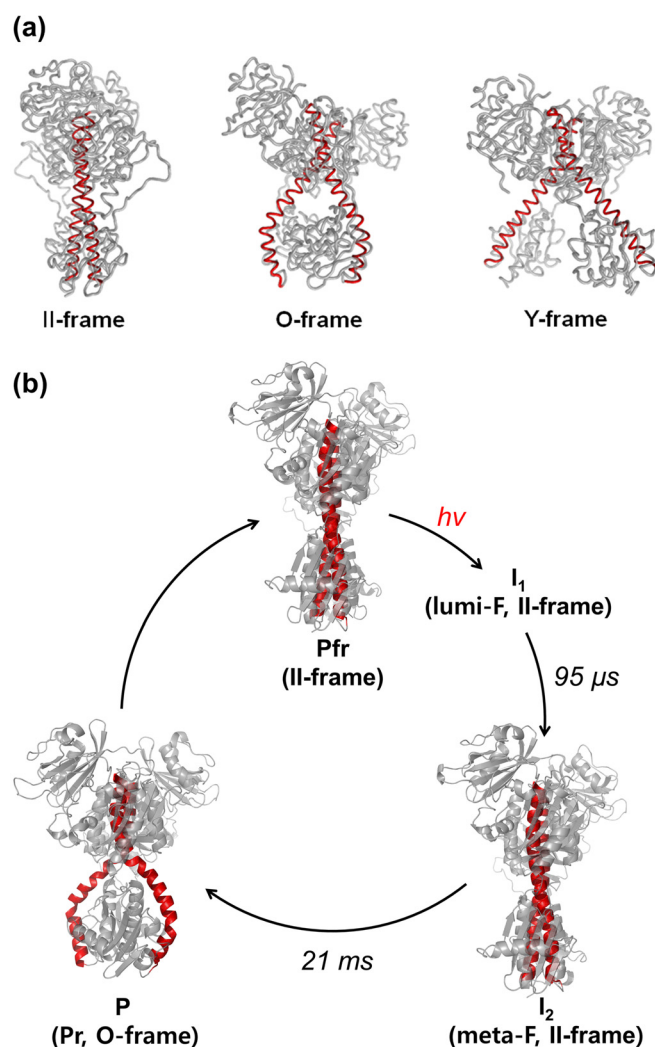


**FIG. 14.** (a) Three representative conformations (II-frame, O-frame, and Y-frame) of the photosensory domain of bacterial phytochromes categorized according to the spatial arrangement of the helical backbones (red ribbons) in reported crystal structures. (b) Schematic for the structural dynamics of the bathy bacterial phytochrome from *P. aeruginosa* upon photoexcitation revealed via TRXL. Reproduced with permission from Lee *et al.*, *Sci. Adv.* **8**, eabm6278 (2022). Copyright 2022 Authors, licensed under a Creative Commons Attribution 4.0 License.

G-protein-coupled receptor (GPCR).<sup>176,177</sup> The retinal chromophore of a retinylidene protein is covalently bound to the protein in the form of a Schiff base, and it has a C = C double bond which can isomerize upon photoexcitation. The isomerization of the retinal chromophore induces the structural change in retinylidene proteins and their functions *in vivo*. In the cases of bR and pR, the retinal chromophore transforms its conformation from the all-trans conformation to the 13-cis conformation upon photoexcitation.<sup>174,178</sup> This structural change accompanies the transportation of a proton via the protonation-deprotonation process of several residues. In the case of rhodopsin, the 11-cis conformation of the retinal chromophore becomes the all-trans

conformation upon photoexcitation, inducing the structural change in the protein and eventually the signal transduction.<sup>176,177,179</sup> Retinylidene proteins have served as model systems for photoactive proteins and been extensively investigated with time-resolved spectroscopic methods. For example, using methods such as time-resolved FTIR, the reaction intermediates involved in the photoreaction of bR were identified, and the proton pump mechanism was elucidated as well by revealing the protonation states of the chromophore and key residues.<sup>180,181</sup> Nevertheless, it remained challenging to unveil the structural dynamics of retinylidene proteins via crystallography due to the difficulty in crystallization, which is a general problem for membrane proteins. In this regard, TRXL opened a new door for investigating the structural dynamics of retinylidene proteins, which are difficult to study using crystallography.

*a. Bacteriorhodopsin and proteorhodopsin.* In a study of WT bacteriorhodopsin (bR) and proteorhodopsin (pR), structural dynamics in the time domain ranging from hundreds of nanoseconds to hundreds of milliseconds were investigated using TRXL.<sup>65</sup> The TRXL data from bR and pR are similar but show differences in detailed peak positions and amplitudes. In particular, for both cases, the difference scattering data in the WAXS region ( $0.4\text{--}0.6\text{ \AA}^{-1}$ ) in the microsecond timescale show distinct signal features attributable to helix rearrangement. The kinetic analysis suggests that three reaction intermediates (early, intermediate, and late species) are involved [Fig. 15(a)]. Although the SADSs of all three intermediates were obtained from the kinetic analysis, the SADS of the early intermediate was not used for structure refinement due to the insufficient signal-to-noise ratio. Structure refinement was performed using rigid-body modeling. In this method, the protein was divided into several rigid bodies. Then, based on the structural change in bR and pR suggested by previous studies,<sup>182,183</sup> the rigid bodies were allowed to move to imitate the protein motion that best describes the SADSs of intermediates. It should be noted that retinylidene proteins, including bR and pR, are surrounded by lipid or detergent molecules. The surrounding molecules, different from water, affect the electron density of the excluded volume and the density of the border layer, thereby changing the x-ray scattering intensity. In addition, the arrangement of the surrounding molecules can be altered upon the structural change in the protein. Accordingly, the surrounding molecules also contribute to the TRXL signal. Their simulation results showed that the contribution of the arrangement change in the surrounding molecules to the TRXL signal is not significant in the WAXS region, which was used for the structure refinement in the study of bR and pR. Accordingly, the movement of surrounding molecules due to the change in the protein structure was ignored during the structure refinement. For example, the changes in the shape and density of a micelle were not considered. Nevertheless, the x-ray scattering intensity was calculated by using a system in which the protein was inserted into a micelle to consider the presence of the micelle surrounding the protein. Based on the structure refinement, the SADSs of the intermediate and late species of bR can be described using the movements of the C, E, and F helices. Specifically, the cytoplasmic portion of the C helix moves inward, and the cytoplasmic portions of the E and F helices move outward [Fig. 15(b)]. The amplitude of protein movement increased by  $\sim 50\%$  in the late species than in the intermediate species. From previous studies, it was known that the deprotonation of the Schiff base, the

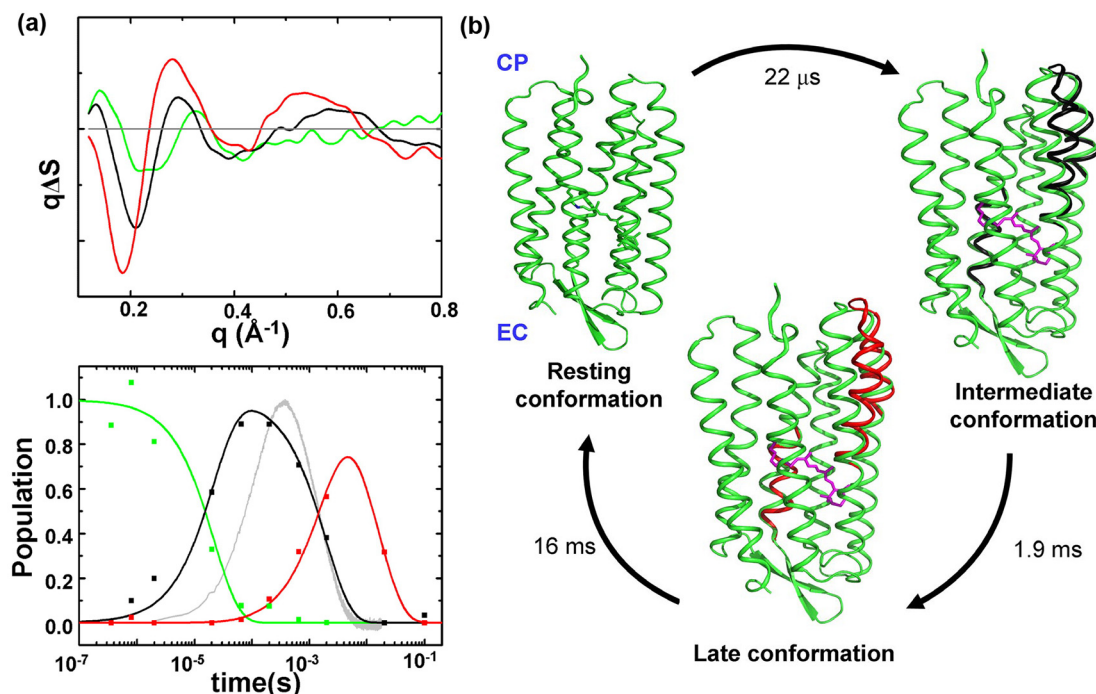


**FIG. 15.** (a) (Top) SADSs of the reaction intermediates involved in the photoreaction of bR obtained from the TRXL data. (Bottom) The corresponding time profiles of the populations. The early, intermediate, and late species are shown in green, black, and red. For the time profiles of the population, the squares in the time profiles indicate the optimal populations of the reaction intermediates at each time delay, which were obtained by fitting the TRXL data with the linear combination of the SADSs of the intermediates. The solid lines indicate the population change calculated using the kinetic model, and the solid gray line indicates the population of the deprotonated Schiff base obtained from a TA experiment. (b) Structural change in bR upon photoexcitation obtained by TRXL. The ground state (resting conformation), intermediate species (intermediate conformation), late species (late conformation), and chromophore are shown in green, black, red, and magenta, respectively. Reproduced with permission from Andersson *et al.*, *Structure* **9**, 1265 (2009). Copyright 2009 Elsevier Ltd.

chromophore, plays an important role in proton transfer.<sup>178,184</sup> The TA signal, which was measured in addition to the TRXL data, indicates that the deprotonation of the Schiff base occurs between the formation of the intermediate species and the late species [Fig. 15(a)]. A structural analysis of TRXL data showed that the intermediate and late species have the same structural motion in terms of the directions of helix movements, although the late species has a larger amplitude of motion than the intermediate species. In this regard, it was suggested that the deprotonation of the Schiff base enhances only the amplitude of the structural change without greatly altering the directions of helix movements. Meanwhile, the structural change in the protein obtained through TRXL was found to be larger than that observed in the crystalline phase. Structure refinement was performed on pR in the same manner as used for bR. Based on the result of the structure refinement, it was suggested that the capping motion of the G helix, as well as the structural change observed in bR, occurs in the late species of pR. On the other hand, for the intermediate species, it was difficult to determine the structural change due to the unsatisfactory agreement between the SADS and the theoretical difference scattering curve obtained from the structure refinement.

Afterward, the structural dynamics of pR were revisited using TRXL.<sup>185</sup> In this study, different from the previous study in which the TRXL experiment was performed only on the native form, the TRXL experiment was performed not only on native pR but also on the

protein in which one of the methyl groups of the retinal chromophore was substituted with iodine (I-pR). Since x-ray scattering is affected by the electron density of molecules, heavy-atom labeling has been proposed as a method to increase sensitivity to subtle local structural changes nearby the labeled atom. One of the problems with heavy-atom labeling is that it may change the kinetics of the structural dynamics of the molecule or even the structural change itself. In this regard, TRXL experiments on native pR and I-pR could be used to confirm the effect of heavy-atom labeling on the protein structural dynamics. Overall, I-pR shows faster kinetics compared to native pR. Both native pR and I-pR data can be explained by the formation and decay of a reaction intermediate. In native pR, the intermediate is formed with a time constant of 2  $\mu\text{s}$  and decayed with a time constant of 49 ms [Fig. 16(a)]. For I-pR, the TRXL signal has fully emerged by the fastest time delay (2  $\mu\text{s}$ ) of the experiment and decayed with a time constant of 2 ms [Fig. 16(a)]. As opposed to the differences in kinetics, the first ISVs of the TRXL data from two proteins, which can represent the SADSs of the intermediates of the two proteins, are similar [Fig. 16(a)]. The structure refinement was performed using rigid-body modeling and MD simulations. First, the structures of the ground and intermediate states that can explain the intermediate difference scattering curve well were obtained using rigid-body modeling in a similar way to that used for bR and pR. Then, MD simulations were performed using those resultant structures. The MD simulations were

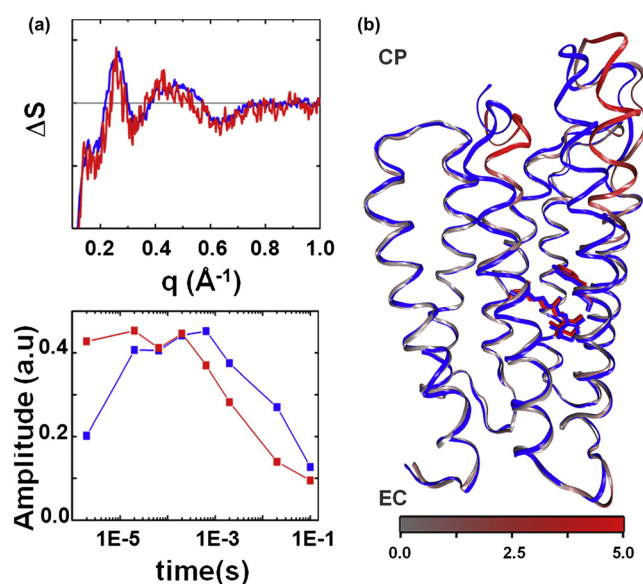


**FIG. 16.** (a) The first ISVs (top) and rSVs (bottom) of the SVD results obtained from the TRXL data from native pR (blue) and I-pR (red). (b) Structural change in pR upon photoexcitation obtained by TRXL. The structure of the ground state is shown in blue. The structure of the intermediate state is shown in a gray-to-red scale according to the amplitude of the movement. Reproduced with permission from Malmerberg *et al.*, *Biophys. J.* **101**, 1345 (2011). Copyright 2011 Biophysical Society.

performed on a system containing surrounding molecules as well as the protein, in which both the presence of the surrounding molecules and their arrangement change due to the structural change in the protein can be considered. Among the structures obtained from the MD simulations, the structure pair of the ground and intermediate states that best described the SADS was selected for further analysis [Fig. 16(b)]. The structural changes observed in the best structure pairs for native pR and I-pR were similar, indicating that the structural changes in native pR and I-pR are similar. The different kinetics of native pR and I-pR were explained by the different steric interactions around the chromophore. According to additional MD simulations for estimating the free energy differences of native pR and I-pR, heavy-atom labeling induces the larger steric interaction between the chromophore and the nearby residues and destabilizes the protein with the 13-*cis* chromophore, resulting in the acceleration of the structural change after the isomerization of the chromophore.

**b. Rhodopsin.** Rhodopsin has a different photoreaction pathway from other retinylidene proteins, such as bR and pR, in terms of the reversibility of the reaction. As opposed to bR and pR, which have reversible photocycle, the retinal chromophore of rhodopsin is eventually released from the protein via hydrolysis after isomerization.<sup>176,177,179</sup> Because of this irreversible characteristic, a fresh sample should be continuously provided during the TRXL experiment on rhodopsin, and the iterative measurement on the same sample, which is often used in TRXL experiments, cannot be easily utilized. Using a rapid readout detector can overcome such a limitation. In a typical TRXL experiment, the sample is exposed to a single x-ray probe pulse

with a specific time delay after the initiation of the reaction by a pump pulse, and the scattered x-ray pulse is collected by a detector to generate an x-ray scattering image. In other words, for each pump pulse, a single x-ray pulse is used to obtain an x-ray scattering signal. In contrast, in the experimental scheme using a rapid readout detector, a series of x-ray pulses instead of a single x-ray pulse pass through the sample after the photoexcitation by the pump pulse.<sup>186</sup> Because of the short readout time of the detector (for example, 3 ms in this case), the detector can record multiple x-ray scattering images with different time delays, each of which is from a different portion of an x-ray pulse series, while a series of x-ray pulses pass through the sample. Namely, multiple x-ray scattering images with different time delays are obtained using a single pump pulse. The sample exposed to a series of x-ray pulses is then replaced with a fresh sample. In this way, the amount of sample required for collecting x-ray scattering images with various time delays can be greatly reduced. A caveat is that such an experimental scheme using a rapid readout detector has a disadvantage in that damage due to x-rays can be accumulated because the sample is repeatedly exposed to a succession of x-ray pulses. In the TRXL experiment on rhodopsin, the TRXL data were collected on the rapid readout detector for various time delays from -200 ms to 2.8 s [Fig. 17(a)].<sup>68</sup> By analyzing the kinetics of the TRXL data, it was confirmed that a light-activated state is generated with a time constant of 13 ms from the resting state and is then maintained up to 2.8 s. Structural analysis of the light-activated state was performed in a manner similar to that used for the analysis of pR and I-pR. Considering the suggestion from previous studies using atomic force microscopy (AFM) that rhodopsin forms a dimer,<sup>187,188</sup> the structure refinement was performed on both the monomeric and dimeric forms of rhodopsin. The SADS of the light-activated state could be described slightly better when the dimeric form was used for the refinement. Regardless of the oligomeric states, the outward tilt of the cytoplasmic portion of helix 6, the inward tilt of the cytoplasmic portion of helix 5, and the outward movement of cytoplasmic loop III, connecting helix 6 and helix 5, are observed [Fig. 17(b)]. The movement of these helices is similar to that observed in previous crystallography studies. Still, the amplitude of the structural change observed in the solution is larger by 80% than that observed in the crystal, and the amplitude is similar to that of the structural change induced by the coupling of a homologous GPCR protein and a G protein. It was suggested that the movements observed by crystallography are limited due to various factors, such as crystal contacts.

### 3. Photoactive yellow protein

Photoactive yellow protein (PYP) is known to play a role in the negative phototaxis of bacteria called *Halorhodospira halophila*.<sup>189</sup> PYP has *p*-coumaric acid as the chromophore. Upon photoexcitation, trans-to-*cis* isomerization of *p*-coumaric acid occurs, accompanying the structural changes in the protein.<sup>190,191</sup> Because PYP can be readily produced and has natural photoactivity under physiological conditions, the structural dynamics of PYP have been investigated using TRXL as a model system to study the photoreceptor proteins. Even before the development of TRXL, local structural changes in PYP, including the partial unfolding of the N-terminal of PYP, had been identified via experimental tools sensitive to local structural changes, such as FTIR and CD spectroscopy.<sup>192–194</sup> TRXL revealed the global



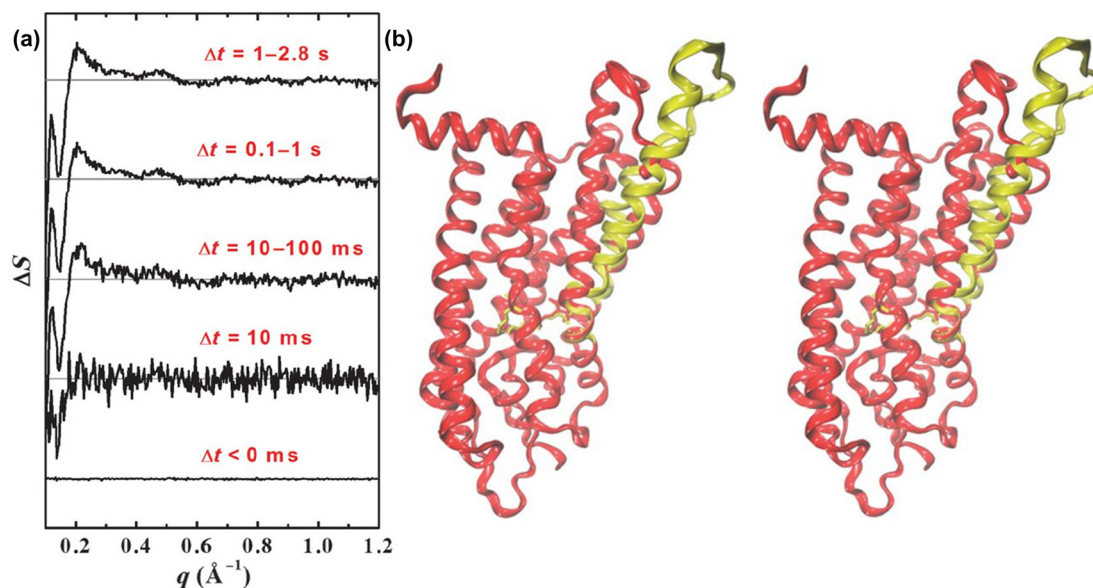


**FIG. 17.** (a) TRXL data from rhodopsin obtained using a rapid readout detector. The TRXL data at five representative time intervals (negative delays, 10 ms, from 10 to 100 ms, from 100 ms to 1 s, and from 1 to 2.8 s) are shown. (b) Stereo view representation of the structural change in rhodopsin obtained by TRXL. The resting state is shown in red, while the cytoplasmic portions of helix 5 and 6 and the loop III connecting those helices in the light-activated state are shown in yellow. Reproduced with permission from Malmerberg *et al.*, *Sci. Signaling* **8**, ra26 (2015). Copyright 2015 American Association for the Advancement of Science.

structural changes in PYP, and the results were compared with those of other studies to elucidate the relation between local and global structural changes.

The first TRXL experiment on PYP, combined with other techniques, such as nuclear magnetic resonance (NMR) spectroscopy and double electron–electron resonance (DEER) spectroscopy, was performed to unveil the structural dynamics of PYP in the solution phase.<sup>195</sup> The TRXL signal of PYP obtained at 10 ms provides information on the global structural changes in the  $pB_2$  state (the  $I_2'$  state), which corresponds to the signaling state of PYP. The TRXL signal in the SAXS region of the difference scattering curve increases, whereas the signal decreases at  $q = 0.13 \text{ \AA}^{-1}$  [Fig. 18(a)]. Based on these features, it was suggested that the  $R_g$  of the protein increases in the  $pB_2$  state. The TRXL data, together with the results obtained by other experimental methods, were used for the structure refinement [Fig. 18(a)]. According to the refinement results, the N-terminal region loses its  $\alpha$ -helical content in the  $pB_2$  state [Fig. 18(b)]. In addition,  $pB_2$  has a structure in which the N-terminal region and the chromophore binding cleft are closely located.

In a subsequent TRXL study, the structural dynamics of PYP over a long time range (3.16  $\mu\text{s}$  to 300 ms) rather than a single time point were clarified.<sup>67</sup> The kinetic analysis uncovered that four reaction intermediates ( $pR_1$ ,  $pR_2$ ,  $pB_1$ , and  $pB_2$ ) are involved in the photo-reaction [Fig. 19(a)]. To elucidate the structures of the intermediates, low-resolution structure reconstruction was performed on the SACs of the intermediates. The SACs were generated by adding a properly scaled static x-ray scattering curve of the ground state ( $pG$ ) to the SADS obtained from the kinetic analysis. From the low-resolution structure reconstruction results, it was confirmed that a protrusion occurs upon photoactivation [Fig. 19(a)]. The protrusion gradually

increases as time passes, increasing the  $R_g$  of the protein. Based on the previous TRXL study, it was suggested that protrusion is due to the motion of the N-terminal region. Concerning the kinetics, it was proposed that a parallel model in which both  $pR_1$  and  $pR_2$  are generated from  $pG$  in a parallel manner is more suitable than a sequential model in which  $pR_1$  and  $pR_2$  are sequentially generated from  $pG$  [Fig. 19(a)]. Then,  $pR_1$  and  $pR_2$  are transformed into  $pB_1$  and  $pB_2$  in a sequential manner. Meanwhile, the structural change in PYP observed in the solution phase is similar to that observed in the crystalline phase,<sup>56</sup> but the structural change is much larger in the solution phase. This result showcases that the movement of the protein within the crystal is restricted by the crystal contact.

Afterward, another TRXL study on PYP, covering a longer time range (100 ps to 1 s) than the previous study, was conducted.<sup>196</sup> It was suggested that four intermediates are involved in the structural dynamics of PYP, as reported in the previous TRXL study. According to their analysis, an increase in the  $R_g$  of PYP was observed in the signaling state, but the degree of the increase in the  $R_g$  revealed in this study (1.9  $\text{\AA}$ ) was larger than that of the previous study (0.9  $\text{\AA}$ ). The reconstructed low-resolution structure of the signaling state exhibits protein elongation, and it was suggested that the unfolding of the residues in the N-terminal region is responsible for the elongation.

In addition to the TRXL study on WT PYP, a mutant study was performed to clarify the role of a key residue, Glu46.<sup>197</sup> The Glu46 residue is located near the chromophore of PYP and forms a hydrogen bond with the chromophore. Upon photoactivation, Glu46 transfers a proton to the chromophore,<sup>198,199</sup> and such a transfer is known to be involved in the generation of the  $pB$  state, the signaling state. In E46Q PYP, proton transfer by Glu46 cannot occur since the Glu46 residue is mutated into Gln. To investigate the effect of proton transfer from

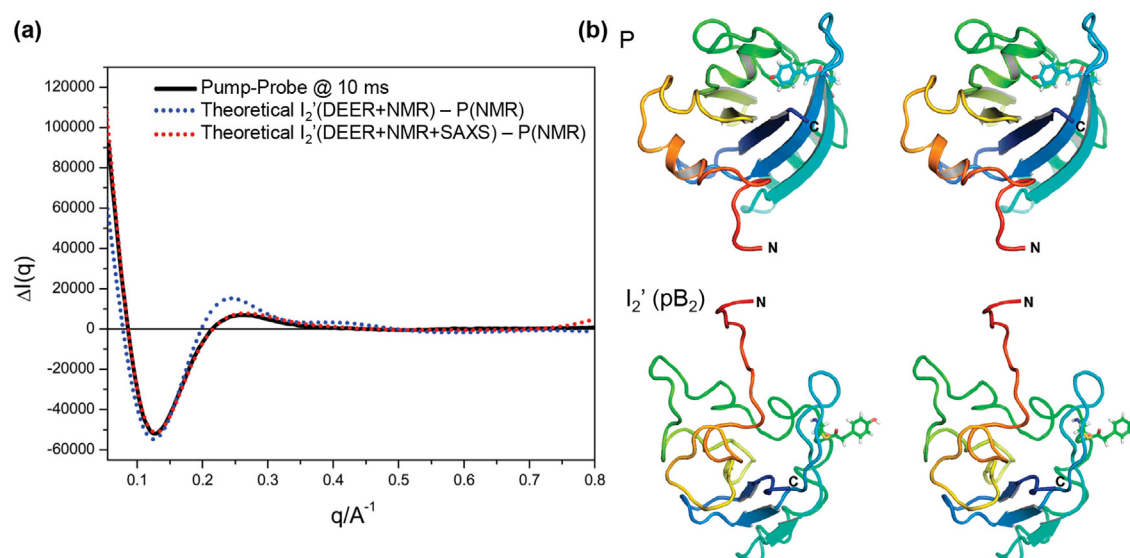


**FIG. 18.** (a) Comparison of the experimental difference scattering curve of PYP at 10 ms (black) obtained from a TRXL experiment and theoretical difference scattering curves (blue and red). The theoretical difference scattering curve obtained from a structural change refined using DEER and NMR is shown in blue, and that in which DEER, NMR, and TRXL were used for the refinement is shown in red. (b) Stereo view representation of the structures for the ground state (top) and the pB<sub>2</sub> state (the I<sub>2</sub>' state) (bottom). The structure of the ground state was obtained using DEER and NMR, and the structure of the pB<sub>2</sub> state was obtained using DEER, NMR, and TRXL. Adapted with permission from Ramachandran *et al.*, *J. Am. Chem. Soc.* **133**, 9395 (2011). Copyright 2011 American Chemical Society.

Glu46 on the structural dynamics of PYP, a study on the E46Q mutant, which combined TRXL and TA, was performed over a time range from a microsecond to a hundred milliseconds. The TA result confirmed that a state whose absorption is red-shifted compared to the ground state is formed upon photoexcitation. Then, the transition to a different state whose absorption is blue-shifted occurs with a time constant of 64  $\mu$ s. The kinetic analysis of the TRXL data from the E64Q mutant established a kinetic model in which four intermediates evolve and decay sequentially. The time for the second-to-third intermediate transition is 143  $\mu$ s, similar to that of the 64  $\mu$ s observed in the TA experiment. Accordingly, the first and second intermediates were assigned to pR <sub>$\alpha$</sub>  and pR <sub>$\beta$</sub> , respectively, and the third and fourth intermediates were assigned to pB <sub>$\alpha$</sub>  and pB <sub>$\beta$</sub> , respectively [Fig. 19(b)]. The larger time constant obtained from TRXL (143  $\mu$ s) compared to that obtained from TA (64  $\mu$ s) suggested that the propagation of the structural change from the chromophore to the whole protein takes time. Similar to the study on WT, SACs were generated for the reaction intermediates. The SACs of pR <sub>$\alpha$</sub>  and pR <sub>$\beta$</sub>  are similar to each other, and those of pB <sub>$\alpha$</sub>  and pB <sub>$\beta$</sub>  are also similar. These results indicate that a relatively large structural change is accompanied by the pR <sub>$\beta$</sub> -to-pB <sub>$\alpha$</sub>  transition, but the structural changes are not significant for the rest of the transitions, such as the transition from pR <sub>$\alpha$</sub>  to pR <sub>$\beta$</sub> . According to the result of low-resolution structure reconstruction using SACs, the structural change observed in pB <sub>$\alpha$</sub>  is similar to that observed in the pB<sub>2</sub> of WT. Based on this, the pB <sub>$\alpha$</sub>  state was assigned to the signaling state [Fig. 19(b)]. The amplitude of the structural change occurring in pB <sub>$\alpha$</sub>  was smaller than that of the pB<sub>2</sub> state of WT. It was suggested that the smaller structural change in E46Q is caused by a smaller structural perturbation in the N-terminal region due to the decrease in the hydrogen bond strength between the chromophore and the 46th residue and the absence of proton transfer.

Using the characteristics of PYP, that a structural change readily occurs upon photoactivation and that the structural change had been well-elucidated, a molecular switch composed of PYP was developed and characterized using TRXL.<sup>200</sup> In this molecular switch, four PYP monomers were connected in a circular form to create a circular oligomer PYP (coPYP) that can change the overall size of a protein upon photoactivation. The electronic state dynamics and structural dynamics of this molecular switch were explored using TA and TRXL. The TA data confirmed that the electronic state dynamics of monomeric PYP and coPYP have similar time constants, and various intermediates identified in the TRXL experiment were assigned following the TA results. The kinetic analysis of the TRXL data indicated that three intermediates (I<sub>1</sub>, I<sub>2</sub>, and P) contribute to the TRXL signal in the time domain from 3.16  $\mu$ s to 178 ms. Through a comparison with the time constants obtained from TA, I<sub>1</sub>, I<sub>2</sub>, and P were assigned to the pR<sub>2</sub>, pB<sub>1</sub>, and pB<sub>2</sub> states, respectively. Structure refinement was performed using MD simulations and the ensemble optimization method (EOM). Structure pools of the ground and intermediate states were generated using MD simulations. Afterward, using the structures in the structure pools, structure ensembles were generated through the EOM so that the ensembles could describe the SACs of the ground and three intermediate states well. According to the refinement result, the R<sub>g</sub> of the structure ensemble for coPYP in the ground state has a major peak at 32 Å [Figs. 20(a) and 20(b)]. In I<sub>1</sub> and I<sub>2</sub>, the global structural changes are not large, and only the distributions of the major peaks are broadened. This result indicates that, in I<sub>1</sub> and I<sub>2</sub>, a local structural change occurs and that the protein becomes flexible. In the refinement results of the P state, not only is the distribution of the major peak broadened, but a new peak emerges at 28.5 Å, which means that protein contraction occurs [Figs. 20(c)–20(e)]. The protein contraction of coPYP is contradictory to the expectation that protein



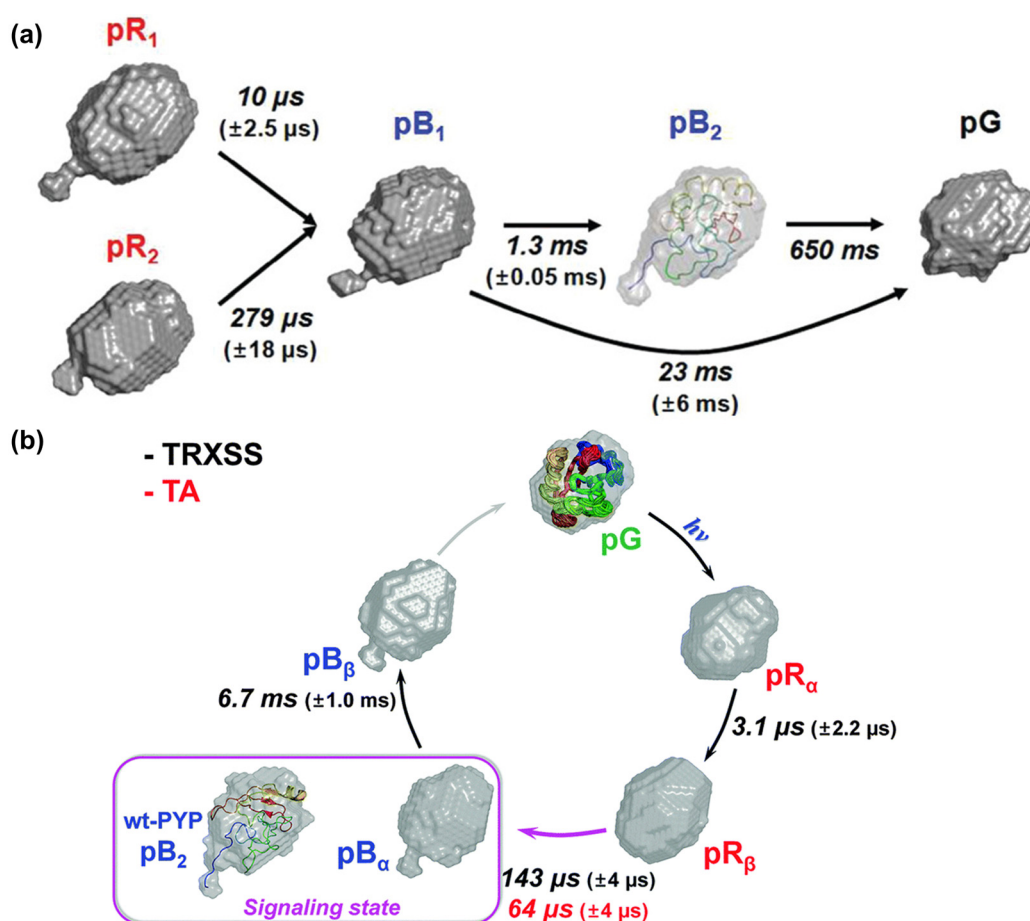


**FIG. 19.** (a) Reconstructed molecular shapes of the reaction intermediates and ground state of WT PYP obtained using TRXL. The time constants for the transition between reaction intermediate and ground state recovery are shown. The reconstructed molecular shape of  $pB_2$  is superimposed on a reported protein structure obtained from a study that used NMR, DEER, and TRXL.<sup>195</sup> Reproduced with permission from Kim *et al.*, J. Am. Chem. Soc. **134**, 3145 (2012). Copyright 2012 American Chemical Society. (b) Reconstructed molecular shapes of the reaction intermediates and ground state of the E46Q mutant of PYP obtained using TRXL. In the magenta box, the molecular shape of the signaling state of WT is also shown for comparison. The time constants for the transitions obtained from TA and TRXL are shown in red and black, respectively. Reproduced with permission from Kim *et al.*, Phys. Chem. Chem. Phys. **18**, 8911 (2016). Copyright 2016 the PCCP Owner Societies.

expansion would occur upon photoactivation through the N-terminal protrusion motion of monomeric PYP. It was suggested that such an unexpected protein contraction originates from the flexibility of coPYP, allowing coPYP to form new interactions among the constituent monomeric PYPs.

#### 4. Light-oxygen-voltage domain

A light-oxygen-voltage (LOV) domain participates in the regulation of several protein functions via structural changes in response to various stimuli, such as light, oxygen, and voltage. A LOV domain has a flavin mononucleotide as a chromophore. When the chromophore is excited by blue light, a triplet excited state is formed via intersystem crossing from the singlet excited state [Fig. 21(a)].<sup>201–203</sup> Eventually, a covalent bond between the chromophore and a nearby Cys residue is formed,<sup>203,204</sup> accompanying the structural change in the LOV domain. The structural change in a LOV domain plays a role in

regulating the function of a protein<sup>205,206</sup> by inducing the association or dissociation of the protein or the structural change in the overall protein. The global structural changes in LOV domains and the subsequent structural changes of other motifs were investigated using TRXL.

*a. Light-oxygen-voltage domain from Bacillus subtilis YtvA.* In the case of the bacterial LOV domain from *Bacillus subtilis* YtvA (*BsYtvA*),<sup>206</sup> the LOV domains form a dimer via the A'α helices and are connected to other motifs of the protein through the Jα helices. Using the photoresponsive properties of the LOV domains, a chimeric protein (YF1) where a histidine kinase and the LOV domains from *BsYtvA* are fused together was prepared. TRXL experiments were performed on the LOV domains<sup>69</sup> and full-length protein<sup>207</sup> of this chimeric protein to elucidate their structural dynamics. The TRXL signal of the LOV domains emerged with a time constant of  $\sim 2 \mu s$ , which is in agreement with the time for the formation of the chromophore–

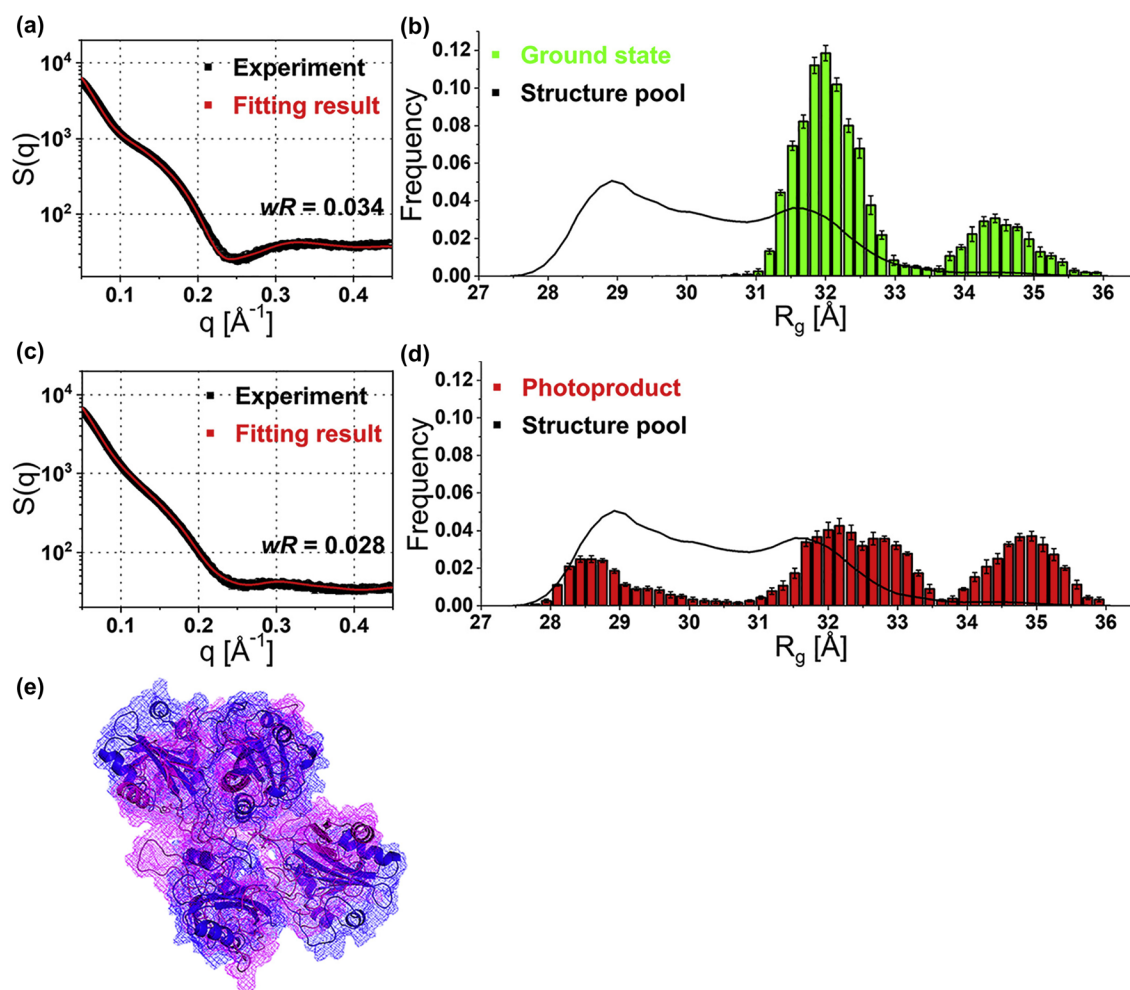


**FIG. 20.** Results from structure refinement of the ground state and the P state using MD simulations and the EOM on the x-ray scattering data from coPYP. (a) Experimental static curve (black) for the ground state and the fitted static curve (red) of the ensemble obtained from the analysis of the x-ray scattering data. The weighted R factor ( $wR$ ) indicates the discrepancy between the experimental and fitted static curves. (c) The counterpart of (a) for the P state. (b) and (d) The distributions of  $R_g$  in (b) the ground state and (d) the P state determined by an EOM analysis. (e) Overlay of the ground state (blue) and P (magenta) states of coPYP composed of four monomeric PYPs. Reproduced with permission from Lee *et al.*, Cell Rep. Phys. Sci. 2, 100512 (2021). Copyright 2021 Elsevier.

cysteine adduct observed in a spectroscopic study [Fig. 21(b)].<sup>208</sup> After that, there is no significant change in the signal until the millisecond timescale. Based on this result, it was suggested that the signaling state is formed with a time constant of  $\sim 2 \mu\text{s}$ . A Fourier transform was performed on the TRXL data to elucidate the approximate structural change, and the pair distribution function at the large distance was positive, indicating that protein expansion occurs upon photoactivation [Fig. 21(b)]. Detailed structural changes were revealed through structure refinement using MD simulations. In this method, two MD simulations were performed using the crystal structure of YF1 under two different force fields. One force field was that of the dark state (the ground state) to describe the protein structures in the dark state. The other was the force field for the adduct state, where the chromophore forms a covalent bond with a Cys residue to describe the protein structure in the signaling state. Then, among the structures obtained from

the MD simulations, structure pairs that can describe the TRXL data well were selected for structural characterization. The result of the structure refinement indicated that the distance between the two monomeric LOV domains increases upon photoexcitation [Fig. 21(a)]. The increase in the distance between the monomers is the greatest in the C-terminal region where the  $J\alpha$  helix is attached and the smallest in the N-terminal region. The observed structural change is similar to the structural changes found in the crystalline phase, but the amplitude of the change is larger than that in the crystalline phase.

Such a structural change in the LOV domains is transferred to other motifs of the protein, resulting in structural changes in other motifs. The structural change in the overall protein induced by the LOV domains was investigated in a TRXL study, which used TA as well, on full-length YF1. Two reaction intermediates were identified from the kinetic analysis of the TRXL data. The first intermediate

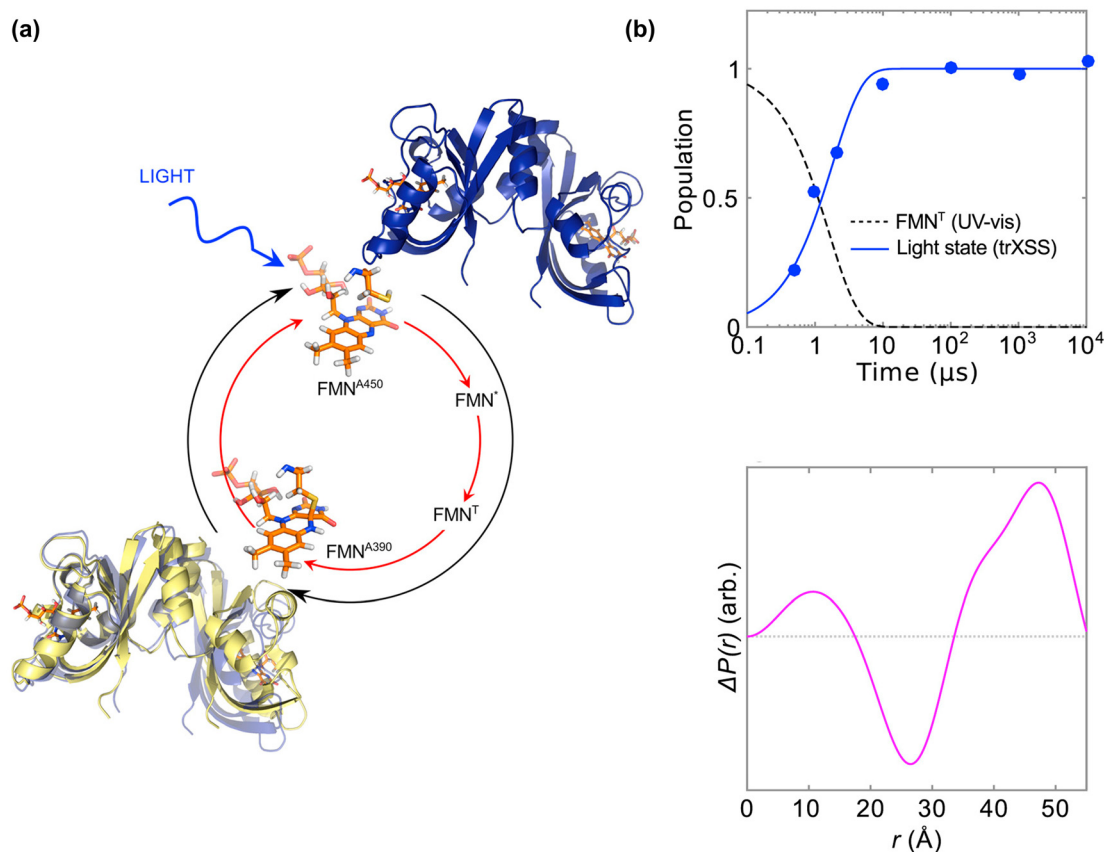


**FIG. 21.** (a) Schematic for the change in the chromophore and the LOV domains upon photoexcitation. The structures of the ground and signaling states are represented by blue and yellow ribbons, respectively. The chromophores of the LOV domains, shown in the red inner circle and protein structures, are shown with stick representation. (b) (Top) Time profile for the population of the signaling state (blue) obtained from the kinetic analysis of the TRXL data from the LOV domains and the time profile for the decay of the chromophore in the triplet state (dashed line) from a TA study. (Bottom) Change in the pair distribution function obtained using the TRXL data at  $>100$  ms. Reproduced with permission from Bertsson *et al.*, *Structure* **25**, 933 (2017). Copyright 2017 Elsevier.

(YF1<sub>int.</sub>) is formed with a time constant of 2  $\mu$ s and transforms into the second intermediate (YF1<sub>fin.</sub>) with a time constant of 250 ms. The time constant for the formation of YF1<sub>int.</sub> is similar to the decay time of the triplet state of the chromophore, which was obtained from the TA experiment, indicating that the formation of YF1<sub>int.</sub> accompanies the adduct formation. The structural changes occurring at each intermediate were elucidated via structure refinement using MD simulations, similar to that used for the LOV domains. The formation of YF1<sub>int.</sub> accompanies the structural change in the LOV domains, the left-handed supercoiling of the J $\alpha$  helices, and the left-handed rotation of the kinase motif (Fig. 22). Based on these results, it was concluded that the structural change in the LOV domains causes left-handed supercoiling of the J $\alpha$  helices. In the structure refinement results of YF1<sub>fin.</sub>, the movements of the catalytic and ATP-binding (CA) domains of the kinase motif were observed (Fig. 22). It was suggested that the concept of structural change transfer from the LOV domains to other motifs can reflect the reaction pathways of other signal receptor proteins.

*b. Light-oxygen-voltage domain from green algae Chlamydomonas reinhardtii.* In addition to the LOV domains from BsYtvA, the

structural dynamics of the LOV domain from the phototropin of green algae *Chlamydomonas reinhardtii* (CrPhot)<sup>209,210</sup> were also explored using TRXL.<sup>211</sup> CrPhot has two LOV domains, LOV1 and LOV2 [Fig. 23(a)]. LOV2 is known to be related to the activity control of a kinase motif.<sup>212</sup> On the other hand, it had been suggested that LOV1 is related to the dimerization of the protein or the lifetime of the signaling state, but the role of LOV1 had not been clear.<sup>213,214</sup> Using TRXL, the structural dynamics of LOV1 were unveiled, and the interaction between LOV1 and LOV2 was suggested based on the analysis results. The TRXL data from CrPhot indicated that the structural dynamics of the microsecond time regime can be described by a kinetic model with an intermediate state (the product state), which is formed monoexponentially. The product state is formed with a time constant of 0.99  $\mu$ s. The structural change upon photoexcitation was elucidated using MD simulations, as in the case of other proteins related to the LOV domains. The structure refinement showed that CrPhot has a structural change similar to that of the LOV domains from BsYtvA, although the biological roles of LOV1 from CrPhot and the LOV domains from BsYtvA are different [Fig. 23(b)]. In addition, the results indicated that changes in the hydrogen bond and salt bridge

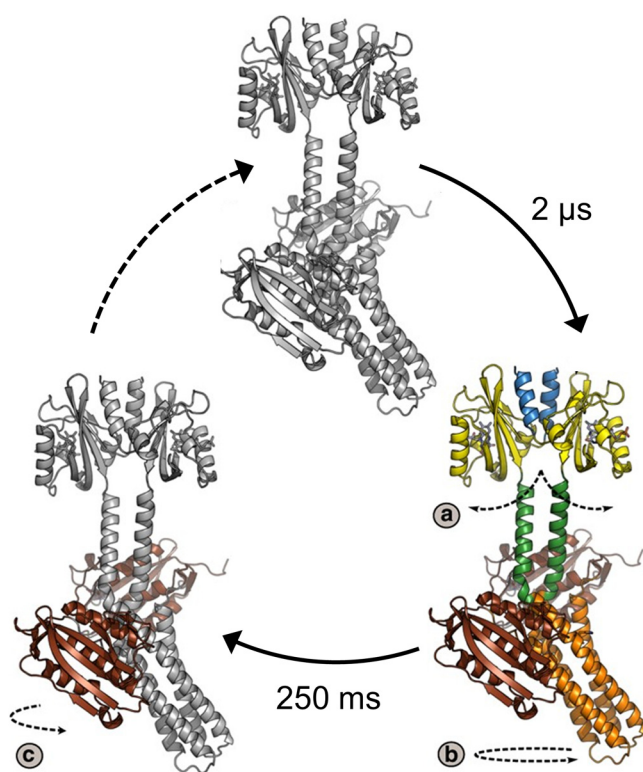


**FIG. 22.** Schematic for the structural change in full-length YF1 revealed by TRXL. Upon photoexcitation, the structural change in the LOV domains (arrow a), the supercoiling of the  $J\alpha$  helices, and the rotation of the kinase motif (arrow b) occur, followed by the movement of the catalytic and ATP-binding (CA) domains of the kinase motif (arrow c). Overall protein structure is shown in gray, whereas regions with significant movements during transitions are marked in different colors. The LOV domains, the dimerization and histidine phosphotransfer (DHp) domains, and the CA domains are shown in yellow, orange, and brown, respectively. The DHp domains and the CA domains constitute the kinase motif. The  $A'\alpha$  and  $J\alpha$  helices are shown in blue and green, respectively. Adapted with permission from Berntsson *et al.*, Nat. Commun. 8, 284 (2017). Copyright 2017 Authors, licensed under a Creative Commons Attribution (CC BY) License.

in the protein occur during the structural change. For example, a hydrogen bond between Gln120 and Asn99 is observed in the dark state, whereas that between Gln120 and Thr21 is identified in the product state. The salt bridge between Asp122 and Arg91, which is absent in the dark state, is observed in the product state. It was suggested that the change in the surface charge of LOV1 due to the change in the salt bridge may affect LOV2, inducing the changes in the lifetime of the signaling state.

### 5. Other examples

*a. Cryptochrome from Drosophila melanogaster.* Cryptochromes are photoreceptors participating in the circadian clock and magnetoreception.<sup>215–217</sup> Cryptochromes have flavin adenine dinucleotide (FAD) as a chromophore [Fig. 24(a)]. When FAD is photoexcited, electron transfer occurs, forming a radical pair with residues around FAD [Fig. 24(b)].<sup>218</sup> After the deprotonation of the residues, the

recombination of radical pairs occurs on a millisecond timescale. TRXL revealed the structural dynamics of a cryptochrome accompanied by the redox reaction of the chromophore.<sup>219</sup> The cryptochrome to which TRXL was applied was that from *D. melanogaster* (*DmCry*). *DmCry* plays a role in regulating the interaction between proteins called Timeless (TIM) and E3-ubiquitin ligase Jetlag (JET).<sup>220–222</sup> An important moiety for controlling this protein–protein interaction is the C-terminal tail (CTT) in the C-terminal of *DmCry*, which blocks the interaction surface in the dark state. In addition, His378 had been suggested to play an important role. It was proposed that the hydrogen bond network changes when the protonation of His378 occurs, which induces the detachment of the CTT.<sup>223</sup> With these aspects taken into account, TRXL experiments were performed on not only WT *DmCry* but also the H378A *DmCry* mutant. In addition, for a comparative study, a TRXL experiment was performed on photolyase from *Xenopus laevis* (Pho), which has a homologous structure to *DmCry* but does not have the CTT. From the kinetic analysis of the TRXL data from *DmCry* in a time range from 10 ns to 10 ms, five intermediates (*DmCry*<sub>α</sub>, *DmCry*<sub>β</sub>, *DmCry*<sub>γ</sub>, *DmCry*<sub>δ</sub>, and *DmCry*<sub>ε</sub>), which evolve and decay sequentially, were identified [Fig. 24(b)]. The SADS of *DmCry*<sub>δ</sub> and *DmCry*<sub>ε</sub> have distinct signals in the high- $q$  region [ $q = 1$  ( $\text{\AA}^{-1}$ )], whereas the SADS of other intermediates only have distinct signals in the SAXS region. Considering the reciprocal relation of the  $q$  space and real space, it was suggested that the signal in the high- $q$  region originates from a structural change corresponding to a distance of approximately 6 Å. Based on this result, this signal was assigned to the structural change in the  $\alpha$  helix of the CTT. The TRXL signal of Pho, which does not have the CTT, is similar to the SADS of *DmCry*<sub>β</sub>, and the distinct signal in the high- $q$  region was not observed. Considering that the SADSs of *DmCry*<sub>δ</sub> and *DmCry*<sub>ε</sub> have distinct high- $q$  signals, the absence of distinct high- $q$  signals in the TRXL data from Pho indicates that the structural change in the CTT is involved in the formation of *DmCry*<sub>δ</sub> and *DmCry*<sub>ε</sub>. *DmCry*<sub>ε</sub> was assigned to a signaling state because its signal was similar to the difference between the light state and the dark state obtained from a static x-ray scattering experiment [Fig. 24(c)]. The difference pair distance distribution curve obtained from the SADS indicated that protein expansion occurs in *DmCry*<sub>ε</sub>, suggesting that the extended structure is formed due to the detachment of the CTT. Through a comparison with the structural dynamics of the H378A mutant, it was unveiled that the signaling state formation is not due to the change in His378. The H378A mutant has a kinetic framework similar to that of WT *DmCry*, and the TRXL data from the H378A mutant also have similar features to those of WT. These results imply that the His378 residue is not an exclusive factor inducing structural changes necessary for the formation of the signaling state. According to the MD simulation results, His378 stabilizes the protein in the dark state rather than affecting the structural change in the protein. In addition, it was suggested that the signal relay from the chromophore to the CTT occurs via a Coulombic interaction between the reduced chromophore and residues in the CTT rather than His378.

*b. The photosynthetic reaction center.* The photosynthetic reaction center (RC) participates in photosynthesis, and it is one of the first proteins studied using fs-TRXL with the development of XFELs. When the RC is exposed to strong light, it is necessary to rapidly release excessive energy so that such light does not damage the



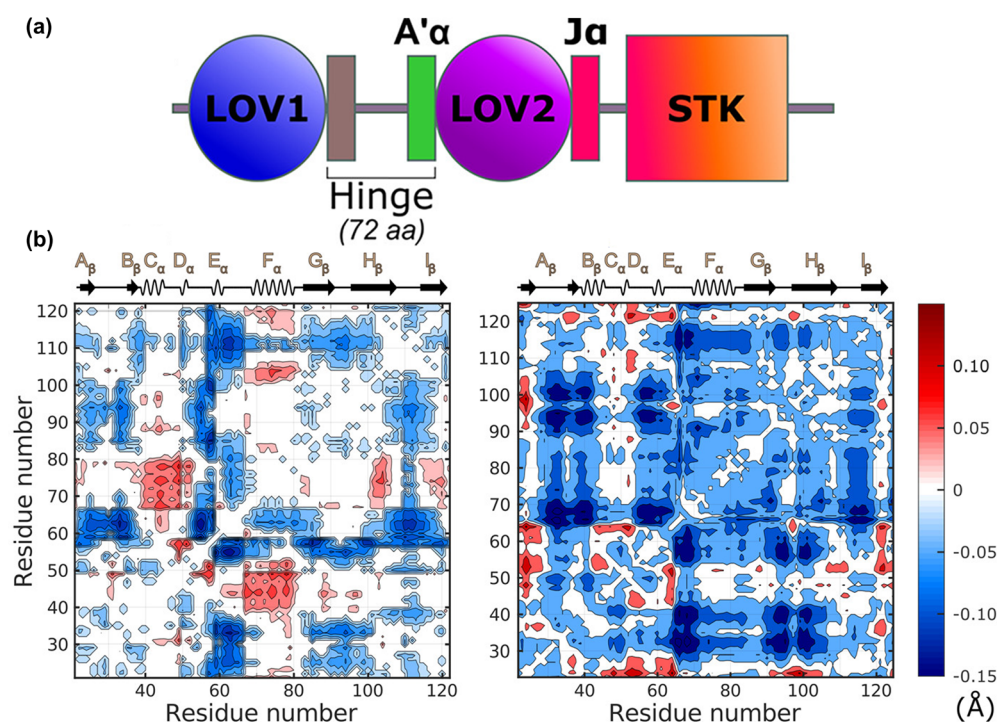


**FIG. 23.** (a) Schematic for the structure of CrPhot. It has two LOV domains (LOV1 and LOV2 domains) and a serine/threonine kinase (STK) effector domain. (b) Difference distance maps of (left) the LOV1 domain of CrPhot and (right) the LOV domains from BsYtvA. The difference distance maps were calculated using the ground state structures and the refined structures obtained from the structure refinement using the TRXL data. Reproduced with permission from Berntsson *et al.*, *Biochemistry* **59**, 3206 (2020). Copyright 2020 American Chemical Society.

integrity of the protein. To investigate such ultrafast dynamics, fs-TRXL at an XFEL, which can provide a femtosecond time resolution, was performed on the RC.<sup>224</sup> As a result, the heat transfer dynamics and protein structural dynamics involved in excessive energy dissipation were revealed using fs-TRXL. In this study, the fs-TRXL experiment was conducted under a high-laser-fluence condition where an RC molecule would absorb  $\sim 800$  photons, which can generate excessive energy. The TRXL data from 0.5 ps to 280 ps can be described using a kinetic model with four components (C1, C2, C3, and C4). The first two components (C1 and C2) are assigned to the structural change in the chromophore and protein, respectively, and the last two components (C3 and C4) are related to the heat propagation rather than the structural change in the protein. The structure refinement of C1 and C2 was performed using MD simulations. For C1, the results of the MD simulations where only the movement of the cofactors was considered can describe the experimental curve well. On the other hand, the movement of the entire protein was allowed in the MD simulations for C2. The structure refinement results of C2 indicate that the expansion of the transmembrane domain is involved in the formation of C2. In addition to the structure refinement of C1 and C2, the MD simulation results were used to assign C3 and C4. According to the MD simulation results, the time profile of heat propagation through the protein is similar to that of C3, and that of heat propagation into the surroundings is similar to that of C4. Based on these similarities, it was suggested that C3 and C4 correspond to the heat flow through the protein and that from the protein to the surroundings,

respectively. In terms of kinetics, protein structural changes (C1 and C2) precede heat transfer processes (C3 and C4). Based on this result, it was proposed that the photoexcitation of the RC accompanies the protein quake, which is the propagation of structural changes through a protein in a similar manner to wave propagation, and that the protein quake facilitates the rapid dissipation of the excessive energy generated by the photoexcitation. The results of the TRXL study on the RC promoted a question concerning biological relevance. It was suggested that the structural change observed under the extreme experimental condition (absorption of  $\sim 800$  photons per protein molecule) may not represent the actual structural change in the protein related to its biological function. In this sense, it is highly desirable to use a fluence as low as possible, ideally to the level of not compromising the biological relevance. However, if the experiment is performed with a low laser fluence, it is difficult to obtain satisfactory TRXL data in a beamtime. For this practical reason, high laser fluences, although not as strong as that used for the TRXL study on the RC, are frequently used for TRXL experiments to obtain stronger TRXL signals and, eventually, better TRXL data. XFELs with higher repetition rates can potentially make it possible to collect TRXL data with satisfactory signal-to-noise ratios even with low laser fluences. Recently developed EuXFEL or LCLS-II-HE under development provides a repetition rate of  $\sim 1$  MHz or more, which is more than  $\sim 10\,000$  times that of typical XFEL facilities. The high repetition rates of these facilities can greatly reduce the time necessary to accumulate sufficient data as far as the repetition rates of the optical lasers can match those of the XFELs.

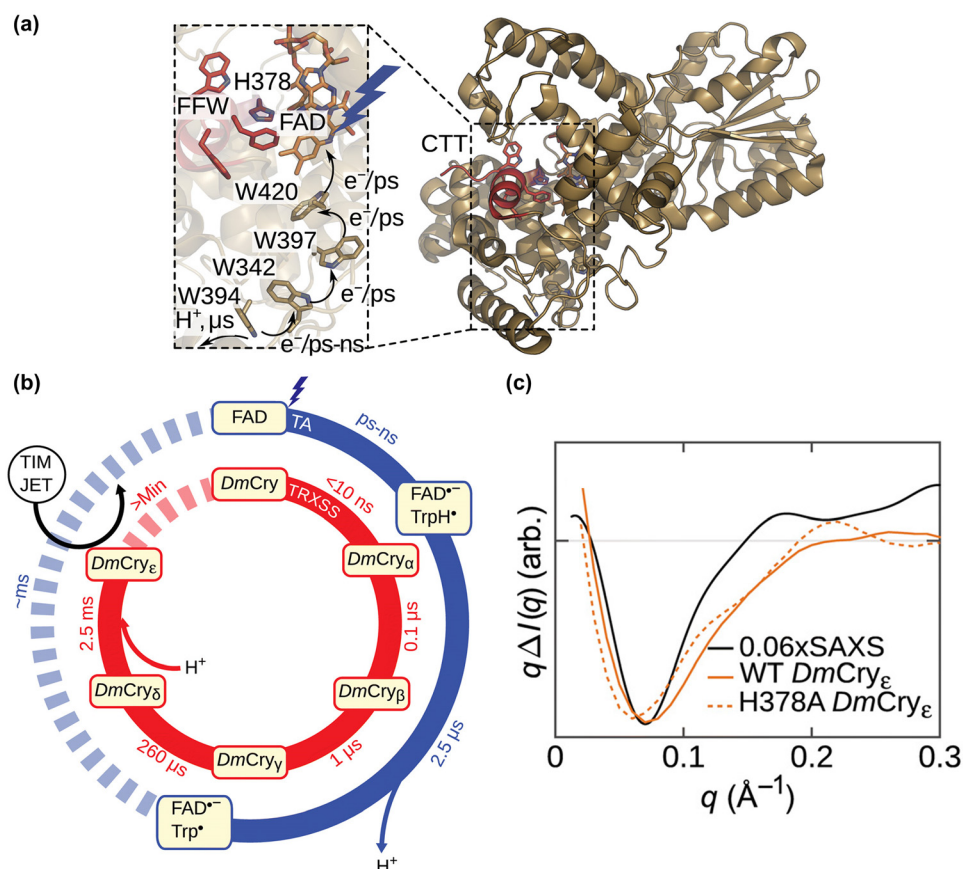


**FIG. 24.** (a) Molecular structure of *DmCry*. The inset shows the structure near the FAD chromophore. (b) Reaction schematics for the chromophore determined by TA (outer blue circle) and the overall protein revealed by TRXL (inner red circle). (c) Comparison between the experimental difference scattering curve upon photoexcitation obtained from a static x-ray scattering experiment (black solid line) and the SADSS of *DmCry*<sub>ε</sub> of WT (orange solid line) and H378A mutant (orange dashed line). Reproduced with permission from Bernthsson *et al.*, *Sci. Adv.* **5**, eaaw1531 (2019). Copyright 2019 Authors, licensed under a Creative Commons Attribution 4.0 License.

With this advantage, it will be feasible to perform laser fluence titration to find the effect of laser fluence on the structural dynamics of a protein, select an optimal laser fluence, and acquire high-quality TRXL data even under low-laser-fluence conditions.

## V. TRXL STUDIES USING OTHER PUMP METHODS

### A. Insulin (T-jump)

Insulin is a protein hormone that plays roles in important biological functions, such as regulating blood sugar. Before activation, insulin forms a hexamer, which has good long-term stability *in vivo*, and the hexamer becomes monomers upon activation.<sup>225,226</sup> In addition to the monomer and hexamer, insulin can form a dimer,<sup>227,228</sup> which is the constituent unit for the hexamer.<sup>225</sup> Because insulin can exist in various forms through interactions between proteins, it can be a model system for studying protein association dynamics due to interprotein interactions. As the oligomeric form of insulin can be controlled via temperature, T-jump TRXL was performed on insulin to understand the structural dynamics of the protein oligomer formation mechanism.<sup>229,230</sup> In particular, based on the fact that TRXL is sensitive to global structural changes, the global structural change in insulin has

been intensively investigated. In the T-jump TRXL experiment, the overtone of the O-H stretch mode of the water solvent was excited by an IR laser pulse with a wavelength of  $\sim 1.4 \mu\text{m}$  and a temporal width of  $\sim 7 \text{ ns}$ . The estimated temperature increase due to IR irradiation was about  $8^\circ\text{C}$ .

### 1. Insulin dimer

The insulin dimer is the smallest form of an oligomer, and in particular, the insulin hexamer exists as a trimer of the dimers. In this sense, the reaction dynamics of an insulin dimer may be relevant to the structural dynamics of larger oligomers. Insulin dimers can be formed by changing the solution composition and temperature. For example, a static x-ray scattering experiment on insulin in a solution of water and ethanol indicated that insulin has a dimeric form at low temperatures and a monomeric form at relatively high temperatures. In addition, temperature-dependent (T-dependent) CD spectra showed that the signal of the intermolecular  $\beta$  sheet disappears when the temperature is increased, suggesting that the dimer-to-monomer transition occurs at high temperatures. Based on these results, the experimental conditions were set (for example, an initial temperature of  $35^\circ\text{C}$ )

such that the T-jump TRXL data could reflect the structural dynamics of the dimer-to-monomer transition. The T-jump TRXL data ranging from  $\sim 10$  ns to  $\sim 100$  ms indicated that five reaction intermediates are involved in the reaction dynamics [Fig. 25(a)].<sup>229</sup> Before several hundred microseconds, three reaction intermediates ( $D^*$ ,  $D_1$ , and  $D_2$ ) are identified. Their SADSs show clear signals in the SAXS region, but they are nearly featureless in the WAXS region. Based on this result, it was suggested that no loss of the intermolecular  $\beta$  sheet occurs in these intermediates [Fig. 25(b)]. Instead, these intermediates accompany structural changes such as protein expansion ( $D^*$ ), solvent uptake ( $D_1$ ), and the internal rearrangement of the monomers ( $D_2$ ). The fourth

intermediate (2M), formed  $240 \mu\text{s}$  after the T-jump, has prominent signals not only in the SAXS region but also in the WAXS region, indicating that the dimer-to-monomer transition occurs through the loss of the intermolecular  $\beta$  sheet. The SADS of 2M is similar to the difference scattering curve for the transition from a dimer to monomers obtained in the T-dependent static x-ray scattering experiment. In addition, the SADS agrees with the theoretical difference scattering curve corresponding to the structural change for the dimer-to-monomer transition calculated using the crystal structures. Therefore, 2M was assigned to the dissociated insulin monomers [Fig. 25(b)]. The SADS of the final reaction intermediate ( $2M'$ ), which is formed on a millisecond

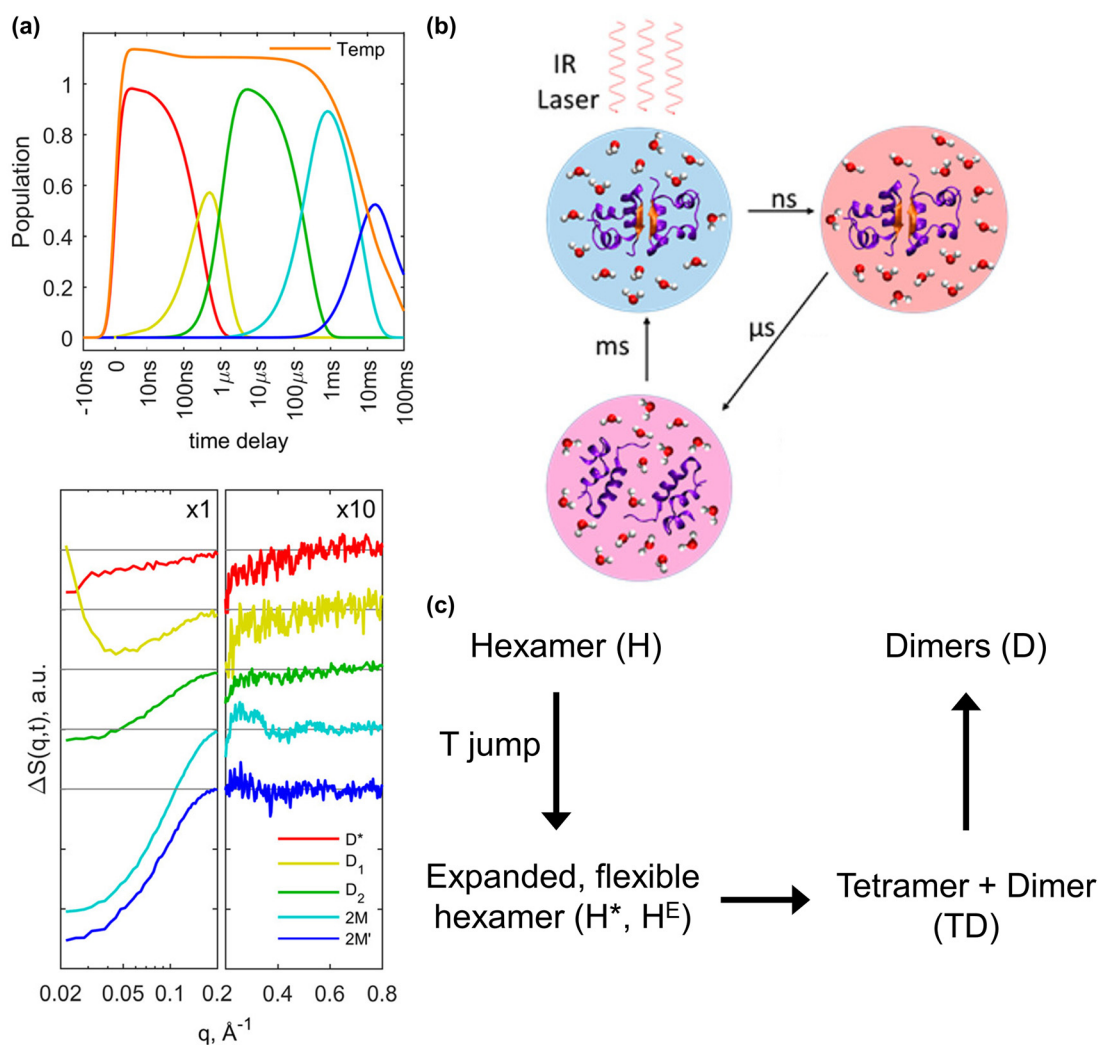


**FIG. 25.** (a) Kinetic analysis of the TRXL data from the insulin dimer. (Top) The time profiles of the populations of the reaction intermediates of the insulin dimer upon a T-jump. The change in temperature is also shown. (Bottom) The SADSs of the reaction intermediates. The time profiles of the populations and SADSs of  $D^*$ ,  $D_1$ ,  $D_2$ , 2M, and  $2M'$  are shown in red, yellow, green, cyan, and blue, respectively. For clarity, the WAXS region of the SADSs is scaled up by 10. (b) Schematic for the photoreaction of the insulin dimer revealed by TRXL. On the nanosecond timescale, the increase in the temperature induces the structural change of an insulin dimer while maintaining its dimeric form. On the microsecond timescale, the insulin dimer dissociates into insulin monomers. Finally, the insulin monomer recovers to the insulin dimer on the millisecond timescale. Reproduced with permission from Rimmerman *et al.*, J. Phys. Chem. Lett. 8, 4413 (2017). Copyright 2017 American Chemical Society. (c) Schematic for the photoreaction of the insulin hexamer elucidated by TRXL. Upon T-jump, an insulin hexamer becomes expanded and flexible. Then, the insulin hexamer dissociates into a tetramer and a dimer. Finally, the insulin tetramer further dissociates into two insulin dimers.



timescale, is similar to that of 2M in the SAXS region, but the signal of the WAXS region is smaller than that of 2M. This result indicates that a structural rearrangement of the monomer occurs during the transition from 2M to 2M' prior to the dimer formation through recombination with another monomer. Although such a rearrangement preceding association had been suggested previously, the TRXL study offered evidence for the rearrangement.

## 2. Insulin hexamer

At a lower temperature (15 °C), insulin can form a hexamer, which was confirmed via T-dependent static x-ray scattering and CD spectroscopy experiments, although dimers also exist with a large population at 15 °C. In the T-jump TRXL experiment on insulin hexamers, a T-jump was induced using an IR laser in a similar way to the experiment on dimers.<sup>230</sup> The TRXL data ranging from 10 ns to 100 ms can be described using a kinetic model with four reaction intermediates, represented by difference scattering curves at 10 ns, 20  $\mu$ s, 2 ms, and 100 ms, respectively. The difference scattering signals of the first two intermediates (H<sup>+</sup> and HE), which are formed before 1 ms, show distinct signals only in the SAXS region but not in the WAXS region. Therefore, those intermediates were assigned to the states in which the protein is expanded and has a flexible conformation rather than the dissociation of a hexamer [Fig. 25(c)]. Such dynamics that occur at the beginning of protein dissociation are expected to be similar to those occurring at the end of protein association. On the basis of these considerations, it was suggested that insulin exists as an expanded state immediately after protein association and then becomes a compact state through internal restructuring. The difference scattering signal for the last intermediate (3D) shows distinct features not only in the SAXS but also in the WAXS region. The difference scattering curve for 3D is similar to the hexamer-to-dimer transition obtained from a T-dependent static x-ray scattering experiment. In addition, it shows qualitative agreement with the theoretical difference scattering curve calculated using the crystal structures of the hexamer and the dimer. Based on these results, the last intermediate was assigned to dimers dissociated from a hexamer [Fig. 25(c)]. The difference scattering curve of the third intermediate (TD) has distinct features in both the SAXS and WAXS regions, but the signal in the WAXS region is different from that of 3D. Therefore, this intermediate was assigned to a pair of a tetramer and a dimer, which is dissociated from a hexamer [Fig. 25(c)].

## B. Poly-L-glutamic acid (pH jump)

Protein function and conformation are significantly affected by the surrounding chemical environment. For example, as the protonation state of protein residues changes according to a change in pH, the structure and function of a protein can be affected. Such a structural change in a protein in response to a change in pH was investigated using TRXL.<sup>231</sup>

Poly-L-glutamic acid (PGA) is a polypeptide composed of glutamic acids, and the conformation of PGA varies according to pH. At a neutral pH, PGA has an unfolded state due to the negative charges in the Glu residues.<sup>232</sup> In contrast, at a low pH, the residues are protonated and lose negative charges. Consequently, peptide folding occurs, accompanying the formation of  $\alpha$  helices.<sup>233,234</sup> It is known that the peptide folding kinetics of PGA are affected by the peptide length, that is, the number of constituent amino acids. The structural

dynamics of PGA upon a change in pH and its peptide length dependence were explored using pH-jump TRXL.

In pH-jump TRXL, a photoacid is used to induce the change in pH. Since photoacids release protons upon photoexcitation, the photoexcitation of photoacids lowers the pH of the target systems. For example, a photoacid called *o*-nitrobenzaldehyde (*o*-NBA) was used for the pH-jump TRXL study on PGA. As a result of the pH jump, after photoexcitation, the pH was decreased by 0.5 from its initial value of 6. The pH-jump TRXL experiment was performed on PGA peptides with multiple chain lengths to reveal the structural dynamics for a time range from 250 ns to 100  $\mu$ s. To confirm the structural change upon a change in pH, a pH-dependent static x-ray scattering experiment on PGA was performed prior to the pH-jump TRXL experiment. The results indicated that the scattering signals at a low pH correspond to monodisperse peptides, indicating that PGA forms a folded structure with  $\alpha$  helices. At a neutral pH, a new peak emerged in the SAXS region, and the signal in the WAXS region decreased compared to the signal collected at a low pH. It was suggested that the signal change in the SAXS region originates from the interchain interactions between the PGA molecules due to the repulsive force. Such interchain interactions result in interchain packing, where the peptides maintain a certain distance from each other. For the signal change in the WAXS region, it was suggested to originate from the loss of the  $\alpha$  helices.

The pH-jump TRXL data from PGA, consisting of 200 amino acids, indicated that two species (I<sub>p</sub> and F<sub>p</sub>) participate in the reaction [Fig. 26(a)]. I<sub>p</sub> is an intermediate generated before 250 ns, the first time delay of the experiment. In the SADS of I<sub>p</sub>, the SAXS region has strong signals, whereas the signal in the WAXS region is much weaker. The signal in the SAXS region is similar to that due to the interchain packing change obtained from the pH-dependent static x-ray scattering experiment. Therefore, it was suggested that the inter-PGA distance changes due to residue protonation in I<sub>p</sub> [Fig. 26(b)]. The amplitude of the SAXS data does not change significantly after the generation of I<sub>p</sub>, implying that the change in the protonation state of the peptides and the change in the interchain interactions are already completed within 250 ns. F<sub>p</sub> is a state formed with a time constant of 1.8  $\mu$ s, and the distinct signals in both the SAXS and WAXS regions are observed in the SADS of F<sub>p</sub>. The SADS of F<sub>p</sub> is similar to the difference scattering curve before and after the helix formation obtained from the pH-dependent static x-ray scattering experiment, indicating that helix formation occurs in F<sub>p</sub> through a pH jump [Figs. 26(b) and 26(c)]. The pH-jump TRXL experiments were also performed on several PGAs with different peptide chain lengths, such as 20, 50, and 100, to study the chain length dependence of the dynamics. The kinetic models are similar regardless of the chain length, but the time constants for the I<sub>p</sub>-to-F<sub>p</sub> transition vary. The chain-length-dependent kinetics were explained using the nucleation-propagation mechanism for protein folding.<sup>234</sup> In this mechanism, helical nucleation occurs as a local process, and helix formation then spreads to the entire protein, making protein folding dependent on peptide length.

## C. Cytochrome c (pH jump and electron transfer)

Another example in which protein structure is affected by pH is cytochrome c (cyt-c). For example, the ligation state of cyt-c can be altered by a change in pH [Fig. 27(a)]. At a neutral pH, His26 or His33 can be ligated to the axial position of the heme group in the unfolded state of cyt-c.<sup>151</sup> At a lower pH, because His residues are protonated,

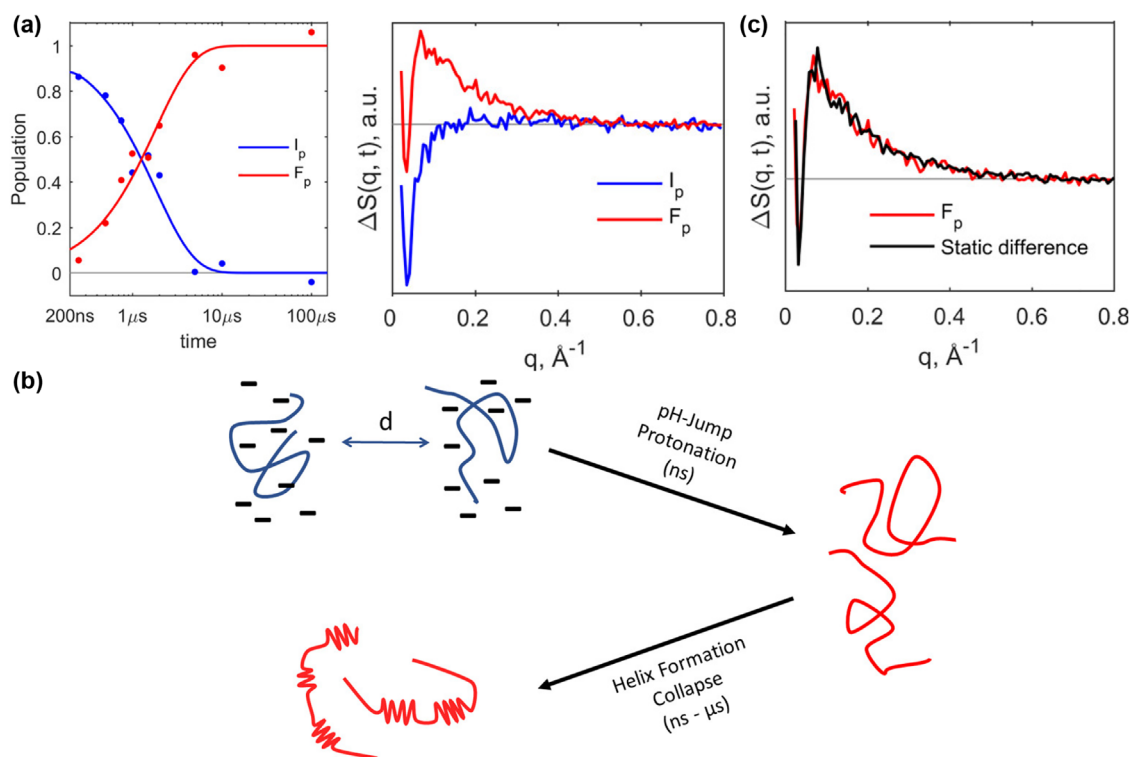


**FIG. 26.** (a) (Left) Time profiles for the populations of the reaction intermediates of PGA. (Right) SADSs of the reaction intermediates obtained from the TRXL data from PGA. Those for  $I_p$  and  $F_p$  are shown in blue and red, respectively. (b) Reaction pathway of PGA upon a change in pH. Upon 'pH jump', the protonation of PGA and change in the interchain interaction occur on the nanosecond timescale, followed by the helix formation on the nanosecond to microsecond timescale. (c) Comparison between the SADS of  $F_p$  (red) and the experimental difference scattering curve upon the change in pH obtained from a static x-ray scattering experiment (black). Reproduced with permission from Rimmerman *et al.*, J. Phys. Chem. B **123**, 2016 (2019). Copyright 2019 American Chemical Society.

a water molecule can be ligated to the axial position instead of the His residues.<sup>153</sup> Such different ligation states of the heme group can affect the folding process of cyt-c. To investigate the change in the ligation state depending on pH, pH-jump TRXL was also performed on cyt-c.<sup>235</sup>

The 'pH jump' was performed using a photoacid called *o*-NBA, which was also used in the TRXL study on PGA, and proton release occurred approximately  $\sim 20$  ns after the photoexcitation. The ligand exchange reaction was initiated by lowering the pH from 5.5 to 4.5 via a 'pH jump'. As a result of a kinetic analysis using SVD on the TRXL data from 5  $\mu$ s to 80 ms, it was found that two species ( $I_{H^+}$  and  $U_{H^+}$ ) are involved in the dynamics [Fig. 27(b)].  $U_{H^+}$ , formed later than  $I_{H^+}$ , is generated with a time constant of 4 ms. The difference scattering curve at 20 ms, which can represent the TRXL signal of  $U_{H^+}$ , shows similar features to the difference scattering curve due to the change in the ligation state from a His residue to a water molecule, which was obtained from a pH-dependent static x-ray scattering experiment [Fig. 27(c)]. Therefore,  $U_{H^+}$  was assigned to the state in which the axial ligand is changed from a His residue to a water molecule. Regarding  $I_{H^+}$ , formed in a microsecond timescale, it was suggested that  $I_{H^+}$  is not an intermediate with heme-related changes because such an intermediate had not been identified in that time domain in previous optical spectroscopy studies. The SADS of  $I_{H^+}$  shows a positive feature overall, indicating that slight protein contraction occurs.

In Sec. IV A 4, the TRXL studies on the folding dynamics of cyt-c triggered by photoexcitation are introduced. In fact, the folding of cyt-c can be induced by stimuli other than photoexcitation. A representative example of such stimuli is electron transfer (ET). Upon the reduction of the heme group from the ferric state [Fe(III)] to the ferrous state [Fe(II)], protein folding occurs in a time period of longer than microseconds.<sup>236</sup> Such folding dynamics of cyt-c have been investigated via TRXL, which used ET to initiate the reaction.<sup>235,237</sup> As previously mentioned, the change in the ligation state due to the change in pH can affect the folding dynamics of cyt-c. To study the effect of pH on folding dynamics, a TRXL experiment using ET was performed on cyt-c at two different pHs in the same study that used a 'pH jump'. ET was induced using the photoexcitation of  $[\text{Ru}(\text{bpy})_3]^{2+}$ , and the measurement was performed for a time range between 100  $\mu$ s and 1 ms, considering the time for ET and back ET to occur. The TRXL signal due to the structural change in the protein was not observed in the data collected at a pH of 7 [Fig. 27(d)], which implied that protein folding does not occur in the measured time domain when a His residue is ligated. On the other hand, when the pH was set to 4, the TRXL signal that originated from the structural change was observed in several hundred microseconds [Fig. 27(d)]. The TRXL data exhibited a negative signal in the SAXS region but no distinct signal in the WAXS region. This result indicated that the loss of a ligated water molecule occurs, yielding a

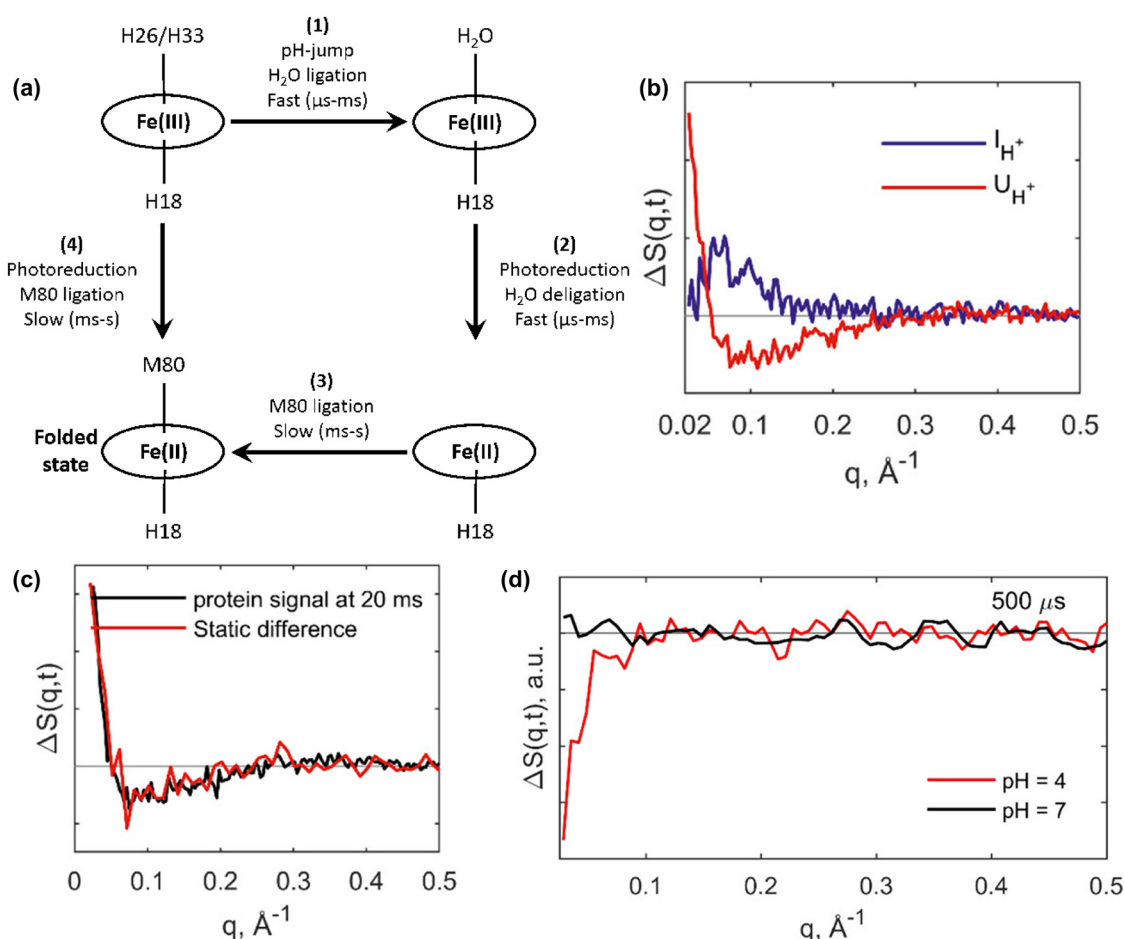


**FIG. 27.** (a) Schematic for the folding of cyt-c under various pHs and oxidation states. (b) SADSs of the reaction intermediates formed upon a 'pH jump' obtained from the kinetic analysis of the TRXL data from cyt-c. (c) Comparison between the experimental difference scattering curve at 20 ms collected from a TRXL experiment (black) and the experimental difference scattering curve due to the change in the axial ligand upon a change in pH obtained from a static x-ray scattering experiment (red). (d) Experimental difference scattering curves of cyt-c at 500 μs from TRXL experiments using ET collected under pHs of 7 (black) and 4 (red). Reproduced with permission from Rimmerman *et al.*, J. Phys. Chem. B **122**, 5218 (2018). Copyright 2018 American Chemical Society.

reduced five-coordinate heme group while the overall protein structure is maintained.

A TRXL study using ET was also performed over a wider time range.<sup>237</sup> In this study, the heterogeneity in the unfolded state, different kinetics for protein folding due to the heterogeneity, and structural characteristics of the reaction intermediates were revealed via TRXL. Nicotinamide adenine dinucleotide (NADH) was used to induce ET, which, in turn, initiated the reaction, and TRXL data were measured over a wide time domain from 31.6 μs to 316 ms. In addition to the TRXL experiment, to obtain structural information about the unfolded and folded states, a static x-ray scattering experiment was performed on the oxidized state (unfolded state) and the reduced state (folded state). Then, the ensembles of protein structures that describe the static x-ray scattering signals of the oxidized and reduced states well were obtained using MD simulations and the EOM. According to the results, at least four conformations are required for the unfolded state, whereas the folded state is described

with only one conformation [Fig. 28(a)]. This result indicated the heterogeneous nature of the unfolded state.

The kinetic analysis results of the TRXL data showed that two species (U' and F) contribute to the folding dynamics of cyt-c [Fig. 28(b)]. Transitions between these species cannot be described using a simple single exponential but rather using a stretched exponential or two exponential functions. According to the analysis using the maximum entropy model, the stretched exponential model is more suitable than the model with two exponential functions. The stretched exponential kinetics indicate that the U'-to-F transition occurs through various pathways due to the heterogeneous characteristics of the unfolded state [Fig. 28(c)]. The F state is formed with a time constant of 185 ms, and the SADS of the F state is similar to the difference scattering curve between the reduced and oxidized states of cyt-c obtained from the static x-ray scattering experiment [Fig. 28(b)]. Based on this result, the F state was assigned to the folded state. The U' state is formed within 31.6 μs, and considering the time for the



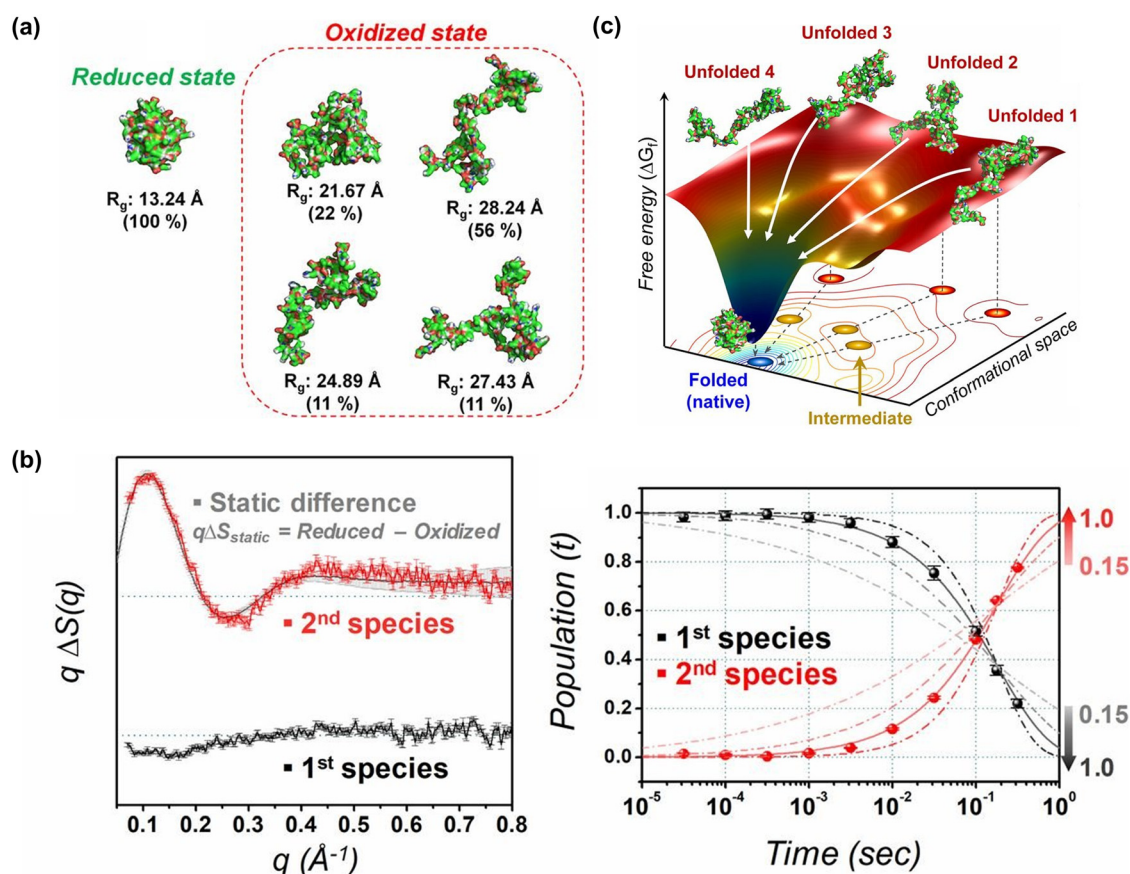


**FIG. 28.** (a) Representative structures for the oxidized and reduced states of cyt-c obtained from the structure refinement using the MD simulations and EOM. The structure refinement was performed on the static x-ray scattering data from oxidized and reduced cyt-c. (b) (Left) SADSs of the reaction intermediates formed during the folding of cyt-c (black and red) obtained from the kinetic analysis of the TRXL data and the experimental difference scattering curve upon the folding of cyt-c obtained from a static x-ray scattering experiment (gray). (Right) Time profiles of the populations of the reaction intermediates obtained from the kinetic analysis of the TRXL data (circles) and their fits (solid line). Gray lines indicate the time profiles, assuming different stretching exponents ( $\beta$ ) ranging from 0.15 to 1. The fits were obtained when  $\beta$  was 0.7. The first and second species correspond to U' and F, respectively. (c) Schematic for the folding pathway of cyt-c. Reproduced with permission from Kim *et al.*, *Proc. Natl. Acad. Sci. U. S. A.* 117, 14996 (2020). Copyright 2020 Authors, licensed under a Creative Commons Attribution (CC BY-NC-ND) License.

reduction via the solvated electron generated through NADH ( $\sim 33 \mu\text{s}$ ), it was suggested that U' has a reduced heme group. The SADS of U' has a negative feature in the SAXS region, indicating that protein expansion occurs. Therefore, it was suggested that, under the experimental conditions, cyt-c passes through an intermediate distinct from a molten globule state because a molten globule state would have a more compact structure than the unfolded state.

#### D. ATP-binding proteins (photocaged molecule)

Many proteins perform their functions through structural changes induced by interactions with other small molecules. A typical example of a small molecule inducing structural changes is a nucleotide, such as ATP. These small molecules can induce reactions such as the binding of a protein to another protein and the phosphorylation of a protein residue, thereby participating in molecular transport or signal transduction.<sup>238–240</sup> Therefore, elucidating the structural changes in proteins activated by these small molecules is essential for understanding the functions of various proteins.

#### 1. Nucleotide-binding domain from MsbA

MsbA is one of the proteins that perform their functions using ATP. MsbA is a lipid flippase, a type of ATP-binding cassette (ABC) transporter, and plays a role in transporting lipids.<sup>240,241</sup> MsbA has a nucleotide-binding domain (NBD), and, after ATP binding, the NBD undergoes dimerization [Fig. 29(a)], causing a change in the overall structure of the protein and lipid transport.<sup>242</sup> Structural dynamics caused by ATP binding to the NBD of MsbA have been studied using TRXL.<sup>243</sup> The ATP binding of the NBD was achieved through caged ATP, which releases ATP upon photoexcitation and TRXL data were obtained for the time range from 50 ms to 1400 ms [Fig. 29(b)]. According to the SVD analysis results, two reaction intermediates are involved in the reaction dynamics. An intermediate generated in the late time was assigned to a dimerized form derived from ATP binding based on the increase in the signal in the SAXS region and the similarity of the TRXL signal to the difference scattering curve for the dimerization calculated using the crystal structures. A more detailed structural analysis was performed by analyzing the  $R_g$  using data from

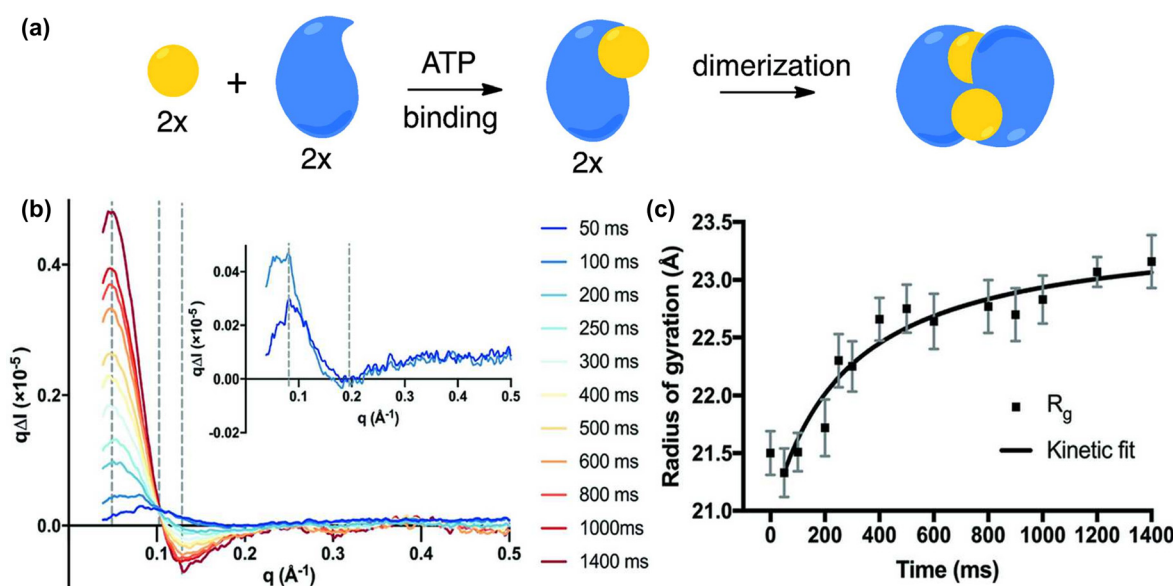


**FIG. 29.** (a) Schematic for the dimerization reaction of the NBD of MsbA. The protein and ATP are labeled blue and yellow, respectively. (b) Experimental difference scattering curves of the NBD of MsbA obtained from a TRXL experiment. The time delays increase from blue to red. The difference scattering curves at the first two time delays are shown in the inset. (c) Time profile of the  $R_g$  (black square) and its fit (black line) obtained from TRXL. Adapted from Josts *et al.*, IUCrJ **5**, 667 (2018). Copyright 2018 Authors, licensed under a Creative Commons Attribution (CC BY) License.

the SAXS region or by obtaining a low-resolution model. The analysis results indicated that the  $R_g$  increased with time, coinciding with the generation of a dimer [Fig. 29(c)]. Furthermore, the low-resolution structure of the NBD at 1400 ms is similar to the crystal structure of the dimer. The difference scattering curve of the intermediate generated in the early time shows a different feature from that of the dimer, and this intermediate was assigned to a state with a change in the internal structure of the NBD by ATP binding.

## 2. Sarco/endoplasmic reticulum $\text{Ca}^{2+}$ ATPase

The structural change in a protein induced by phosphorylation after ATP binding is another example studied via TRXL.<sup>244</sup> Sarco/endoplasmic reticulum (SR/ER)  $\text{Ca}^{2+}$  ATPase (SERCA) is a protein abundantly present in the membrane of the SR and plays a role in transporting  $\text{Ca}^{2+}$  from the cytosol to the SR. The cytoplasmic domain of SERCA is mainly composed of three domains: the nucleotide-binding (N) domain, the phosphorylation (P) domain, and the actuator (A) domain [Fig. 30(a)]. Additionally, there is another domain, called the membrane (M) domain, located at a membrane of the SR and ER. When SERCA binds two  $\text{Ca}^{2+}$  cations and one ATP, the phosphorylation of a protein residue and a structural change in the protein occur to transport  $\text{Ca}^{2+}$  cations.<sup>245</sup> The states of SERCA can be categorized into two states: an E1 state with high ion affinity and an E2 state with low ion affinity.<sup>246,247</sup> Reaction intermediates with different phosphorylation states and protein structures participating in the transition between these two states were determined through crystallographic studies.<sup>245</sup> The TRXL study tracked the movement of SERCA in the solution phase with the aid of prior knowledge obtained from crystallographic studies. The sample solution used for the TRXL

experiment was saturated with  $\text{Ca}^{2+}$  cations so that  $\text{Ca}^{2+}$  cations could bind to SERCA before the ATP release. Then, the ATP release from the photocaged molecules occurred upon photoexcitation to initiate the structural change in SERCA. The TRXL data ranging from 20  $\mu\text{s}$  to 200 ms can be best described using a kinetic model in which three intermediates participate [Fig. 30(b)]. Among the intermediates, a detailed analysis was performed on the second species (intermediate state) and the last species (late state). Structure refinement was performed in two steps. In the first step, using MD simulations, the crystal structure of  $[\text{Ca}_2]\text{E1}$  (the E1 state bounded with two  $\text{Ca}^{2+}$  cations), representing the ground state (prepulse state), was driven toward other crystal structures, such as  $[\text{Ca}_2]\text{E1ATP}$  (the E1 state bounded with two  $\text{Ca}^{2+}$  cations and ATP) and E2P (the phosphorylated E2 state). Then, protein structures that best described the SADSs of the intermediates were selected from the snapshots from the MD simulations. In the second step, MD simulations considering the membrane around the protein were performed on the protein structures selected in the first step and the  $[\text{Ca}_2]\text{E1}$  crystal structure to describe the effect of the membrane. Finally, from the protein structures obtained from the MD simulations considering the membrane, structure pairs that could describe the SADSs well were selected and used for structural characterization. The structure refinement result indicated that the ground state has a more compact conformation than the crystal structure of  $[\text{Ca}_2]\text{E1}$ . The N and A domains are located closer in the solution than in the crystal. In the intermediate state, the cytoplasmic domains have a more closed conformation compared to that of the ground state [Fig. 30(c)]. In the late state, the structure and position of the N domain are similar to that of the E1 state. Still, the movement of the A domain, which is observed in the crystal structure of the E2P state, partially occurs [Fig. 30(c)]. In addition, the nucleotide-binding site is

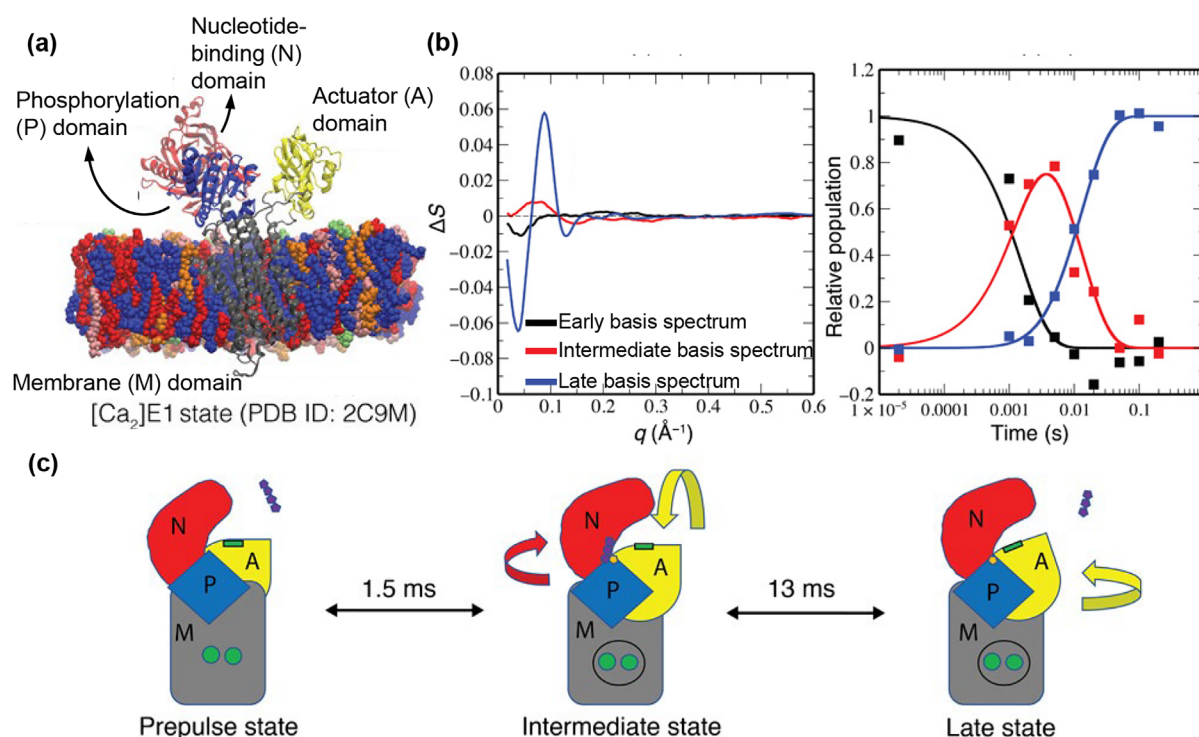


**FIG. 30.** (a) Molecular structure of SERCA surrounded by sarcoplasmic reticulum membrane mimics. The nucleotide-binding (N), actuator (A), phosphorylation (P), and membrane (M) domains are labeled with red, yellow, blue, and gray colors, respectively. (b) (Left) The SADs of the reaction intermediates of SERCA upon ATP binding obtained from the TRXL data from SERCA. (Right) The corresponding time profiles of the populations of the reaction intermediate. The SADs and time profiles of the populations for the early, intermediate, and late states are shown in black, red, and blue, respectively. (c) Schematic for the structural change in SERCA upon ATP binding elucidated by TRXL. The labels and colors for the protein domains are the same as in (a). Green spheres indicate the  $Ca^{2+}$  cations. ATP and ADP are represented by chains of four and three purple pentagons, respectively. The green rectangle and yellow pentagon indicate the Thr-Gly-Glu-Ser (TGES) motif and phosphorylated residue, which become closer during the E1-to-E2 transition. Adapted with permission from Ravishanker *et al.*, *Sci. Adv.* **6**, eaaz0981 (2020). Copyright 2020 Authors, licensed under a Creative Commons Attribution 4.0 License.

exposed in the late state. Based on these results, the late state was assigned to the  $[Ca_2]E1P$  state, which had not been reported by crystallographic studies.

### 3. Adenylate kinase

A TRXL study using ATP binding was also performed on adenylate kinase (AdK).<sup>248</sup> AdK is involved in the conversion of diverse adenosine phosphates. For example, AdK binds with an adenosine 5'-monophosphate (AMP) and an ATP to convert them into two adenosine 5'-diphosphates (ADPs).<sup>239</sup> In terms of structure, AdK consists of the AMP-binding domain (NMPbd), ATP-binding domain (LIDbd), and central domain (CORE domain) [Fig. 31(a)]. Based on crystal structures collected under different conditions, AdK has closed and open configurations,<sup>249,250</sup> and the kinetics for the transition between the two configurations were reported as well.<sup>251,252</sup> Using TRXL, structural dynamics over a wide time range and cooperativity related to the closing motion of AdK were revealed. AMP-bound AdK was used for the TRXL experiment, and photocaged ATP was uncaged and released upon photoexcitation to initiate structural changes via ATP binding. TRXL data were collected for the time domain of 20  $\mu$ s to 25 ms, and the kinetic analysis of the TRXL data identified two intermediates (the early intermediate and late intermediate). The early intermediate is

formed even at the earliest time delay and transforms into the late intermediate with a time constant of 4.3 ms [Figs. 31(b) and 31(c)]. The formation of the early intermediate occurs earlier than the ATP-release time (millisecond timescale), and the early intermediate was excluded from the structure refinement as the early intermediate may be irrelevant to ATP binding. Structure refinement was performed using the results of the MD simulations based on the crystal structures of the closed and open configurations. Various structure pairs were made using snapshots obtained through MD simulations, and the degrees of agreement between the theoretical difference scattering curves of the structure pairs and the SADS of the late intermediate were calculated. The ten structure pairs with the highest agreement showed that partial closing occurs upon photoexcitation [Fig. 31(d)]. During this closing motion, not only LIDbd, where an ATP molecule is bound but also NMPbd, where an AMP molecule is bound, moves. Through this, it was suggested that the closing motion of AdK has a cooperative mechanism. In addition, according to the MD simulation results, a partial unfolding of the secondary structure in LIDdb occurs. Based on this result, it was suggested that the structural change obtained from the TRXL data is consistent with the cracking model, in which the conformation transition accompanies the local unfolding and refolding of the secondary structure.<sup>253</sup>



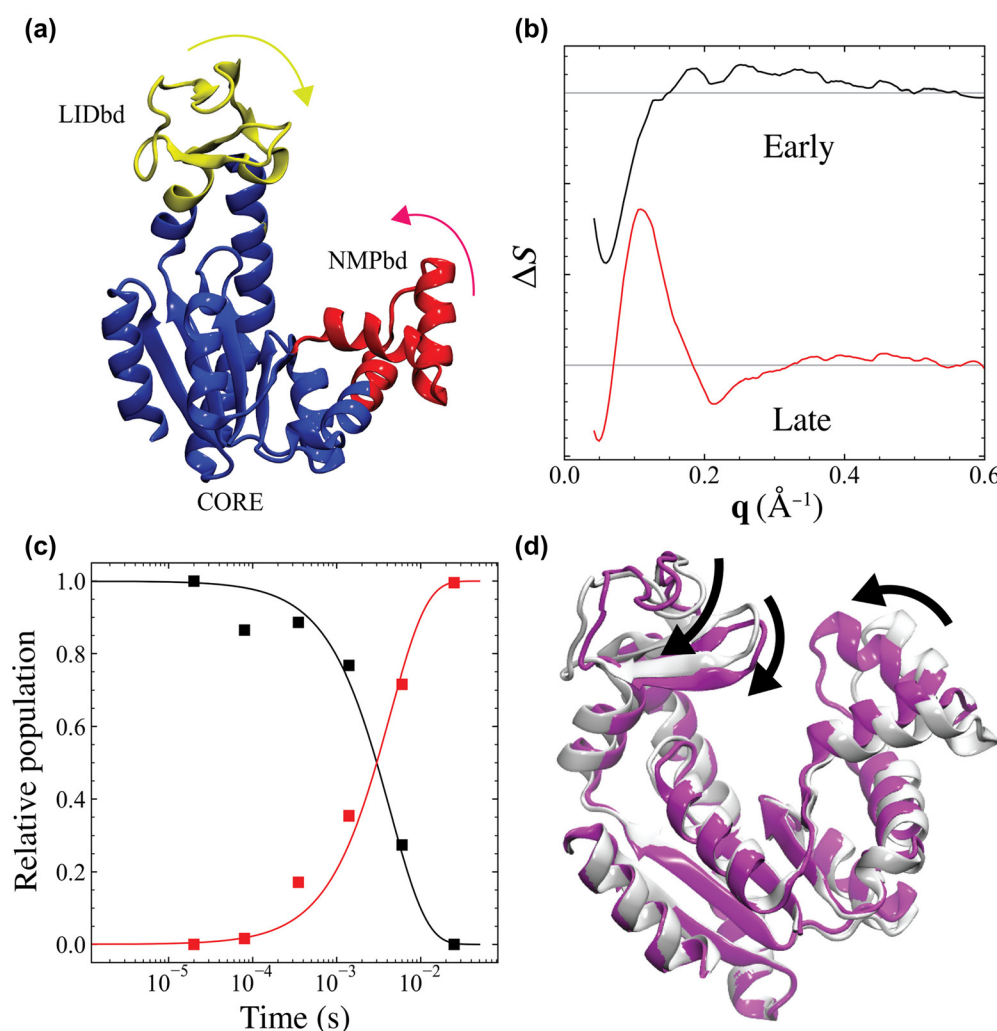


**FIG. 31.** (a) Molecular structure of AdK in its open form. The AMP-binding domain (NMPbd), ATP-binding domain (LIDbd), and central domain (CORE domain) are shown in red, yellow, and blue, respectively. The structural change upon substrate binding is indicated by arrows. (b) SADs of the reaction intermediates of AdK upon ATP binding. (c) Time profiles of the reaction intermediates corresponding to (b). The SADs and time profiles were obtained from the kinetic analysis of the TRXL data. For (b) and (c), the early and late intermediates are labeled as black and red, respectively. (d) Structural change in Adk upon ATP binding revealed by TRXL. The substrate-unbound and substrate-bound structures are shown in white and magenta, respectively. Reproduced with permission from Orådd *et al.*, *Sci. Adv.* **7**, eabi5514 (2021). Copyright 2021 Authors, licensed under a Creative Commons Attribution 4.0 License.

## E. Other examples

### 1. Hemoglobin

As mentioned in Sec. IV A 1, the structural heterogeneity of Hb in the R state was reported via multiple crystal structures, such as R and R2.<sup>112,113</sup> A T-jump TRXL study on Hb proposed that the structural heterogeneity of Hb may also be found in the solution phase.<sup>254</sup> Prior to a T-jump TRXL experiment, a T-dependent static x-ray scattering experiment was performed on carbonmonoxy Hb (HbCO) and deoxy Hb (deoxyHb), which represent the R and T states, respectively, and the difference scattering curves of the two proteins due to the temperature change were obtained. The difference scattering curves of HbCO and deoxyHb have different shapes [Fig. 32(a)]. A difference scattering curve has two contributions: one from the change in the

hydration shell and the other from the change in the protein structure. Based on the assumption that the change in the hydration shell would be similar for HbCO and deoxyHb, it was proposed that the inconsistency in the difference scattering curves originates from the different structural changes in HbCO and deoxyHb. Nevertheless, it was not determined whether only one or both proteins undergo structural changes. To answer this question, a T-jump TRXL experiment covering the time range from 316 ns to 100  $\mu$ s was conducted. The TRXL data from HbCO show time-dependent changes in the WAXS region [Fig. 32(b)], but those from deoxyHb do not show such time dependence. This difference indicates that only HbCO undergoes a structural change upon a T-jump. Based on this result, it was suggested that the R state of Hb has at least two conformations and that the x-ray scattering intensity changes upon a T-jump due to the change in the

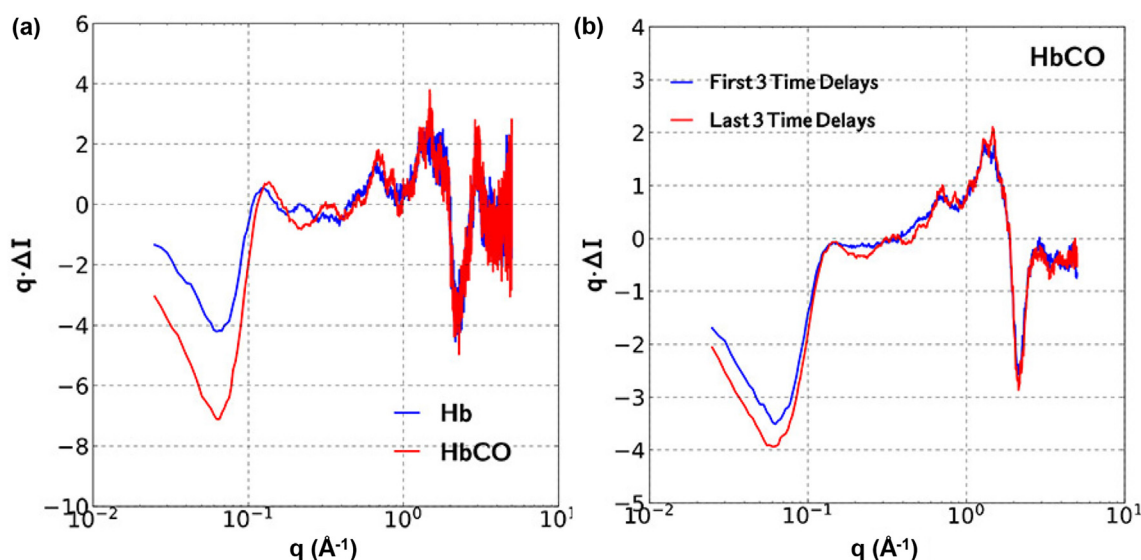


**FIG. 32.** (a) Experimental difference scattering curves of deoxyHb (blue) and HbCO (red) upon a temperature change of 13 °C obtained from a static x-ray scattering experiment. The different shapes of the difference scattering curves of Hb in two different conditions imply that the structural changes of the two proteins upon the temperature change are different, although it remains uncertain whether the structural change occurs in both or only one protein. (b) Comparison of the averaged experimental difference scattering curves of the first three time delays (blue) and the last three time delays (red) obtained from a TRXL experiment on HbCO. The averaged difference scattering curve at the last three time delays shows different features in the WAXS region compared to that at the first three time delays, indicating that the protein structure of HbCO changes upon T-jump. Adapted with permission from Cho *et al.*, J. Phys. Chem. B **122**, 11488 (2018). Copyright 2018 American Chemical Society.

equilibrium between the conformations. In addition, it was proposed that the difference between the time constants for the R–T transition reported by the previous TRXL studies ( $\sim 2 \mu\text{s}$ ) and spectroscopic studies ( $\sim 20 \mu\text{s}$ ) can be explained using multiple conformations of the R state.

## 2. Cyclophilin A

Cyclophilin A (CypA) is a peptidylprolyl isomerase and functions as a protein-folding chaperone.<sup>255</sup> In addition, CypA is known to affect the organ rejection process after transplantation. In an NMR study on CypA, the movements of a loop near the active site (loop region) and several residues extended between the active site and the protein core (core region) were observed.<sup>256</sup> These movements have relevance to the function of the protein. For example, the substrate binding specificity is changed when the loop region is mutated, while a mutation in the core region induces the reduction of catalytic activity.<sup>257,258</sup> Such motions of CypA can be significantly affected by temperature. To confirm the effect of temperature change on the structural dynamics of CypA, a T-jump TRXL experiment was performed on CypA.<sup>259</sup> In particular, through a comparison with other mutants, the key structure domain affecting the catalytic activity of CypA was unveiled. A T-jump was induced using IR irradiation, which generated a temperature increase by  $\sim 10.7^\circ\text{C}$ . By tracking the signal in the SAXS region of the TRXL data, a two-step kinetic model was established. A structural analysis was performed by using the Guinier analysis on the static scattering curve at each time delay, which was generated by adding the static scattering curve in the ground state to the difference scattering curve of each time delay. The  $R_g$  obtained from the Guinier analysis was used to extract information

about global structural change. According to the analysis results, protein contraction occurs before the first time delay (562 ns). Then, the protein is expanded over a few microseconds, corresponding to the fast kinetic component, and, eventually, it is contracted again over a few tens of microseconds, which corresponds to the slow kinetic component. In addition to WT, T-jump TRXL was performed on the D66N/R69H mutant and the S99T mutant, which have mutations in the loop region and core region, respectively, to investigate how each region affects the protein dynamics. The kinetic analysis showed that the slow kinetic component is not observed in the S99T mutant, whereas the fast kinetic component is not observed in the D66N/R69H mutant. The absence of the slow kinetic component in the S99T mutant indicated that the structural change corresponding to the slow kinetic component affects the catalytic activity. Additionally, it was suggested that the fast kinetic component in the D66N/R69H mutant was not observed due to the accelerated rate of the structural change, which positioned it out of the time window of the TRXL experiment.

## 3. Bovine $\alpha$ -lactalbumin (BLA)

Protein structures are closely related to the functions of proteins. Still, some proteins, called intrinsically disordered proteins, do not have fixed tertiary structures. Moreover, a disordered state of proteins can play a role in unfolding. In this regard, the study of the disordered structure of a protein can be regarded as an important topic for protein structure studies. One of the model systems for proteins with such a disordered structure is bovine  $\alpha$ -lactalbumin (BLA) [Fig. 33(a)]. BLA can form a molten globule state during protein unfolding at high temperatures.<sup>260</sup> According to the reported characteristics of BLA in the molten globule state, although native-like secondary structures are

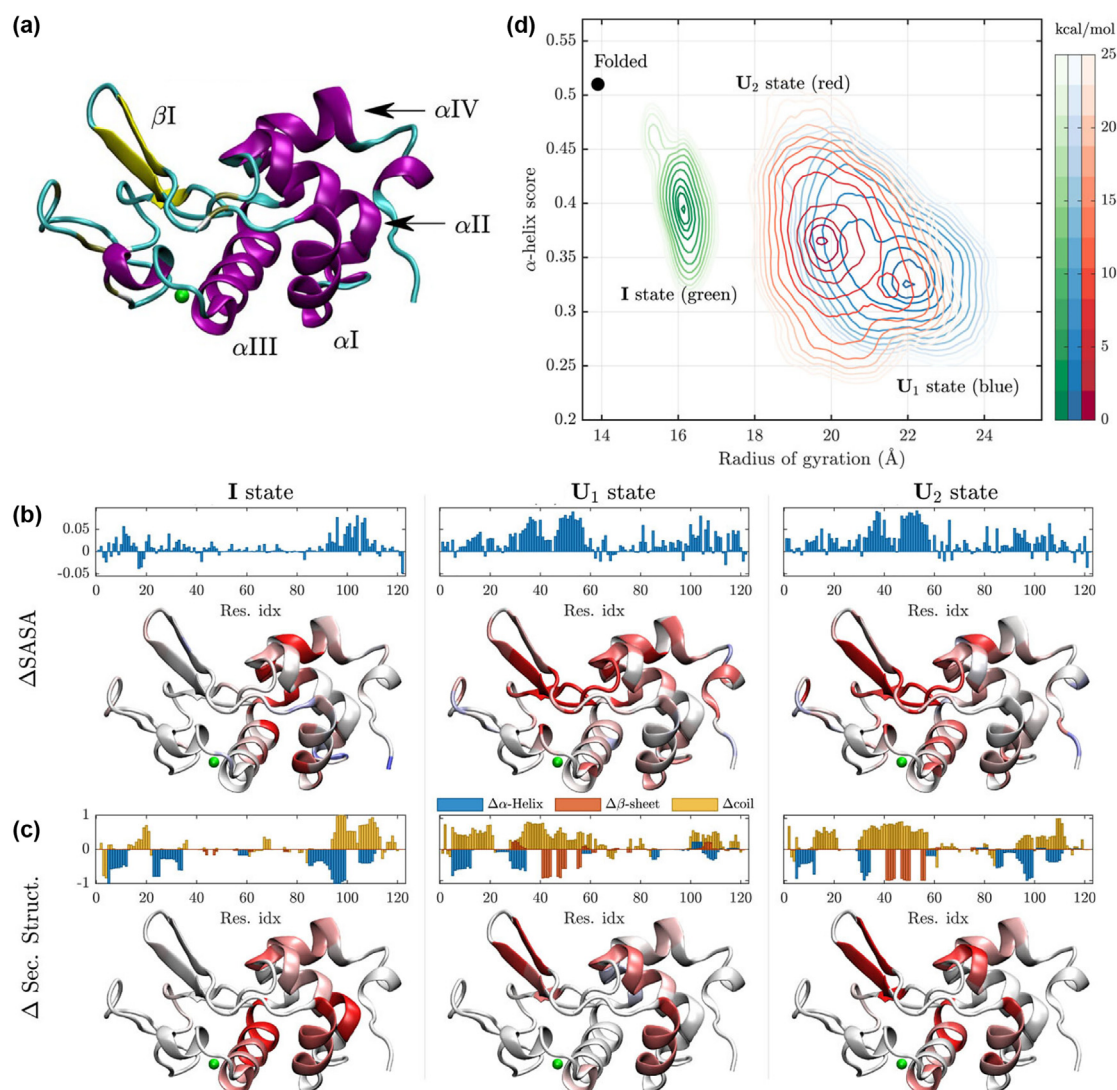


**FIG. 33.** (a) Molecular structure of BLA. The  $\alpha$  helices and  $\beta$  sheets are labeled purple and yellow, respectively. The green sphere indicates the  $\text{Ca}^{2+}$  cation bound to the protein. (b, c) Structure refinement results obtained from the TRXL data. (b) Change in the SASA for the reaction intermediates of the unfolding of BLA. The bar plots for the SASAs show the changes in the SASAs of the protein residues. For protein structures under the bar plots for the SASAs, the red color indicates the residues of which SASAs are increased, and the red color becomes pronounced as the increase in the SASA becomes larger. The green spheres in the protein structures indicate the  $\text{Ca}^{2+}$  cation bound to the protein. (c) Change in the secondary structure contents for the reaction intermediates. The bar plots for the secondary structure contents show the changes in secondary structure contents such as  $\alpha$  helices (blue),  $\beta$  sheets (red), and random coils (yellow). In the structures under the bar plots for the secondary structure contents, the residues where  $\alpha$  helices or  $\beta$  sheets are formed are labeled blue, and those where  $\alpha$  helices or  $\beta$  sheets are unfolded are labeled red, respectively. For all of the protein structures, the green sphere indicates the  $\text{Ca}^{2+}$  cation bound to the protein. (d) Free energy surfaces for the I (green),  $U_1$  (red), and  $U_2$  (blue) states obtained from the MD simulations used for the structure refinement of BLA. The minimum of each FES is set to zero. The  $R_g$  and  $\alpha$  helix score for the folded state are indicated with a black dot. Reproduced from Hsu *et al.*, J. Chem. Phys. **154**, 105101 (2021), with the permission of AIP Publishing LLC.

maintained, the  $R_g$  of the protein increases, and the packing interactions of the side chains are weakened.<sup>261,262</sup> Nevertheless, the detailed structural dynamics of the molten globule state had been unclear. The results of a T-dependent static x-ray scattering experiment indicated that the unfolding of BLA occurs with a melting temperature of  $\sim 74^\circ\text{C}$ . Building on this result, T-jump TRXL was used to investigate the pathway of the unfolding and structural features of the molten

globule and unfolded states.<sup>95</sup> IR laser irradiation was used to T-jump in a similar manner to the TRXL study on insulin (Sec. V A), and a temperature rise of  $\sim 11.5^\circ\text{C}$  was generated upon a T-jump. The TRXL data were collected for a time range from 20  $\mu\text{s}$  to 70 ms. The initial temperatures used to induce the unfolding of BLA upon a T-jump were between 60 and  $70^\circ\text{C}$ . The TRXL data could be well-described by using a kinetic model with two parallel unfolding



pathways. One pathway is a three-state pathway in which unfolding occurs via one reaction intermediate (from the folded state to the I state and then to the  $U_1$  state), and the other pathway is a two-state pathway where an unfolded state ( $U_2$ ) is formed directly from the folded state. In the three-state pathway, the I state is formed within 20  $\mu$ s and then transformed into the  $U_1$  state with a time constant of 920  $\mu$ s. The  $U_1$  state decays with a time constant of 8.6 ms. In the two-state pathway, the  $U_2$  state is formed with a rising time of 2.2 ms and decays with a time constant of 40 ms. A detailed structural analysis was performed using MD simulations driven by a score describing the disagreement between the theoretical and experimental difference scattering curves. According to the structure refinement results, the solvent-accessible surface area (SASA) of the I state increases compared to that of the ground state [Fig. 33(b)]. In addition, the  $\alpha$  helix score, which indicates the concreteness of the helices, of the I state is lower than that of the ground state, indicating that some  $\alpha$  helices lost the properties of the helix [Figs. 33(c) and 33(d)]. Meanwhile, the  $R_g$  of the I state does not increase significantly compared to that of the ground state [Fig. 33(d)]. Based on these results, it was suggested that the I state has similar characteristics to the molten globule state.

The  $U_1$  and  $U_2$  states have larger  $R_g$ s and SASAs, as well as smaller  $\alpha$  helix scores, than the I state and show the unfolding of  $\beta$  sheets, which are not significant in the I state [Figs. 33(b)–33(d)]. The origins of the increased SASAs are different for the  $U_1$  and  $U_2$  states. In the  $U_2$  state, the increase in the SASA originates from the protein expansion from the core, but in the  $U_1$  state, the residues located on the surface are more exposed to the solvent, resulting in an increase in the SASA. Based on these structural analysis results, it was suggested

that protein folding pathways vary depending on whether the solvent can access the protein core. When the protein core is accessible to the solvent, the folding process can bypass the molten globule state, owing to the easier structural rearrangement of the protein.

#### 4. Myoglobin

In addition to the unfolding of BLA, the unfolding of Mb without the heme group (apoMb) was investigated using T-jump TRXL.<sup>263</sup> The T-jump was performed using IR irradiation, as in previous studies, with the temperature increase by about 10 °C during the T-jump. Since the melting temperature of apoMb obtained from a tryptophan fluorescence experiment was about 56 °C, the initial temperature of the experiment was set to 50 °C to induce protein unfolding upon the T-jump. According to the results of the SVD analysis on the TRXL data, at least three intermediates contribute to the TRXL data. Structure refinement was performed through MD simulations. Structure ensembles that can describe the static x-ray scattering curve collected at 50 °C and the difference scattering curve at each time delay were obtained through a genetic algorithm using the snapshots from the MD simulations. Based on the SVD results, the structures composing these ensembles were clustered using the  $R_g$ , SASA, RMSD, and helicity to yield three clusters. Among the three clusters, cluster I occupies approximately 15% of the population at time delays shorter than 1  $\mu$ s, and, afterward, its population gradually decays [Fig. 34(a)]. Cluster I has a compact structure similar to that of the native structure [Fig. 34(b)], and many residue–residue contacts observed in the crystal structure were also identified. Based on these results, cluster I was assigned to

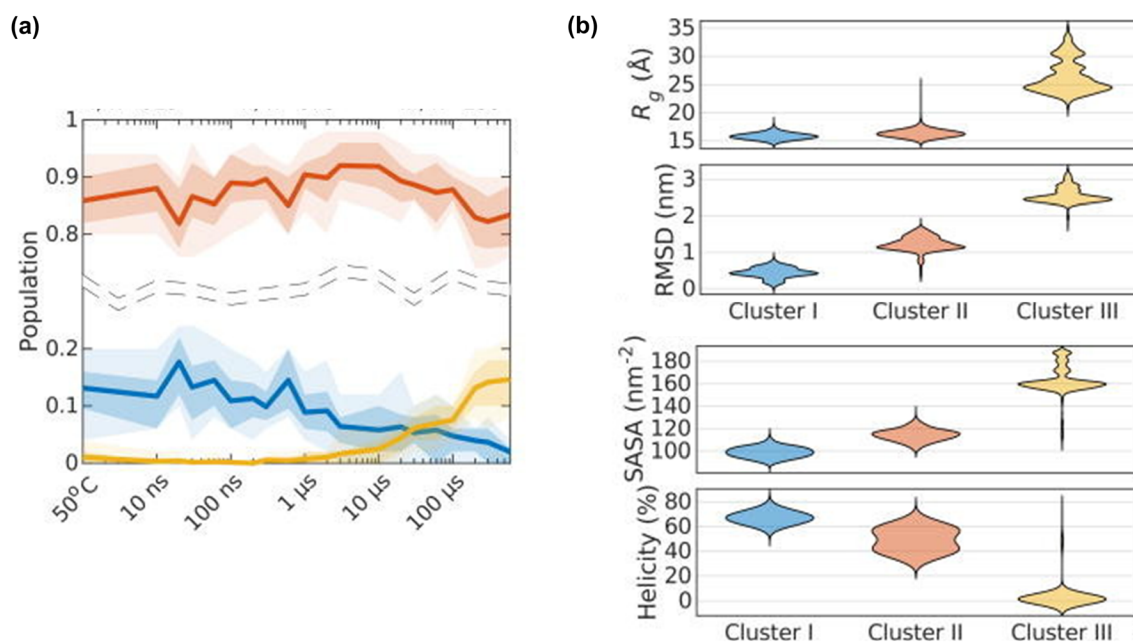


**FIG. 34.** (a) Time profiles for the populations of the three clusters obtained from the structure refinement of apoMb using the TRXL data. Clusters I–III are shown in blue, red, and yellow, respectively. Cluster II is the most dominant cluster across the time domain investigated by TRXL. Cluster I occupies ~15% of the population on the nanosecond timescale and decays over time, whereas cluster III emerges on the microsecond timescale. (b) The  $R_g$ , RMSD, SASA, and helicity of the three clusters formed during the unfolding of apoMb. The parameters for clusters I, II, and III are shown in blue, red, and yellow, respectively. The  $R_g$ , RMSD, and SASA of cluster II are larger than those of cluster I, whereas the helicity of cluster II is smaller than cluster I. Cluster III has larger  $R_g$ , RMSD, and SASA than the other clusters, while its helicity is smaller than the others. Reproduced from Henry *et al.*, *Struct. Dyn.* **7**, 054702 (2020). Copyright 2020 Authors, licensed under a Creative Commons Attribution (CC BY) License.

the native state. Cluster II is the dominant species for all of the time delays [Fig. 34(a)]. It has larger  $R_g$  and SASA as well as a less helical character than cluster I [Fig. 34(b)]. In addition, a similar pattern of the residue–residue contacts observed in the crystal structure was found as well, although the contacts have a transient character. Since these characteristics are similar to those of the molten globule state, cluster II was assigned to the molten globule state. Cluster III was observed in time delays longer than  $1\ \mu\text{s}$  [Fig. 34(a)]. The  $R_g$  and SASA of cluster III are significantly large compared to those of cluster I, whereas the helical character of cluster III is much smaller than that of cluster I [Fig. 34(b)]. Based on these results, cluster III was assigned to the unfolded state. The molten globule state revealed in this study (kinetic molten globule state) shows different characteristics from those of the equilibrium molten globule state, which was identified under low-pH conditions in a previous study.<sup>264</sup> For example, the kinetic molten globule state shows a smaller increase in the  $R_g$  than that of the equilibrium molten globule state. Based on the difference, it was suggested that the unfolding pathway of apoMb under nonequilibrium conditions may be different from that under equilibrium conditions.

## VI. SUMMARY AND OUTLOOK

The structure of a protein is an important property that is closely related to the function of a protein. TRXL is an attractive experimental method to reveal the structural dynamics of proteins and has been applied to various proteins to study their conformational changes, which are related to their functions. The outstanding advantage of TRXL is its sensitivity to the local and global structural changes in the solution phase. In exploring the structure–function relationship of proteins, it is important to elucidate the dynamic behavior of protein structures under physiological conditions. Still, experimental techniques that satisfy this requirement are rare. For example, although TRXC is an excellent method for elucidating the structure of a protein, its application is limited to proteins in the crystalline phase. NMR, which is widely used to study protein structures, generally cannot be applied to obtain high-resolution structures of large proteins and has a limited time resolution compared to other techniques. With spectroscopic methods such as TA and time-resolved vibrational spectroscopies, which are applicable to proteins in the solution phase, it is often difficult to observe global structural changes in proteins because they are sensitive only to energy states or, indirectly, to local structural changes. As this review has demonstrated, TRXL has been performed on proteins of various sizes in the solution phase, ranging from polypeptides composed of several dozen amino acids to large proteins such as a cyanobacterial phytochrome from *Synechocystis* sp. PCC6803, which consists of  $\sim 1500$  amino acids with a molecular weight of  $\sim 170$  kDa. In addition, TRXL is directly sensitive to various movements, from subtle changes in the tertiary structures of proteins to large-scale quaternary motion. Recently, with the development of XFELs, the time resolution of protein TRXL has been enhanced to be better than even 100 fs. Thanks to these characteristics, TRXL has been in the spotlight as a complementary tool for other experimental techniques, including time-resolved spectroscopic and crystallographic methods. Indeed, combining the results obtained through TRXL and other experiments has made it possible to obtain a comprehensive picture of protein structural changes, from the changes in a chromophore to global structural changes.

In this review, we summarized the TRXL studies on various proteins. TRXL was first applied to heme proteins, such as Hb, Mb, and cyt-c, which have been studied extensively as model systems with other techniques, such as time-resolved spectroscopic methods. Afterward, the applications of TRXL were broadened to include naturally photoactive proteins such as phytochrome, rhodopsin, and PYP. The structural changes in the proteins in the solution phase revealed by TRXL often differ from those in the crystal phase, suggesting the importance of studying protein structures in the solution phase using TRXL. Recently, the reaction triggering of TRXL has been expanded to various methods, such as T-jump, pH jump, electron transfer, and the use of photocaged molecules, beyond the conventional direct photoexcitation of proteins using an optical laser pulse. Through these new pump methods, it was possible to reveal the structural dynamics of naturally nonphotoactive proteins, such as the dissociation of insulin oligomers, the folding of PGA and cyt-c, and the dimerization of MsbA-related NBD, which are difficult to investigate with traditional TRXL. Along with these advances, the improvement in time resolution, thanks to the development of XFELs, has widened the application of TRXL to an unprecedented level. Due to such unceasing improvements, it is expected that TRXL will become a typical tool for investigating the reaction dynamics of proteins.

Nevertheless, there is still room for improvement in TRXL. First, a typical TRXL experiment on proteins requires a large amount of a protein sample with a high concentration. In particular, the requirement for such a large amount of the sample poses a critical problem when target proteins have irreversible reactions. If the reaction of a target protein is irreversible, it is difficult to repeat the measurement multiple times on the same sample, thereby requiring an even larger amount of sample for a TRXL experiment. In this regard, an experimental scheme that can overcome this limitation is desirable. A scheme that can reduce the amount of sample consumed will greatly facilitate the wide application of TRXL on difficult-to-express proteins as well as proteins with irreversible reactions. Another limitation to overcome is the time resolutions for stimuli other than direct photoexcitation. For example, the time resolutions of the T-jump TRXL studies have been approximately several nanoseconds. When photocaged molecules are used, the time resolutions of the TRXL studies are typically limited to microseconds due to the time for the photodissociation of the caged molecules. As the structural change in a protein that occurs on a nanosecond or even shorter timescale can be a key process in inducing subsequent structural changes, improving the time resolutions of TRXL using stimuli other than photoexcitation is highly demanded.

## ACKNOWLEDGMENTS

This work was supported by the Institute for Basic Science (Grant No. IBS-R033).

## AUTHOR DECLARATIONS

### Conflict of Interest

The authors have no conflicts to disclose.

## Author Contributions

**Yunbeom Lee:** Conceptualization (supporting); Visualization (equal); Writing – original draft (equal); Writing – review & editing (equal).  
**Hyosub Lee:** Visualization (equal); Writing – original draft (supporting);

Writing – review & editing (supporting). **Hyotcherl Ihee:** Conceptualization (lead); Supervision (lead); Writing – original draft (equal); Writing – review & editing (equal).

## DATA AVAILABILITY

Data sharing is not applicable to this article as no new data were created or analyzed in this study.

## REFERENCES

- <sup>1</sup>Y. Lee, S. Basith, and S. Choi, *J. Med. Chem.* **61**, 1 (2018).
- <sup>2</sup>P. Śledź and A. Caflisch, *Curr. Opin. Struct. Biol.* **48**, 93 (2018).
- <sup>3</sup>C. Cao, H. J. Kang, I. Singh, H. Chen, C. Zhang, W. Ye, B. W. Hayes, J. Liu, R. H. Gumpfer, B. J. Bender, S. T. Slocum, B. E. Krumm, K. Lansu, J. D. McCorvy, W. K. Kroeze, J. G. English, J. F. DiBerto, R. H. J. Olsen, X.-P. Huang, S. Zhang, Y. Liu, K. Kim, J. Karpik, L. Y. Jan, S. N. Abraham, J. Jin, B. K. Shoichet, J. F. Fay, and B. L. Roth, *Nature* **600**, 170 (2021).
- <sup>4</sup>H. Ihee, *Acc. Chem. Res.* **42**, 356 (2009).
- <sup>5</sup>T. K. Kim, J. H. Lee, M. Wulff, Q. Kong, and H. Ihee, *ChemPhysChem* **10**, 1958 (2009).
- <sup>6</sup>J. G. Kim, T. W. Kim, J. Kim, and H. Ihee, *Acc. Chem. Res.* **48**, 2200 (2015).
- <sup>7</sup>J. Kim, K. H. Kim, K. Y. Oang, J. H. Lee, K. Hong, H. Cho, N. Huse, R. W. Schoenlein, T. K. Kim, and H. Ihee, *Chem. Commun.* **52**, 3734 (2016).
- <sup>8</sup>H. Ki, K. Y. Oang, J. Kim, and H. Ihee, *Annu. Rev. Phys. Chem.* **68**, 473 (2017).
- <sup>9</sup>H. S. Cho, F. Schotte, V. Stadnytskyi, and P. Anfinrud, *Curr. Opin. Struct. Biol.* **70**, 99 (2021).
- <sup>10</sup>M. Levantino, Q. Kong, M. Cammarata, D. Khakhulin, F. Schotte, P. Anfinrud, V. Kabanova, H. Ihee, A. Plech, S. Bratos, and M. Wulff, *C. R. Phys.* **22**, 75 (2021).
- <sup>11</sup>H. Ihee, M. Lorenc, T. K. Kim, Q. Y. Kong, M. Cammarata, J. H. Lee, S. Bratos, and M. Wulff, *Science* **309**, 1223 (2005).
- <sup>12</sup>Q. Kong, J. Kim, M. Lorenc, T. K. Kim, H. Ihee, and M. Wulff, *J. Phys. Chem. A* **109**, 10451 (2005).
- <sup>13</sup>J. Davidsson, J. Poulsen, M. Cammarata, P. Georgiou, R. Wouts, G. Katona, F. Jacobson, A. Plech, M. Wulff, G. Nyman, and R. Neutze, *Phys. Rev. Lett.* **94**, 245503 (2005).
- <sup>14</sup>Q. Kong, M. Wulff, J. H. Lee, S. Bratos, and H. Ihee, *J. Am. Chem. Soc.* **129**, 13584 (2007).
- <sup>15</sup>J. H. Lee, T. K. Kim, J. Kim, Q. Kong, M. Cammarata, M. Lorenc, M. Wulff, and H. Ihee, *J. Am. Chem. Soc.* **130**, 5834 (2008).
- <sup>16</sup>J. H. Lee, J. Kim, M. Cammarata, Q. Kong, K. H. Kim, J. Choi, T. K. Kim, M. Wulff, and H. Ihee, *Angew. Chem. Int. Ed.* **47**, 1047 (2008).
- <sup>17</sup>J. Vincent, M. Andersson, M. Eklund, A. B. Wöhri, M. Odelius, E. Malmerberg, Q. Kong, M. Wulff, R. Neutze, and J. Davidsson, *J. Chem. Phys.* **130**, 154502 (2009).
- <sup>18</sup>J. Kim, J. H. Lee, J. Kim, S. Jun, K. H. Kim, T. W. Kim, M. Wulff, and H. Ihee, *J. Phys. Chem. A* **116**, 2713 (2012).
- <sup>19</sup>C. W. Ahn, H. Ki, J. Kim, J. Kim, S. Park, Y. Lee, K. H. Kim, Q. Kong, J. Moon, M. N. Pedersen, M. Wulff, and H. Ihee, *J. Phys. Chem. Lett.* **9**, 647 (2018).
- <sup>20</sup>S. Park, J. Choi, H. Ki, K. H. Kim, K. Y. Oang, H. Roh, J. Kim, S. Nozawa, T. Sato, S-i Adachi, J. Kim, and H. Ihee, *J. Chem. Phys.* **150**, 224201 (2019).
- <sup>21</sup>Q. Kong, D. Khakhulin, I. A. Shkrob, J. H. Lee, X. Zhang, J. Kim, K. H. Kim, J. Jo, J. Kim, J. Kang, V.-T. Pham, G. Jennings, C. Kurtz, R. Spence, L. X. Chen, M. Wulff, and H. Ihee, *Struct. Dyn.* **6**, 064902 (2019).
- <sup>22</sup>M. R. Panman, E. Biasin, O. Berntsson, M. Hermann, S. Niebling, A. J. Hughes, J. Kübel, K. Atkovska, E. Gustavsson, A. Nimrich, A. O. Dohn, M. Laursen, D. B. Zederkof, A. Honarfar, K. Tono, T. Katayama, S. Owada, T. B. van Driel, K. Kjaer, M. M. Nielsen, J. Davidsson, J. Uhlig, K. Haldrup, J. S. Hub, and S. Westenhoff, *Phys. Rev. Lett.* **125**, 226001 (2020).
- <sup>23</sup>H. Kim, J. G. Kim, T. W. Kim, S. J. Lee, S. Nozawa, S-i Adachi, K. Yoon, J. Kim, and H. Ihee, *Chem. Sci.* **12**, 2114 (2021).
- <sup>24</sup>J. Gu, S. Lee, S. Eom, H. Ki, E. H. Choi, Y. Lee, S. Nozawa, S-i Adachi, J. Kim, and H. Ihee, *Int. J. Mol. Sci.* **22**, 9793 (2021).
- <sup>25</sup>T. K. Kim, M. Lorenc, J. H. Lee, M. L. Russo, J. Kim, M. Cammarata, Q. Kong, S. Noel, A. Plech, M. Wulff, and H. Ihee, *Proc. Natl. Acad. Sci. U. S. A.* **103**, 9410 (2006).
- <sup>26</sup>E. H. Choi, D.-S. Ahn, S. Park, C. Kim, C. W. Ahn, S. Kim, M. Choi, C. Yang, T. W. Kim, H. Ki, J. Choi, M. N. Pedersen, M. Wulff, J. Kim, and H. Ihee, *J. Phys. Chem. Lett.* **10**, 1279 (2019).
- <sup>27</sup>D. Leshchev, D. Khakhulin, G. Newby, H. Ki, H. Ihee, and M. Wulff, *J. Chem. Phys.* **151**, 054310 (2019).
- <sup>28</sup>E. H. Choi, J. G. Kim, J. Kim, H. Ki, Y. Lee, S. Lee, K. Yoon, J. Kim, J. Kim, and H. Ihee, *Nat. Commun.* **12**, 4732 (2021).
- <sup>29</sup>R. Neutze, R. Wouts, S. Techert, J. Davidsson, M. Kocsis, A. Kirrander, F. Schotte, and M. Wulff, *Phys. Rev. Lett.* **87**, 195508 (2001).
- <sup>30</sup>S. Bratos, F. Mirloup, R. Vuilleumier, and M. Wulff, *J. Chem. Phys.* **116**, 10615 (2002).
- <sup>31</sup>A. Plech, M. Wulff, S. Bratos, F. Mirloup, R. Vuilleumier, F. Schotte, and P. A. Anfinrud, *Phys. Rev. Lett.* **92**, 125505 (2004).
- <sup>32</sup>M. Wulff, S. Bratos, A. Plech, R. Vuilleumier, F. Mirloup, M. Lorenc, Q. Kong, and H. Ihee, *J. Chem. Phys.* **124**, 034501 (2006).
- <sup>33</sup>Q. Kong, J. H. Lee, M. Lo Russo, T. K. Kim, M. Lorenc, M. Cammarata, S. Bratos, T. Buslaps, V. Honkimaki, H. Ihee, and M. Wulff, *Acta Cryst. A* **66**, 252 (2010).
- <sup>34</sup>J. H. Lee, M. Wulff, S. Bratos, J. Petersen, L. Guerin, J.-C. Leicknam, M. Cammarata, Q. Kong, J. Kim, K. B. Möller, and H. Ihee, *J. Am. Chem. Soc.* **135**, 3255 (2013).
- <sup>35</sup>K. H. Kim, J. H. Lee, J. Kim, S. Nozawa, T. Sato, A. Tomita, K. Ichinagaki, H. Ki, J. Kim, S-i Adachi, and H. Ihee, *Phys. Rev. Lett.* **110**, 165505 (2013).
- <sup>36</sup>K. H. Kim, H. Ki, K. Y. Oang, S. Nozawa, T. Sato, J. Kim, T. K. Kim, J. Kim, S-i Adachi, and H. Ihee, *ChemPhysChem* **14**, 3687 (2013).
- <sup>37</sup>K. H. Kim, H. Ki, J. H. Lee, S. Park, Q. Kong, J. Kim, J. Kim, M. Wulff, and H. Ihee, *Phys. Chem. Chem. Phys.* **17**, 8633 (2015).
- <sup>38</sup>J. Heo, J. G. Kim, E. H. Choi, H. Ki, D.-S. Ahn, J. Kim, S. Lee, and H. Ihee, *Nat. Commun.* **13**, 522 (2022).
- <sup>39</sup>M. Cammarata, M. Levantino, F. Schotte, P. A. Anfinrud, F. Ewald, J. Choi, A. Cupane, M. Wulff, and H. Ihee, *Nat. Methods* **5**, 881 (2008).
- <sup>40</sup>K. Moffat, *Chem. Rev.* **101**, 1569 (2001).
- <sup>41</sup>V. Srajer, T. Teng, T. Ursby, C. Pradervand, Z. Ren, S. Adachi, W. Schildkamp, D. Bourgeois, M. Wulff, and K. Moffat, *Science* **274**, 1726 (1996).
- <sup>42</sup>V. Šrajer, Z. Ren, T.-Y. Teng, M. Schmidt, T. Ursby, D. Bourgeois, C. Pradervand, W. Schildkamp, M. Wulff, and K. Moffat, *Biochemistry* **40**, 13802 (2001).
- <sup>43</sup>D. Bourgeois, B. Vallone, F. Schotte, A. Arcovito, E. Miele Adriana, G. Sciarra, M. Wulff, P. Anfinrud, and M. Brunori, *Proc. Natl. Acad. Sci. U. S. A.* **100**, 8704 (2003).
- <sup>44</sup>F. Schotte, M. Lim, T. A. Jackson, A. V. Smirnov, J. Soman, J. S. Olson, G. N. Phillips, Jr., M. Wulff, and P. A. Anfinrud, *Science* **300**, 1944 (2003).
- <sup>45</sup>G. Hummer, F. Schotte, and A. Anfinrud Philip, *Proc. Natl. Acad. Sci. U. S. A.* **101**, 15330 (2004).
- <sup>46</sup>M. Schmidt, K. Nienhaus, R. Pahl, A. Krasselt, S. Anderson, F. Parak, G. U. Nienhaus, and V. Šrajer, *Proc. Natl. Acad. Sci. U. S. A.* **102**, 11704 (2005).
- <sup>47</sup>R. t Aranda, E. J. Levin, F. Schotte, P. A. Anfinrud, and G. N. Phillips, Jr., *Acta Crystallogr., Sect. D: Struct. Biol.* **62**, 776 (2006).
- <sup>48</sup>D. Bourgeois, B. Vallone, A. Arcovito, G. Sciarra, F. Schotte, A. Anfinrud Philip, and M. Brunori, *Proc. Natl. Acad. Sci. U. S. A.* **103**, 4924 (2006).
- <sup>49</sup>J. E. Knapp, R. Pahl, V. Srajer, and W. E. Royer, Jr., *Proc. Natl. Acad. Sci. U. S. A.* **103**, 7649 (2006).
- <sup>50</sup>J. E. Knapp, R. Pahl, J. Cohen, J. C. Nichols, K. Schulten, Q. H. Gibson, V. Srajer, and W. E. Royer, Jr., *Structure* **17**, 1494 (2009).
- <sup>51</sup>Z. Ren, V. Srajer, J. E. Knapp, and W. E. Royer, Jr., *Proc. Natl. Acad. Sci. U. S. A.* **109**, 107 (2012).
- <sup>52</sup>K. Genick Ulrich, E. O. Borgstahl Gloria, K. Ng, Z. Ren, C. Pradervand, M. Burke Patrick, V. Šrajer, T.-Y. Teng, W. Schildkamp, E. McRee Duncan, K. Moffat, and D. Getzoff Elizabeth, *Science* **275**, 1471 (1997).
- <sup>53</sup>B. Perman, V. Srajer, Z. Ren, T. Teng, C. Pradervand, T. Ursby, D. Bourgeois, F. Schotte, M. Wulff, R. Kort, K. Hellingwerf, and K. Moffat, *Science* **279**, 1946 (1998).
- <sup>54</sup>Z. Ren, B. Perman, V. Srajer, T. Y. Teng, C. Pradervand, D. Bourgeois, F. Schotte, T. Ursby, R. Kort, M. Wulff, and K. Moffat, *Biochemistry* **40**, 13788 (2001).



- <sup>55</sup>S. Rajagopal, M. Schmidt, S. Anderson, H. Ihee, and K. Moffat, *Acta Crystallogr., Sect. D: Struct. Biol.* **60**, 860 (2004).
- <sup>56</sup>H. Ihee, S. Rajagopal, V. Srajer, R. Pahl, S. Anderson, M. Schmidt, F. Schotte, P. A. Anfinrud, M. Wulff, and K. Moffat, *Proc. Natl. Acad. Sci. U. S. A.* **102**, 7145 (2005).
- <sup>57</sup>S. Rajagopal, S. Anderson, V. Srajer, M. Schmidt, R. Pahl, and K. Moffat, *Structure* **13**, 55 (2005).
- <sup>58</sup>F. Schotte, S. Cho Hyun, R. I. Kaila Ville, H. Kamikubo, N. Dashdorj, R. Henry Eric, J. Graber Timothy, R. Henning, M. Wulff, G. Hummer, M. Kataoka, and A. Anfinrud Philip, *Proc. Natl. Acad. Sci. U. S. A.* **109**, 19256 (2012).
- <sup>59</sup>Y. O. Jung, J. H. Lee, J. Kim, M. Schmidt, K. Moffat, V. Srajer, and H. Ihee, *Nat. Chem.* **5**, 212 (2013).
- <sup>60</sup>M. Schmidt, V. Srajer, R. Henning, H. Ihee, N. Purwar, J. Tenboer, and S. Tripathi, *Acta Cryst. D* **69**, 2534 (2013).
- <sup>61</sup>R. H. G. Baxter, N. Ponomarenko, V. Srajer, R. Pahl, K. Moffat, and J. R. Norris, *Proc. Natl. Acad. Sci. U. S. A.* **101**, 5982 (2004).
- <sup>62</sup>A. B. Wöhri, G. Katona, L. C. Johansson, E. Fritz, E. Malmerberg, M. Andersson, J. Vincent, M. Eklund, M. Cammarata, M. Wulff, J. Davidsson, G. Groenhof, and R. Neutze, *Science* **328**, 630 (2010).
- <sup>63</sup>J. Key, V. Srajer, R. Pahl, and K. Moffat, *Biochemistry* **46**, 4706 (2007).
- <sup>64</sup>S. Ahn, K. H. Kim, Y. Kim, J. Kim, and H. Ihee, *J. Phys. Chem. B* **113**, 13131 (2009).
- <sup>65</sup>M. Andersson, E. Malmerberg, S. Westenhoff, G. Katona, M. Cammarata, A. B. Wöhri, L. C. Johansson, F. Ewald, M. Eklund, M. Wulff, J. Davidsson, and R. Neutze, *Structure* **17**, 1265 (2009).
- <sup>66</sup>K. H. Kim, S. Muniyappan, K. Y. Oang, J. G. Kim, S. Nozawa, T. Sato, S-y Koshihara, R. Henning, I. Kosheleva, H. Ki, Y. Kim, T. W. Kim, J. Kim, S-i Adachi, and H. Ihee, *J. Am. Chem. Soc.* **134**, 7001 (2012).
- <sup>67</sup>T. W. Kim, J. H. Lee, J. Choi, K. H. Kim, L. J. van Wilderen, L. Guerin, Y. Kim, Y. O. Jung, C. Yang, J. Kim, M. Wulff, J. J. van Thor, and H. Ihee, *J. Am. Chem. Soc.* **134**, 3145 (2012).
- <sup>68</sup>E. Malmerberg, M. B.-G. P. H. G. Katona, X. Deupi, D. Arnlund, C. Wickstrand, C. Johansson Linda, S. Westenhoff, E. Nazarenko, X. S. G. F. A. Menzel, J. de Grip Willem, and R. Neutze, *Sci. Signaling* **8**, ra26 (2015).
- <sup>69</sup>O. Berntsson, R. P. Diensthuber, M. R. Panman, A. Björling, A. J. Hughes, L. Henry, S. Niebling, G. Newby, M. Liebi, A. Menzel, R. Henning, I. Kosheleva, A. Möglich, and S. Westenhoff, *Structure* **25**, 933 (2017).
- <sup>70</sup>J. M. Friedman, D. L. Rousseau, and M. R. Ondrias, *Annu. Rev. Phys. Chem.* **33**, 471 (1982).
- <sup>71</sup>D. P. Millar, *Curr. Opin. Struct. Biol.* **6**, 637 (1996).
- <sup>72</sup>L. X. Chen, *Annu. Rev. Phys. Chem.* **56**, 221 (2004).
- <sup>73</sup>E. T. J. Nibbering, H. Fidder, and E. Pines, *Annu. Rev. Phys. Chem.* **56**, 337 (2004).
- <sup>74</sup>D. Buhrke and P. Hildebrandt, *Chem. Rev.* **120**, 3577 (2020).
- <sup>75</sup>M. Terazima, *Acc. Chem. Res.* **54**, 2238 (2021).
- <sup>76</sup>J. Kim, K. H. Kim, J. G. Kim, T. W. Kim, Y. Kim, and H. Ihee, *J. Phys. Chem. Lett.* **2**, 350 (2011).
- <sup>77</sup>J. G. Kim, K. H. Kim, K. Y. Oang, T. W. Kim, H. Ki, J. Jo, J. Kim, T. Sato, S. Nozawa, S-i Adachi, and H. Ihee, *J. Phys. B: At., Mol. Opt. Phys.* **48**, 244005 (2015).
- <sup>78</sup>K. Haldrup, G. Levi, E. Biasin, P. Vester, M. G. Laursen, F. Beyer, K. S. Kjær, T. Brandt van Driel, T. Harlang, A. O. Dohn, R. J. Hartsock, S. Nelson, J. M. Glowia, H. T. Lemke, M. Christensen, K. J. Gaffney, N. E. Henriksen, K. B. Møller, and M. M. Nielsen, *Phys. Rev. Lett.* **122**, 063001 (2019).
- <sup>79</sup>H. Ki, S. Choi, J. Kim, E. H. Choi, S. Lee, Y. Lee, K. Yoon, C. W. Ahn, D.-S. Ahn, J. H. Lee, J. Park, I. Eom, M. Kim, S. H. Chun, J. Kim, H. Ihee, and J. Kim, *J. Am. Chem. Soc.* **143**, 14261 (2021).
- <sup>80</sup>M. Wulff, A. Plech, L. Eybert, R. Randler, F. Schotte, and P. Anfinrud, *Faraday Discuss.* **122**, 13 (2003).
- <sup>81</sup>S. Nozawa, S-i Adachi, J-i Takahashi, R. Tazaki, L. Guerin, M. Daimon, A. Tomita, T. Sato, M. Chollet, E. Collet, H. Cailleau, S. Yamamoto, K. Tsuchiya, T. Shioya, H. Sasaki, T. Mori, K. Ichiyangi, H. Sawa, H. Kawata, and S-y Koshihara, *J. Synchrotron Radiat.* **14**, 313 (2007).
- <sup>82</sup>T. Graber, S. Anderson, H. Brewer, Y.-S. Chen, H. S. Cho, N. Dashdorj, R. W. Henning, I. Kosheleva, G. Macha, M. Meron, R. Pahl, Z. Ren, S. Ruan, F. Schotte, V. Srajer, P. J. Viccaro, F. Westferro, P. Anfinrud, and K. Moffat, *J. Synchrotron Radiat.* **18**, 658 (2011).
- <sup>83</sup>T. Ishikawa, H. Aoyagi, T. Asaka, Y. Asano, N. Azumi, T. Bizen, H. Ego, K. Fukami, T. Fukui, Y. Furukawa, S. Goto, H. Hanaki, T. Hara, T. Hasegawa, T. Hatsui, A. Higashiya, T. Hirono, N. Hosoda, M. Ishii, T. Inagaki, Y. Inubushi, T. Itoga, Y. Joti, M. Kago, T. Kameshima, H. Kimura, Y. Kirihaara, A. Kiyomichi, T. Kobayashi, C. Kondo, T. Kudo, H. Maesaka, X. M. Maréchal, T. Masuda, S. Matsubara, T. Matsumoto, T. Matsushita, S. Matsui, M. Nagasono, N. Nariyama, H. Ohashi, T. Ohata, T. Ohshima, S. Ono, Y. Otake, C. Saji, T. Sakurai, T. Sato, K. Sawada, T. Seike, K. Shirasawa, T. Sugimoto, S. Suzuki, S. Takahashi, H. Takebe, K. Takeshita, K. Tamasaku, H. Tanaka, R. Tanaka, T. Tanaka, T. Togashi, K. Togawa, A. Tokuhisa, H. Tomizawa, K. Tono, S. Wu, M. Yabashi, M. Yamaga, A. Yamashita, K. Yanagida, C. Zhang, T. Shintake, H. Kitamura, and N. Kumagai, *Nat. Photonics* **6**, 540 (2012).
- <sup>84</sup>M. Chollet, R. Alonso-Mori, M. Cammarata, D. Damiani, J. Defever, J. T. Delor, Y. Feng, J. M. Glowia, J. B. Langton, S. Nelson, K. Ramsey, A. Robert, M. Sikorski, S. Song, D. Stefanescu, V. Srinivasan, D. Zhu, H. T. Lemke, and D. M. Fritz, *J. Synchrotron Radiat.* **22**, 503 (2015).
- <sup>85</sup>J. Park, I. Eom, T.-H. Kang, S. Rah, K. H. Nam, J. Park, S. Kim, S. Kwon, S. H. Park, K. S. Kim, H. Hyun, S. N. Kim, E. H. Lee, H. Shin, S. Kim, M.-j Kim, H.-J. Shin, D. Ahn, J. Lim, C.-J. Yu, C. Song, H. Kim, D. Y. Noh, H. S. Kang, B. Kim, K.-W. Kim, I. S. Ko, M.-H. Cho, and S. Kim, *Nucl. Instrum. Methods Phys. Res. A* **810**, 74 (2016).
- <sup>86</sup>W. Decking, S. Abeghyan, P. Abramian, A. Abramsky, A. Aguirre, C. Albrecht, P. Alou, M. Altarelli, P. Altmann, K. Amyan, V. Anashin, E. Apostolov, K. Appel, D. Auguste, V. Ayvazyan, S. Baark, F. Babies, N. Baboi, P. Bak, V. Balandin, R. Baldinger, B. Baranasic, S. Barbanotti, O. Belikov, V. Belokurov, L. Belova, V. Belyakov, S. Berry, M. Bertucci, B. Beutner, A. Block, M. Blöcher, T. Böckmann, C. Bohm, M. Böhnert, V. Bondar, E. Bondarchuk, M. Bonezzi, P. Borowiec, C. Bösch, U. Bösenberg, A. Bosotti, R. Böspflug, M. Bousonville, E. Boyd, Y. Bozhko, A. Brand, J. Bransford, S. Briehle, F. Brinker, S. Brinker, R. Brinkmann, S. Brockhauser, O. Brovko, H. Brück, A. Brüdger, L. Butkowski, T. Büttner, J. Calero, E. Castro-Carballo, G. Cattalanotto, J. Charrier, J. Chen, A. Cherepenko, V. Cheskidov, M. Chiodini, A. Chong, S. Choroba, M. Chorowski, D. Churanov, V. Cichalewski, M. Clausen, W. Clement, C. Cloué, J. A. Cobos, N. Coppola, S. Cunis, K. Czuba, M. Czwalińska, B. D'Almagre, J. Dammann, H. Danared, A. de Zubiaurre Wagner, A. Delfs, T. Delfs, F. Dietrich, T. Dietrich, M. Dohlus, M. Dommach, A. Donat, X. Dong, N. Doynikov, M. Dressel, M. Duda, P. Duda, H. Eckoldt, W. Ehsan, J. Eidam, F. Eints, C. Engling, U. Englisch, A. Ermakov, K. Escherich, J. Eschke, E. Saldin, M. Faesing, A. Fallou, M. Felber, M. Fenner, B. Fernandes, J. M. Fernández, S. Feuker, K. Filippakopoulos, K. Floettmann, V. Fogel, M. Fontaine, A. Francés, I. F. Martin, W. Freund, T. Freyermuth, M. Friedland, L. Fröhlich, M. Fuseti, J. Fydrich, A. Gallas, O. García, L. Garcia-Tabares, G. Geloni, N. Gerasimova, C. Gerth, P. Geßler, V. Gharibyan, M. Gloor, J. Glowinkowski, A. Goessell, Z. Gołbiewski, N. Golubeva, W. Grabowski, W. Graeff, A. Grebentsov, M. Grecki, T. Grevsmuehl, M. Gross, U. Grosse-Wortmann, J. Grünert, S. Grunewald, P. Grzegory, G. Feng, H. Guler, G. Gusev, J. L. Gutierrez, L. Hagge, M. Hamberg, R. Hanneken, E. Harms, I. Hartl, A. Hauberg, S. Hauf, J. Hauschildt, J. Hauser, J. Havlicek, A. Hedqvist, N. Heidbrook, F. Hellberg, D. Henning, O. Hensler, T. Hermann, A. Hidvégi, M. Hierholzer, H. Hintz, F. Hoffmann, M. Hoffmann, M. Hoffmann, Y. Holler, M. Hüning, A. Ignatenko, M. Ilchen, A. Iluk, J. Iversen, J. Iversen, M. Izquierdo, L. Jachmann, N. Jardon, U. Jastrow, K. Jensch, J. Jensen, M. Jeżabek, H. Jidda, H. Jin, N. Johansson, R. Jonas, W. Kaabi, D. Kaefler, R. Kammering, H. Kapitza, S. Karabekyan, S. Karstensen, K. Kasprzak, V. Katalev, D. Keese, B. Keil, M. Kholopov, M. Killenberger, B. Kitaev, Y. Klimchenko, R. Klos, L. Knebel, A. Koch, M. Koepke, S. Köhler, W. Köhler, N. Kohlstrunk, Z. Konopkova, A. Konstantinov, W. Kook, W. Koprek, M. Körfer, O. Korth, A. Kosarev, K. Kosiński, D. Kostin, Y. Kot, A. Kotarba, T. Kozak, V. Kozak, R. Kramert, M. Krasilnikov, A. Krasnov, B. Krause, L. Kravchuk, O. Krebs, R. Kretschmer, J. Kreutzkamp, O. Kröplin, K. Krzysik, G. Kube, H. Kuehn, N. Kujala, V. Kulikov, V. Kuzminych, D. L. Civita, M. Lacroix, T. Lamb, A. Lancetov, M. Larsson, D. L. Pinvidic, S. Lederer, T. Lensch, D. Lenz, A. Leuschner, F. Levenhagen, Y. Li, J. Liebing, L. Lilje, T. Limberg, D. Lipka, B. List, J. Liu, S. Liu, B. Lorbeer, J. Lorkiewicz, H. H. Lu, F. Ludwig, K. Machau, W. Maciocha, C. Madec, C. Magueur,

- C. Maiano, I. Maksimova, K. Malcher, T. Maltezopoulos, E. Mamoshkina, B. Manschwetus, F. Marcellini, G. Marinkovic, T. Martinez, H. Martirosyan, W. Maschmann, M. Maslov, A. Matheisen, U. Mavric, J. Meißner, K. Meissner, M. Messerschmidt, N. Meyners, G. Michalski, P. Michelato, N. Mildner, M. Moe, F. Moglia, C. Mohr, S. Mohr, W. Möller, M. Mommerz, L. Monaco, C. Montiel, M. Moretti, I. Morozov, P. Morozov, and D. Mross, *Nat. Photonics* **14**, 391 (2020).
- <sup>87</sup>E. Prat, R. Abela, M. Aiba, A. Alarcon, J. Alex, Y. Arbelo, C. Arrell, V. Arsov, C. Bacellar, C. Beard, P. Beaud, S. Bettoni, R. Biffiger, M. Bopp, H.-H. Braun, M. Calvi, A. Cassar, T. Celcer, M. Chergui, P. Chevtsov, C. Cirelli, A. Citterio, P. Craievich, M. C. Divall, A. Dax, M. Dehler, Y. Deng, A. Dietrich, P. Dijkstra, R. Dinapoli, S. Dordevic, S. Ebner, D. Engeler, C. Erny, V. Esposito, E. Ferrari, U. Flechsig, R. Follath, F. Frei, R. Ganter, T. Garvey, Z. Geng, A. Gobbo, C. Gough, A. Hauff, C. P. Hauri, N. Hiller, S. Hunziker, M. Huppert, G. Ingold, R. Ischebeck, M. Janusch, P. J. M. Johnson, S. L. Johnson, P. Juranić, M. Jurcevic, B. Kaiser, R. Kalt, B. Keil, D. Kiselev, C. Kittel, G. Knopp, W. Koprek, M. Laznovsky, H. T. Lemke, D. L. Sancho, F. Löh, A. Malyzhenkov, G. F. Mancini, R. Mankowsky, F. Marcellini, G. Marinkovic, I. Martiel, F. Märki, C. J. Milne, A. Mozzanica, K. Nass, G. L. Orlandi, C. O. Loch, M. Paralevic, B. Patterson, D. Patthey, B. Pedrini, M. Pedrozzi, C. Pradervand, P. Radi, J.-Y. Ragui, J. Redford, J. Rehanek, S. Reiche, L. Rivkin, A. Romann, L. Sala, M. Sander, T. Schietinger, T. Schilcher, V. Schlott, T. Schmidt, M. Seidel, M. Stadler, L. Stingelin, C. Svetina, D. M. Treyer, A. Trisorio, C. Vicario, D. Voulou, A. Wrulich, S. Zerdane, and E. Zimoch, *Nat. Photonics* **14**, 748 (2020).
- <sup>88</sup>E. H. Choi, Y. Lee, J. Heo, and H. Ihee, *Chem. Sci.* **13**, 8457 (2022).
- <sup>89</sup>D. Svergun, C. Barberato, and M. H. J. Koch, *J. Appl. Crystallogr.* **28**, 768 (1995).
- <sup>90</sup>D. Schneidman-Duhovny, M. Hammel, J. Tainer, and A. Sali, *Biophys. J.* **105**, 962 (2013).
- <sup>91</sup>K. Y. Oang, J. G. Kim, C. Yang, T. W. Kim, Y. Kim, K. H. Kim, J. Kim, and H. Ihee, *J. Phys. Chem. Lett.* **5**, 804 (2014).
- <sup>92</sup>K. Y. Oang, C. Yang, S. Muniyappan, J. Kim, and H. Ihee, *Struct. Dyn.* **4**, 044013 (2017).
- <sup>93</sup>D. Svergun, *J. Appl. Crystallogr.* **25**, 495 (1992).
- <sup>94</sup>D. I. Svergun, *Biophys. J.* **76**, 2879 (1999).
- <sup>95</sup>D. J. Hsu, D. Leshchev, I. Kosheleva, K. L. Kohlstedt, and L. X. Chen, *J. Chem. Phys.* **154**, 105101 (2021).
- <sup>96</sup>W. A. Eaton, E. R. Henry, J. Hofrichter, S. Bettati, C. Viappiani, and A. Mozzarelli, *IUBMB Life* **59**, 586 (2007).
- <sup>97</sup>J. Monod, J. Wyman, and J.-P. Changeux, *J. Mol. Biol.* **12**, 88 (1965).
- <sup>98</sup>M. Brunori, *Trends Biochem. Sci.* **24**, 158 (1999).
- <sup>99</sup>M. F. Perutz, *Nature* **228**, 726 (1970).
- <sup>100</sup>C. A. Sawicki and Q. H. Gibson, *J. Biol. Chem.* **251**, 1533 (1976).
- <sup>101</sup>J. Hofrichter, J. H. Sommer, E. R. Henry, and W. A. Eaton, *Proc. Natl. Acad. Sci. U. S. A.* **80**, 2235 (1983).
- <sup>102</sup>E. W. Findsen, J. M. Friedman, M. R. Ondrias, and S. R. Simon, *Science* **229**, 661 (1985).
- <sup>103</sup>J. M. Friedman, T. W. Scott, G. J. Fisanick, S. R. Simon, E. W. Findsen, M. R. Ondrias, and V. W. MacDonald, *Science* **229**, 187 (1985).
- <sup>104</sup>J. Hofrichter, E. R. Henry, J. H. Sommer, R. Deutsch, M. Ikeda-Saito, T. Yonetani, and W. A. Eaton, *Biochemistry* **24**, 2667 (1985).
- <sup>105</sup>V. Jayaraman, K. R. Rodgers, I. Mukerji, and T. G. Spiro, *Science* **269**, 1843 (1995).
- <sup>106</sup>S. C. Björling, R. A. Goldbeck, S. J. Paquette, S. J. Milder, and D. S. Klinger, *Biochemistry* **35**, 8619 (1996).
- <sup>107</sup>R. A. Goldbeck, R. M. Esquerre, and D. S. Klinger, *J. Am. Chem. Soc.* **124**, 7646 (2002).
- <sup>108</sup>G. Balakrishnan, M. A. Case, A. Pevsner, X. Zhao, C. Tengroth, G. L. McLendon, and T. G. Spiro, *J. Mol. Biol.* **340**, 843 (2004).
- <sup>109</sup>M. Cammarata, M. Levantino, M. Wulff, and A. Cupane, *J. Mol. Biol.* **400**, 951 (2010).
- <sup>110</sup>M. Levantino, A. Spilotros, M. Cammarata, G. Schirò, C. Ardiccioni, B. Vallone, M. Brunori, and A. Cupane, *Proc. Natl. Acad. Sci. U. S. A.* **109**, 14894 (2012).
- <sup>111</sup>A. Spilotros, M. Levantino, G. Schirò, M. Cammarata, M. Wulff, and A. Cupane, *Soft Matter* **8**, 6434 (2012).
- <sup>112</sup>B. Shaanan, *J. Mol. Biol.* **171**, 31 (1983).
- <sup>113</sup>M. M. Silva, P. H. Rogers, and A. Arnone, *J. Biol. Chem.* **267**, 17248 (1992).
- <sup>114</sup>G. S. Kachalova, A. N. Popov, and H. D. Bartunik, *Science* **284**, 473 (1999).
- <sup>115</sup>V. Guallar, A. A. Jarzecki, R. A. Friesner, and T. G. Spiro, *J. Am. Chem. Soc.* **128**, 5427 (2006).
- <sup>116</sup>A. E. Miele, S. Santanché, C. Travaglini-Allocatelli, B. Vallone, M. Brunori, and A. Bellelli, *J. Mol. Biol.* **290**, 515 (1999).
- <sup>117</sup>A. E. Miele, F. Draghi, A. Arcovito, A. Bellelli, M. Brunori, C. Travaglini-Allocatelli, and B. Vallone, *Biochemistry* **40**, 14449 (2001).
- <sup>118</sup>K. Chu, R. M. Ernst, H. Frauenfelder, J. R. Mourant, G. U. Nienhaus, and R. Philipp, *Phys. Rev. Lett.* **74**, 2607 (1995).
- <sup>119</sup>E. E. Scott and Q. H. Gibson, *Biochemistry* **36**, 11909 (1997).
- <sup>120</sup>G. D. Goodno, V. Astinov, and R. J. D. Miller, *J. Phys. Chem. A* **103**, 10630 (1999).
- <sup>121</sup>K. Chu, J. Vojtechovsky, B. H. McMahon, R. M. Sweet, J. Berendzen, and I. Schlichting, *Nature* **403**, 921 (2000).
- <sup>122</sup>Y. Nishihara, M. Sakakura, Y. Kimura, and M. Terazima, *J. Am. Chem. Soc.* **126**, 11877 (2004).
- <sup>123</sup>R. Elber and M. Karplus, *Science* **235**, 318 (1987).
- <sup>124</sup>H. S. Cho, N. Dashdorj, F. Schotte, T. Graber, R. Henning, and P. Anfinrud, *Proc. Natl. Acad. Sci. U. S. A.* **107**, 7281 (2010).
- <sup>125</sup>K. H. Kim, K. Y. Oang, J. Kim, J. H. Lee, Y. Kim, and H. Ihee, *Chem. Commun.* **47**, 289 (2011).
- <sup>126</sup>K. Y. Oang, K. H. Kim, J. Jo, Y. Kim, J. G. Kim, T. W. Kim, S. Jun, J. Kim, and H. Ihee, *Chem. Phys.* **442**, 137 (2014).
- <sup>127</sup>M. Levantino, G. Schirò, H. T. Lemke, G. Cottone, J. M. Glowina, D. Zhu, M. Chollet, H. Ihee, A. Cupane, and M. Cammarata, *Nat. Commun.* **6**, 6772 (2015).
- <sup>128</sup>M. L. Shelby, A. Wildman, D. Hayes, M. W. Mara, P. J. LeStrange, M. Cammarata, L. Balducci, M. Artamonov, H. T. Lemke, D. Zhu, T. Seideman, B. M. Hoffman, X. Li, and L. X. Chen, *Proc. Natl. Acad. Sci. U. S. A.* **118**, e2018966118 (2021).
- <sup>129</sup>M. Lim, T. A. Jackson, and P. A. Anfinrud, *J. Chem. Phys.* **102**, 4355 (1995).
- <sup>130</sup>K. Nienhaus, J. S. Olson, S. Franzen, and G. U. Nienhaus, *J. Am. Chem. Soc.* **127**, 40 (2005).
- <sup>131</sup>A. Sato, Y. Gao, T. Kitagawa, and Y. Mizutani, *Proc. Natl. Acad. Sci. U. S. A.* **104**, 9627 (2007).
- <sup>132</sup>L. U. L. Brinkmann and J. S. Hub, *Proc. Natl. Acad. Sci. U. S. A.* **113**, 10565 (2016).
- <sup>133</sup>Y. Lee, J. G. Kim, S. J. Lee, S. Muniyappan, T. W. Kim, H. Ki, H. Kim, J. Jo, S. R. Yun, H. Lee, K. W. Lee, S. O. Kim, M. Cammarata, and H. Ihee, *Nat. Commun.* **12**, 3677 (2021).
- <sup>134</sup>W. E. H. Royer and W. A. E. Chiancone, *Science* **249**, 518 (1990).
- <sup>135</sup>E. Chiancone, P. Vecchini, D. Verzili, F. Ascoli, and E. Antonini, *J. Mol. Biol.* **152**, 577 (1981).
- <sup>136</sup>J. E. Knapp and W. E. Royer, *Biochemistry* **42**, 4640 (2003).
- <sup>137</sup>E. Antonini, F. Ascoli, M. Brunori, E. Chiancone, D. Verzili, R. J. Morris, and Q. H. Gibson, *J. Biol. Chem.* **259**, 6730 (1984).
- <sup>138</sup>D. L. Rousseau, S. Song, J. M. Friedman, A. Boffi, and E. Chiancone, *J. Biol. Chem.* **268**, 5719 (1993).
- <sup>139</sup>J. Huang, M. Leone, A. Boffi, J. M. Friedman, and E. Chiancone, *Biophys. J.* **70**, 2924 (1996).
- <sup>140</sup>J. E. Knapp, M. A. Bonham, Q. H. Gibson, J. C. Nichols, and W. E. Royer, *Biochemistry* **44**, 14419 (2005).
- <sup>141</sup>W. E. Royer, A. Pardanani, Q. H. Gibson, E. S. Peterson, and J. M. Friedman, *Proc. Natl. Acad. Sci. U. S. A.* **93**, 14526 (1996).
- <sup>142</sup>J. G. Kim, S. Muniyappan, K. Y. Oang, T. W. Kim, C. Yang, K. H. Kim, J. Kim, and H. Ihee, *Struct. Dyn.* **3**, 023610 (2016).
- <sup>143</sup>J. E. Knapp, Q. H. Gibson, L. Cushing, and W. E. Royer, *Biochemistry* **40**, 14795 (2001).
- <sup>144</sup>H. Kim, J. G. Kim, S. Muniyappan, T. W. Kim, S. J. Lee, and H. Ihee, *J. Phys. Chem. B* **124**, 1550 (2020).
- <sup>145</sup>P. Ceci, L. Giangiacomo, A. Boffi, and E. Chiancone, *J. Biol. Chem.* **277**, 6929 (2002).
- <sup>146</sup>M. Choi, J. G. Kim, S. Muniyappan, H. Kim, T. W. Kim, Y. Lee, S. J. Lee, S. O. Kim, and H. Ihee, *Chem. Sci.* **12**, 8207 (2021).
- <sup>147</sup>G. W. Bushnell, G. V. Louie, and G. D. Brayer, *J. Mol. Biol.* **214**, 585 (1990).

- <sup>148</sup>V. E. Kagan, V. A. Tyurin, J. Jiang, Y. Y. Tyurina, V. B. Ritov, A. A. Amoscato, A. N. Osipov, N. A. Belikova, A. A. Kapralov, V. Kini, I. I. Vlasova, Q. Zhao, M. Zou, P. Di, D. A. Svistunenko, I. V. Kurnikov, and G. G. Borisenko, *Nat. Chem. Biol.* **1**, 223 (2005).
- <sup>149</sup>L. J. McClelland, H. B. B. Steele, F. G. Whitby, T.-C. Mou, D. Holley, J. B. A. Ross, S. R. Sprang, and B. E. Bowler, *J. Am. Chem. Soc.* **138**, 16770 (2016).
- <sup>150</sup>C. M. Jones, E. R. Henry, Y. Hu, C. K. Chan, S. D. Luck, A. Bhuyan, H. Roder, J. Hofrichter, and W. A. Eaton, *Proc. Natl. Acad. Sci. U. S. A.* **90**, 11860 (1993).
- <sup>151</sup>J. R. Telford, F. A. Tezcan, H. B. Gray, and J. R. Winkler, *Biochemistry* **38**, 1944 (1999).
- <sup>152</sup>S. J. Hagen, R. F. Latypov, D. A. Dolgikh, and H. Roder, *Biochemistry* **41**, 1372 (2002).
- <sup>153</sup>S. Oellerich, H. Wackerbarth, and P. Hildebrandt, *J. Phys. Chem. B* **106**, 6566 (2002).
- <sup>154</sup>E. Chen, M. J. Wood, A. L. Fink, and D. S. Kliger, *Biochemistry* **37**, 5589 (1998).
- <sup>155</sup>R. A. Goldbeck, Y. G. Thomas, E. Chen, R. M. Esquerra, and D. S. Kliger, *Proc. Natl. Acad. Sci. U. S. A.* **96**, 2782 (1999).
- <sup>156</sup>J. Choi, C. Yang, J. Kim, and H. Ihee, *J. Phys. Chem. B* **115**, 3127 (2011).
- <sup>157</sup>T. W. Kim, J. G. Kim, C. Yang, H. Ki, J. Jo, and H. Ihee, *Bull. Korean Chem. Soc.* **35**, 695 (2014).
- <sup>158</sup>D. J. Hsu, D. Leshchev, D. Rimmerman, J. Hong, M. S. Kelley, I. Kosheleva, X. Zhang, and L. X. Chen, *Chem. Sci.* **10**, 9788 (2019).
- <sup>159</sup>M. E. Reinhard, M. W. Mara, T. Kroll, H. Lim, R. G. Hadt, R. Alonso-Mori, M. Chollet, J. M. Glowina, S. Nelson, D. Sokaras, K. Kunnus, T. B. v Driel, R. W. Hartsock, K. S. Kjaer, C. Weninger, E. Biasin, L. B. Gee, K. O. Hodgson, B. Hedman, U. Bergmann, E. I. Solomon, and K. J. Gaffney, *Nat. Commun.* **12**, 1086 (2021).
- <sup>160</sup>W. L. Butler, K. H. Norris, H. W. Siegelman, and S. B. Hendricks, *Proc. Natl. Acad. Sci. U. S. A.* **45**, 1703 (1959).
- <sup>161</sup>D. M. Kehoe and A. R. Grossman, *Science* **273**, 1409 (1996).
- <sup>162</sup>N. C. Rockwell, Y.-S. Su, and J. C. Lagarias, *Annu. Rev. Plant Biol.* **57**, 837 (2006).
- <sup>163</sup>M. J. Burke, D. C. Pratt, and A. Moscovitz, *Biochemistry* **11**, 4025 (1972).
- <sup>164</sup>D. L. Farrens, R. E. Holt, B. N. Rospendowski, P. S. Song, and T. M. Cotton, *J. Am. Chem. Soc.* **111**, 9162 (1989).
- <sup>165</sup>B. Karniol and D. Vierstra Richard, *Proc. Natl. Acad. Sci. U. S. A.* **100**, 2807 (2003).
- <sup>166</sup>X. Yang, E. Stojković, W. Ozarowski, J. Kuk, E. Davydova, and K. Moffat, *Struct.* **23**, 1179 (2015).
- <sup>167</sup>T. Lamparter, P. Xue, A. Elkurdi, G. Kaeser, L. Sauthof, P. Scheerer, and N. Krauß, *Front. Plant Sci.* **12**, 642801 (2021).
- <sup>168</sup>H. Takala, A. Björling, O. Berntsson, H. Lehtivuori, S. Niebling, M. Hoernke, I. Kosheleva, R. Henning, A. Menzel, J. A. Ihalainen, and S. Westenhoff, *Nature* **509**, 245 (2014).
- <sup>169</sup>H. Takala, S. Niebling, O. Berntsson, A. Björling, H. Lehtivuori, H. Häkkinen, M. Panman, E. Gustavsson, M. Hoernke, G. Newby, F. Zontone, M. Wulff, A. Menzel, J. A. Ihalainen, and S. Westenhoff, *Struct. Dyn.* **3**, 054701 (2016).
- <sup>170</sup>A. Björling, O. Berntsson, H. Lehtivuori, H. Takala, J. Hughes Ashley, M. Panman, M. Hoernke, S. Niebling, L. Henry, R. Henning, I. Kosheleva, V. Chukharev, V. Tkachenko Nikolai, A. Menzel, G. Newby, D. Khakhulin, M. Wulff, A. Ihalainen Janne, and S. Westenhoff, *Sci. Adv.* **2**, e1600920 (2016).
- <sup>171</sup>D. J. Heyes, S. J. O. Hardman, M. N. Pedersen, J. Woodhouse, E. De La Mora, M. Wulff, M. Weik, M. Cammarata, N. S. Scrutton, and G. Schirò, *Commun. Biol.* **2**, 1 (2019).
- <sup>172</sup>S. J. Lee, T. W. Kim, J. G. Kim, C. Yang, S. R. Yun, C. Kim, Z. Ren, I. Kumarapperuma, J. Kuk, K. Moffat, X. Yang, and H. Ihee, *Sci. Adv.* **8**, eabm6278 (2022).
- <sup>173</sup>E. Consiglieri, A. Gutt, W. Gärtner, L. Schubert, C. Viappiani, S. Abbruzzetti, and A. Losi, *Photochem. Photobiol. Sci.* **18**, 2484 (2019).
- <sup>174</sup>D. Oesterhelt, *Curr. Opin. Struct. Biol.* **8**, 489 (1998).
- <sup>175</sup>O. Bějá, L. Aravind, V. Koonin Eugene, T. Suzuki Marcelino, A. Hadd, P. Nguyen Linh, B. Jovanovich Stevan, M. G. Christian, A. Feldman Robert, L. Spudich John, N. Spudich Elena, and F. DeLong Edward, *Science* **289**, 1902 (2000).
- <sup>176</sup>K. Palczewski, *Annu. Rev. Biochem.* **75**, 743 (2006).
- <sup>177</sup>S. O. Smith, *Annu. Rev. Biophys.* **39**, 309 (2010).
- <sup>178</sup>W. Kühlbrandt, *Nature* **406**, 569 (2000).
- <sup>179</sup>T. Yoshizawa and G. Wald, *Nature* **197**, 1279 (1963).
- <sup>180</sup>K. Gerwert, G. Souvignier, and B. Hess, *Proc. Natl. Acad. Sci. U. S. A.* **87**, 9774 (1990).
- <sup>181</sup>R. Rammelsberg, B. Heßling, H. Chorogiewski, and K. Gerwert, *Appl. Spectrosc.* **51**, 558 (1997).
- <sup>182</sup>S. Subramaniam and R. Henderson, *Nature* **406**, 653 (2000).
- <sup>183</sup>K. Edman, A. Royant, G. Larsson, F. Jacobson, T. Taylor, D. van der Spoel, E. M. Landau, E. Pebay-Peyroula, and R. Neutze, *J. Biol. Chem.* **279**, 2147 (2004).
- <sup>184</sup>J. K. Lanyi and B. Schobert, *J. Mol. Biol.* **328**, 439 (2003).
- <sup>185</sup>E. Malmerberg, Z. Omran, J. Hub, X. Li, G. Katona, S. Westenhoff, L. Johansson, M. Andersson, M. Cammarata, M. Wulff, D. van der Spoel, J. Davidsson, A. Specht, and R. Neutze, *Biophys. J.* **101**, 1345 (2011).
- <sup>186</sup>S. Westenhoff, E. Malmerberg, D. Arnlund, L. Johansson, E. Nazarenko, M. Cammarata, J. Davidsson, V. Chaptal, J. Abramson, G. Katona, A. Menzel, and R. Neutze, *Nat. Methods* **7**, 775 (2010).
- <sup>187</sup>D. Fotiadis, Y. Liang, S. Filipek, D. A. Saperstein, A. Engel, and K. Palczewski, *Nature* **421**, 127 (2003).
- <sup>188</sup>Y. Liang, D. Fotiadis, S. Filipek, D. A. Saperstein, K. Palczewski, and A. Engel, *J. Biol. Chem.* **278**, 21655 (2003).
- <sup>189</sup>W. W. Sprenger, W. D. Hoff, J. P. Armitage, and K. J. Hellingwerf, *J. Bacteriol.* **175**, 3096 (1993).
- <sup>190</sup>M. A. Cusanovich and T. E. Meyer, *Biochemistry* **42**, 4759 (2003).
- <sup>191</sup>K. J. Hellingwerf, J. Hendriks, and T. Gensch, *J. Phys. Chem. A* **107**, 1082 (2003).
- <sup>192</sup>W. D. Hoff, A. Xie, I. H. M. Van Stokkum, X.-j. Tang, J. Gural, A. R. Kroon, and K. J. Hellingwerf, *Biochemistry* **38**, 1009 (1999).
- <sup>193</sup>A. Xie, L. Kelemen, J. Hendriks, B. J. White, K. J. Hellingwerf, and W. D. Hoff, *Biochemistry* **40**, 1510 (2001).
- <sup>194</sup>J. Sasaki, M. Kumauchi, N. Hamada, T. Oka, and F. Tokunaga, *Biochemistry* **41**, 1915 (2002).
- <sup>195</sup>P. L. Ramachandran, J. E. Lovett, P. J. Carl, M. Cammarata, J. H. Lee, Y. O. Jung, H. Ihee, C. R. Timmel, and J. J. van Thor, *J. Am. Chem. Soc.* **133**, 9395 (2011).
- <sup>196</sup>H. S. Cho, F. Schotte, N. Dashdorj, J. Kyndt, R. Henning, and P. A. Anfirud, *J. Am. Chem. Soc.* **138**, 8815 (2016).
- <sup>197</sup>T. W. Kim, C. Yang, Y. Kim, J. G. Kim, J. Kim, Y. O. Jung, S. Jun, S. J. Lee, S. Park, I. Kosheleva, R. Henning, J. J. van Thor, and H. Ihee, *Phys. Chem. Chem. Phys.* **18**, 8911 (2016).
- <sup>198</sup>Y. Imamoto, K. i Mihara, O. Hisatomi, M. Kataoka, F. Tokunaga, N. Bojkova, and K. Yoshihara, *J. Biol. Chem.* **272**, 12905 (1997).
- <sup>199</sup>J. Hendriks, W. D. Hoff, W. Crielaard, and K. J. Hellingwerf, *J. Biol. Chem.* **274**, 17655 (1999).
- <sup>200</sup>S. J. Lee, Y. Kim, T. W. Kim, C. Yang, K. Thamilselvan, H. Jeong, J. Hyun, and H. Ihee, *Cell Rep. Phys. Sci.* **2**, 100512 (2021).
- <sup>201</sup>J. T. M. Kennis, S. Crosson, M. Gauden, I. H. M. van Stokkum, K. Moffat, and R. van Grondelle, *Biochemistry* **42**, 3385 (2003).
- <sup>202</sup>T. E. Swartz, S. B. Corchnoy, J. M. Christie, J. W. Lewis, I. Szundi, W. R. Briggs, and R. A. Bogomolni, *J. Biol. Chem.* **276**, 36493 (2001).
- <sup>203</sup>S. Crosson, S. Rajagopal, and K. Moffat, *Biochemistry* **42**, 2 (2003).
- <sup>204</sup>M. Salomon, J. M. Christie, E. Knieb, U. Lempert, and W. R. Briggs, *Biochemistry* **39**, 9401 (2000).
- <sup>205</sup>P. Ballario, P. Vittorioso, A. Magrelli, C. Talora, A. Cabibbo, and G. Macino, *EMBO J.* **15**, 1650 (1996).
- <sup>206</sup>M. Ávila-Pérez, K. J. Hellingwerf, and R. Kort, *J. Bacteriol.* **188**, 6411 (2006).
- <sup>207</sup>O. Berntsson, R. P. Diensthuber, M. R. Panman, A. Björling, E. Gustavsson, M. Hoernke, A. J. Hughes, L. Henry, S. Niebling, H. Takala, J. A. Ihalainen, G. Newby, S. Kerruth, J. Heberle, M. Liebi, A. Menzel, R. Henning, I. Kosheleva, A. Möglich, and S. Westenhoff, *Nat. Commun.* **8**, 284 (2017).
- <sup>208</sup>A. Losi, E. Polverini, B. Quest, and W. Gärtner, *Biophys. J.* **82**, 2627 (2002).
- <sup>209</sup>K. Huang and F. Beck Christoph, *Proc. Natl. Acad. Sci. U. S. A.* **100**, 6269 (2003).
- <sup>210</sup>C.-S. Im, S. Eberhard, K. Huang, C. F. Beck, and A. R. Grossman, *Plant J.* **48**, 1 (2006).
- <sup>211</sup>L. Henry, O. Berntsson, M. R. Panman, A. Cellini, A. J. Hughes, I. Kosheleva, R. Henning, and S. Westenhoff, *Biochemistry* **59**, 3206 (2020).



- <sup>212</sup>J. M. Christie, T. E. Swartz, R. A. Bogomolni, and W. R. Briggs, *Plant J.* **32**, 205 (2002).
- <sup>213</sup>T. Kagawa, M. Kasahara, T. Abe, S. Yoshida, and M. Wada, *Plant Cell Physiol.* **45**, 416 (2004).
- <sup>214</sup>M. Nakasako, T. Iwata, D. Matsuoka, and S. Tokutomi, *Biochemistry* **43**, 14881 (2004).
- <sup>215</sup>P. Emery, W. V. So, M. Kaneko, J. C. Hall, and M. Rosbash, *Cell* **95**, 669 (1998).
- <sup>216</sup>R. Stanewsky, M. Kaneko, P. Emery, B. Beretta, K. Wager-Smith, S. A. Kay, M. Rosbash, and J. C. Hall, *Cell* **95**, 681 (1998).
- <sup>217</sup>T. Ritz, S. Adem, and K. Schulten, *Biophys. J.* **78**, 707 (2000).
- <sup>218</sup>I. Chaves, R. Pokorny, M. Byrdin, N. Hoang, T. Ritz, K. Brettel, L.-O. Essen, G. T. J. van der Horst, A. Batschauer, and M. Ahmad, *Annu. Rev. Plant Biol.* **62**, 335 (2011).
- <sup>219</sup>O. Berntsson, R. Rodriguez, L. Henry, R. Panman Matthijs, J. Hughes Ashley, C. Einholz, S. Weber, A. Ihalainen Janne, R. Henning, I. Kosheleva, E. Schleicher, and S. Westenhoff, *Sci. Adv.* **5**, eaaw1531 (2019).
- <sup>220</sup>A. Busza, M. Emery-Le, M. Rosbash, and P. Emery, *Science* **304**, 1503 (2004).
- <sup>221</sup>N. Peschel, S. Veleri, and R. Stanewsky, *Proc. Natl. Acad. Sci. U. S. A.* **103**, 17313 (2006).
- <sup>222</sup>N. Peschel, K. F. Chen, G. Szabo, and R. Stanewsky, *Curr. Biol.* **19**, 241 (2009).
- <sup>223</sup>A. Ganguly, C. C. Manahan, D. Top, E. F. Yee, C. Lin, M. W. Young, W. Thiel, and B. R. Crane, *Proc. Natl. Acad. Sci. U. S. A.* **113**, 10073 (2016).
- <sup>224</sup>D. Arnlund, L. C. Johansson, C. Wickstrand, A. Barty, G. J. Williams, E. Malmerberg, J. Davidsson, D. Milathianaki, D. P. DePonte, R. L. Shoeman, D. Wang, D. James, G. Katona, S. Westenhoff, T. A. White, A. Aquila, K. Bari, P. Berntsen, M. Bogan, T. B. van Driel, R. B. Doak, K. S. Kjær, M. Frank, R. Fromme, I. Grotjohann, R. Henning, M. S. Hunter, R. A. Kirian, I. Kosheleva, C. Kupitz, M. Liang, A. V. Martin, M. M. Nielsen, M. Messerschmidt, M. M. Seibert, J. Sjöhamn, F. Stellato, U. Weierstall, N. A. Zatsepin, J. C. H. Spence, P. Fromme, I. Schlichting, S. Boutet, G. Groenhof, H. N. Chapman, and R. Neutze, *Nat. Methods* **11**, 923 (2014).
- <sup>225</sup>E. N. Baker, T. L. Blundell, J. F. Cutfield, E. J. Dodson, G. G. Dodson, D. M. C. Hodgkin, R. E. Hubbard, N. W. Isaacs, C. D. Reynolds, K. Sakabe, N. Sakabe, and N. M. Vijayan, *Philos. Trans. R. Soc. London B* **319**, 369 (1988).
- <sup>226</sup>T. Blundell, G. Dodson, D. Hodgkin, and D. Mercola, *Adv. Protein Chem.* **26**, 279 (1972).
- <sup>227</sup>L. Nielsen, R. Khurana, A. Coats, S. Frokjaer, J. Brange, S. Vyas, V. N. Uversky, and A. L. Fink, *Biochemistry* **40**, 6036 (2001).
- <sup>228</sup>Z. Ganim, K. C. Jones, and A. Tokmakoff, *Phys. Chem. Chem. Phys.* **12**, 3579 (2010).
- <sup>229</sup>D. Rimmerman, D. Leshchev, D. J. Hsu, J. Hong, I. Kosheleva, and L. X. Chen, *J. Phys. Chem. Lett.* **8**, 4413 (2017).
- <sup>230</sup>D. Rimmerman, D. Leshchev, D. J. Hsu, J. Hong, B. Abraham, I. Kosheleva, R. Henning, and L. X. Chen, *Photochem. Photobiol. Sci.* **17**, 874 (2018).
- <sup>231</sup>D. Rimmerman, D. Leshchev, D. J. Hsu, J. Hong, B. Abraham, R. Henning, I. Kosheleva, and L. X. Chen, *J. Phys. Chem. B* **123**, 2016 (2019).
- <sup>232</sup>Y. P. Myer, *Macromolecules* **2**, 624 (1969).
- <sup>233</sup>T. P. Causgrove and R. B. Dyer, *Chem. Phys.* **323**, 2 (2006).
- <sup>234</sup>M. L. Donten and P. Hamm, *Chem. Phys.* **422**, 124 (2013).
- <sup>235</sup>D. Rimmerman, D. Leshchev, D. J. Hsu, J. Hong, B. Abraham, R. Henning, I. Kosheleva, and L. X. Chen, *J. Phys. Chem. B* **122**, 5218 (2018).
- <sup>236</sup>T. Pascher, P. Chesick John, R. Winkler Jay, and B. G. Harry, *Science* **271**, 1558 (1996).
- <sup>237</sup>T. W. Kim, S. J. Lee, J. Jo, J. G. Kim, H. Ki, C. W. Kim, K. H. Cho, J. Choi, J. H. Lee, M. Wulff, Y. M. Rhee, and H. Ihee, *Proc. Natl. Acad. Sci. U. S. A.* **117**, 14996 (2020).
- <sup>238</sup>W. Kühlbrandt, *Nat. Rev. Mol. Cell Biol.* **5**, 282 (2004).
- <sup>239</sup>P. Dzeja and A. Terzic, *Int. J. Mol. Sci.* **10**, 1729 (2009).
- <sup>240</sup>D. C. Rees, E. Johnson, and O. Lewinson, *Nat. Rev. Mol. Cell Biol.* **10**, 218 (2009).
- <sup>241</sup>Z. Zhou, K. A. White, A. Polissi, C. Georgopoulos, and C. R. H. Raetz, *J. Biol. Chem.* **273**, 12466 (1998).
- <sup>242</sup>A. Ward, C. L. Reyes, J. Yu, C. B. Roth, and G. Chang, *Proc. Natl. Acad. Sci. U. S. A.* **104**, 19005 (2007).
- <sup>243</sup>I. Josts, S. Niebling, Y. Gao, M. Levantino, H. Tidow, and D. Monteiro, *IUCrJ* **5**, 667 (2018).
- <sup>244</sup>H. Ravishanker, N. Pedersen Martin, M. Eklund, A. Sitsel, C. Li, A. Duelli, M. Levantino, M. Wulff, A. Barth, C. Olesen, P. Nissen, and M. Andersson, *Sci. Adv.* **6**, eaaz0981 (2020).
- <sup>245</sup>C. Toyoshima, *Biochim. Biophys. Acta Mol. Cell Res.* **1793**, 941 (2009).
- <sup>246</sup>C. Toyoshima, M. Nakasako, H. Nomura, and H. Ogawa, *Nature* **405**, 647 (2000).
- <sup>247</sup>A.-M. L. Winther, H. Liu, Y. Sonntag, C. Olesen, M. le Maire, H. Soehnel, C.-E. Olsen, S. B. Christensen, P. Nissen, and J. V. Møller, *J. Biol. Chem.* **285**, 28883 (2010).
- <sup>248</sup>F. Orädd, H. Ravishanker, J. Goodman, P. Rogne, L. Backman, A. Duelli, M. N. Pedersen, M. Levantino, M. Wulff, M. Wolf-Watz, and M. Andersson, *Sci. Adv.* **7**, eabi5514 (2021).
- <sup>249</sup>C. W. Müller and G. E. Schulz, *J. Mol. Biol.* **224**, 159 (1992).
- <sup>250</sup>C. W. Müller, G. J. Schlauderer, J. Reinstein, and G. E. Schulz, *Structure* **4**, 147 (1996).
- <sup>251</sup>M. Wolf-Watz, V. Thai, K. Henzler-Wildman, G. Hadjipavlou, E. Z. Eisenmesser, and D. Kern, *Nat. Struct. Mol. Biol.* **11**, 945 (2004).
- <sup>252</sup>H. Y. Aviram, M. Pirchi, H. Mazal, Y. Barak, I. Riven, and G. Haran, *Proc. Natl. Acad. Sci. U. S. A.* **115**, 3243 (2018).
- <sup>253</sup>O. Miyashita, J. N. Onuchic, and P. G. Wolynes, *Proc. Natl. Acad. Sci. U. S. A.* **100**, 12570 (2003).
- <sup>254</sup>H. S. Cho, F. Schotte, V. Stadnytskyi, A. DiChiara, R. Henning, and P. Anfinrud, *J. Phys. Chem. B* **122**, 11488 (2018).
- <sup>255</sup>P. Nigro, G. Pompilio, and M. C. Capogrossi, *Cell Death Discovery* **4**, e888 (2013).
- <sup>256</sup>E. Z. Eisenmesser, O. Millet, W. Labeikovsky, D. M. Korzhnev, M. Wolf-Watz, D. A. Bosco, J. J. Skalicky, L. E. Kay, and D. Kern, *Nature* **438**, 117 (2005).
- <sup>257</sup>A. J. Price, F. Marzetta, M. Lammers, L. M. J. Ylinen, T. Schaller, S. J. Wilson, G. J. Towers, and L. C. James, *Nat. Struct. Mol. Biol.* **16**, 1036 (2009).
- <sup>258</sup>J. S. Fraser, M. W. Clarkson, S. C. Degnan, R. Erion, D. Kern, and T. Alber, *Nature* **462**, 669 (2009).
- <sup>259</sup>M. C. Thompson, B. A. Barad, A. M. Wolff, H. S. Cho, F. Schotte, D. M. C. Schwarz, P. Anfinrud, and J. S. Fraser, *Nat. Chem.* **11**, 1058 (2019).
- <sup>260</sup>G. Vanderheeren and I. Hanssens, *J. Biol. Chem.* **269**, 7090 (1994).
- <sup>261</sup>D. A. Dolgikh, L. V. Abaturon, I. A. Bolotina, E. V. Brazhnikov, V. E. Bychkova, R. I. Gilmanshin, Y. O. Lebedev, G. V. Semisotnov, E. I. Tiktopulo, and O. B. Ptitsyn, *Eur. Biophys. J.* **13**, 109 (1985).
- <sup>262</sup>S. Chakraborty, V. Ittah, P. Bai, L. Luo, E. Haas, and Z.-y. Peng, *Biochemistry* **40**, 7228 (2001).
- <sup>263</sup>L. Henry, M. R. Panman, L. Isaksson, E. Claesson, I. Kosheleva, R. Henning, S. Westenhoff, and O. Berntsson, *Struct. Dyn.* **7**, 054702 (2020).
- <sup>264</sup>M. Kataoka, I. Nishii, T. Fujisawa, T. Ueki, F. Tokunaga, and Y. Goto, *J. Mol. Biol.* **249**, 215 (1995).